

Dipartimento di / Department of

Materials Science

Dottorato di Ricerca in / PhD program Materials Science and Nanotechnology

Ciclo / Cycle XXX

Supramolecular porous crystals: anesthetic vapors uptake and enantioselective recognition properties

Cognome / Surname Asnaghi Nome / Name Donata

Matricola / Registration number 730761

Tutore / Tutor: Piero Sozzani

Coordinatore / Coordinator: Marco Bernasconi

ANNO ACCADEMICO / ACADEMIC YEAR 2016/2017

Contents

Introduction		page	5
Chapter 1	<i>The supramolecular dream: controlling matter</i>	page	7
1.1	Chemistry beyond the molecule		8
1.2	Supramolecular concepts		10
1.3	Crystal engineering		10
1.4	Microporous materials: a way for molecular control?		11
1.4.1	Zeolites		12
1.4.2	Mesoporous silica		12
1.4.3	Organosilicas		13
1.4.4	Porous organic materials		13
1.4.5	Metal-organic frameworks		15
1.4.6	Microporous polymers		17
1.5	References		19
Chapter 2	<i>Microporous materials: gas adsorption characterization</i>	page	23
2.1	Physisorption		23
2.2	Chemisorption		25
2.3	Adsorption isotherm		26
2.4	Langmuir isotherm		27
2.5	BET isotherm		29
2.5	The other isotherms		30
2.7	Adsorption hysteresis		31
2.8	Determination of surface area		32

2.9	Ideal Adsorbed Solution Theory (IAST) Selectivity	34
2.10	Thermodynamics of adsorption	34
2.11	References	35

Chapter 3 *Dipeptide-based crystals*

	<i>as volatile-drug vessels</i>	page 36
3.1	Microporous matrices from hydrophobic dipeptides	37
3.1.1	The Val-Ala class	38
3.1.2	Microporous materials for anesthetic drugs delivery	39
3.2	Administration of volatile anesthetics	40
3.2.1	Enflurane	42
3.2.2	Isoflurane	43
3.2.3	Halothane	44
3.2.4	Desflurane	45
3.3	Pharmacokinetics	45
3.4	Mechanism of general anesthesia	46
3.5	Interactions between anesthetics and proteins	47
3.6	Anesthetics adsorption isotherms	48
3.7	NMR spectroscopic detection	52
3.8	Conformational analysis	56
3.9	Conclusions	59
3.10	References	60

Chapter 4 *Metal-organic frameworks:*

	<i>gas adsorption and enantioselectivity properties</i>	page 63
4.1	Homo-chiral metal-organic frameworks: synthetic procedures	64
4.1.1	Synthesis of 1-Zn, 3-Zn, 1-Cu and 3-Cu tectons	65
4.1.2	Synthesis of 1-Cu(OH) and 3-Cu(OH) tectons	66
4.2	Crystal structures	67
4.3	Gas adsorption properties	71
4.4	Enantioselectivity experiments	73
4.4.1	Chiral uptake of (<i>D</i>)- and (<i>L</i>)-tryptophan	73

4.4.2	Enantioselective separation of small molecules	76
4.5	Conclusions	79
4.6	References	79
General conclusions		page 82
Appendix A Experimental conditions		page 85
A.1	Gas and vapor adsorption characterization	85
A.2	X-Ray diffraction	87
A.3	Thermogravimetric analysis	87
A.4	UV-visible absorption spectroscopy	87
A.5	High Performance Liquid Chromatography measurement	88
A.6	Liquid state NMR	88
A.7	Solid state NMR	88
A.8	Dynamic light scattering measurements	89
A.9	Ab initio calculations	89
A.10	Gran Canonical Monte Carlo simulations	89
A.11	Sec-butylamine derivatization conditions	89
Appendix B Physical properties of gases and vapors		page 90
B.1	Pressure units conversion table	90
B.2	Gas and vapor properties	90
B.3	References	91
Appendix C Supporting data		page 92
C.1	SI Chapter 3	92
C.1.1	Dipeptide powder diffraction patterns	92
C.1.2	Isosteric heats of adsorption	93
C.1.3	Adsorption isotherms	94
C.1.4	Conformers of isoflurane and enflurane	97
C.1.5	^1H, ^{19}F and ^{13}C Solid State NMR spectra	98
C.1.6	GCMC simulations	104

C.1.7	Dynamic Light Scattering	105
C.2	SI Chapter 4	105
C.2.1	Crystal structure data of 1-Zn and 3-Zn	105
C.2.2	PXRD patterns	106
C.2.3	Adsorption isotherms for Cu-based MOFs	107
C.2.4	Isosteric heats of adsorption and CO₂/N₂ selectivity	109
C.2.5	HPLC chromatograms	111
C.2.6	UV-vis MBA adsorption monitoring	112
C.2.7	Liquid ¹H NMR spectra	112

Introduction

The design of tridimensional structures at the solid state based on intermolecular interactions, beyond the covalent bond, has caught a growing attention in the supramolecular chemistry field, as illustrated in Chapter 1. Among the extensive family of supramolecular compounds, porous crystalline materials present appealing features: permanent porosity, good thermal and chemical stability, versatile functionalization, long-range order properties and multiple application branches. One of the latter is nanomedicine, which can spread from drug storage and delivery to enantioselective separation of pharmaceutical precursors. These two aspects have been explored during my PhD work, exploiting the manifold physico-chemical characteristics of two classes of supramolecular porous materials: the dipeptide crystals and the homo-chiral metal-organic frameworks.

The first step in the characterization of a porous material passes through the determination of the surface area, the total pore volume and the pore volume distribution by pore size. Chapter 2 is dedicated to the physical adsorption, a technique used to characterize the texture of solids. The relation, at constant temperature, between the amount adsorbed and the equilibrium pressure of the gas is a function named adsorption isotherm. The shape of the adsorption isotherm is the fingerprint of the texture of solids. Two chapters for the description of the experimental parts follow.

Chapter 3 introduces the world of porous dipeptide crystals and their use as volatile anesthetics vessels. When two amino acids are joint together via dehydration synthesis, a dipeptide is formed. Some dipeptides are able to self-assemble in nano-porous structures thanks to charge-assisted hydrogen bonds, after the solvent removal. The porous dipeptides belonging to the Valyl-Alanine family result to be low density materials, with permanent porosity and 1D chiral and hydrophobic channels. Their biological origin makes dipeptide crystals suitable for drug delivery applications. Five porous dipeptide matrixes, Valyl-Alanine (VA), Alanyl-Isoleucine (AI), Valyl-Valine (VV), Isoleucyl-Alanine (IA) and Isoleucyl-Valine (IV), were tested for the adsorption of volatile halogenated ethers used in general anesthesia, namely enflurane, isoflurane, halothane, desflurane and the common diethyl ether. Adsorption and desorption isotherms were performed at 273 and 298 K till the vapor pressure was reached. Then, the guests included in the dipeptide crystals were detected by ^{13}C , ^{19}F and fast- ^1H MAS NMR spectroscopy, in order to understand the molecular arrangement of the anesthetics inside the nano-channels. A conformational analysis on isoflurane and enflurane was conducted to determine the most stable energy minima and to simulate the relative NMR spectra, to be compared with the experimental ones.

In Chapter 4, four new metal-organic frameworks (MOFs), characterized by alkyl moieties with enantiopure stereogenic centers lined inside the channels, are presented. The reaction between Cu(II) cations and organic tectons with methyl or hydroxyl groups bonded to the chiral carbons gave tridimensional, stable and microporous structures, **1**-Cu, **3**-Cu, **1**-Cu(OH) and **3**-Cu(OH), respectively. First, the porosity of the homo-chiral MOFs was confirmed by N₂ and CO₂ adsorption isotherms, obtaining their surface areas and pore size distributions. Their gas sorption properties in mild conditions, until 10 bar and at different temperatures, were tested for N₂, CO₂ and CH₄. The chiral and porous nature of these MOFs was explored for enantioselective adsorption and resolution of racemic mixtures. The first frameworks, **1**-Cu and **3**-Cu, thanks to their stability in water, were exploited for the adsorption in the solutions of two enantiomers of tryptophan, an essential amino acid involved in many biological processes. The other two matrixes, **1**-Cu(OH) and **3**-Cu(OH), were employed for the resolution of small chiral molecules. As guests, simple amines were chosen, since they are frequently used as pharmaceutical precursors. After the soaking in racemic mixtures, the MOFs were carefully washed and on the remaining solutions a derivatization reaction was performed, in order to get aromatic compounds detectable by the UV-vis analyzer of the HPLC system.

Finally, in the appendix parts are reported the experimental conditions used and the supplementary data and information necessary for an easier comprehension of chapter 3 and 4.

Chapter 1

The supramolecular dream: controlling matter

“Chemistry is the science of matter and of its transformations, and life is its highest expression.”

J.-M. Lehn

As sum up by the Nobel laureate Jean-Marie Lehn, chemistry deals with structure and transformation of matter¹. At a first level, chemists work on molecular chemistry, which represent the study of the entities formed by combining atoms to get molecules. A step beyond is represented by supramolecular chemistry, that addresses how molecules interact with each other. Supramolecular chemistry is based on molecular recognition, namely the way that molecules can recognize between one another. In a living organism, such the human body, all the functions are regulated by recognition between molecules, and therefore are at a supramolecular level. One of the most important target for the future research, especially for material scientists, will be the achievement of an accurate control over matter. By “control” we mean the chance to arrange atoms and molecules in a predetermined and well-ordered way, to let them keep their spatial organization. That control is the fundamental tool for dealing with the design of complex systems². From the point of view of precise control on material processes, living systems are the best examples: they are able to create blocks of high complexity. That control on matter is expressed in many situations and it proceeds through a hierarchic organization, from the microscopic to the macroscopic world, and it is extended to dynamic processes. The assumption for the existence of every living cell is the creation of a space division in an external environment and in an internal one: the cell boundary is its cell membrane, an ordered, dynamic structure, made of a double phospholipid self-assembled layer³. The enzymes, which catalyze the biochemical reactions in mild conditions within the cell, owe their operation to their structure: to perform correctly a function, they must show an active site with an exact tridimensional organization⁴. The muscle fibrils⁵ can turn a single molecule contraction in a macroscopic motion, thanks to their spatial disposition scheme. The DNA is the most important case of how the living world is able to precisely handle the matter: to duplicate a DNA molecule without errors is of crucial importance for the conservation of our life⁶. More than half a century has passed since Richard Feynmann gave his well-known speech “*There’s plenty of room at the bottom*”⁷, in which he encouraged his students to care about the intermediate regions between the atomic and the molecular dimensions (tens of Ångströms) and the

micrometer ones. The nanotech process is quickly developing, with large capitals invested⁸ and promising prospects⁹: materials and devices at the nanoscale demonstrate performances different from the bulky ones¹⁰. There are two different approaches to the problem of creating ordered structures in the nanometer region. The first is called *top-down*, the second *bottom-up*. In the *top-down approach* we act on the nanometric objects with tools that bridge the gap between these and the macroscopic world while the *bottom-up* way means how under certain conditions (structural, chemical and physical), matter self assembles. The *bottom-up* approach is the one chosen by Nature to build its architectures. According to the *top-down* approach the researcher is a sculptor of matter, in the bottom-up paradigm the target is to identify the self-assembling mechanisms, operate on the molecular level with the synthesis and organize the molecules to an ordered architecture.

1.1 Chemistry beyond the molecule

Supramolecular chemistry focuses on chemical systems built up by a discrete number of molecular subunits assembled together through reversible and noncovalent interactions. The existence of intermolecular forces was first postulated by Johannes Diderik van der Waals in 1873. However, in 1890, it was Emil Fischer who suggested for the first time that enzyme-substrate interactions take the form of a "lock and key" system, foreseeing the concepts of molecular recognition and host-guest chemistry. In the early twentieth century noncovalent bonds were understood in gradually more detail, with the hydrogen bond being described by Latimer and Rodebush in 1920. The use of these principles led to an increasing understanding of protein structure and other biological processes. For example, the elucidation of the double helical structure of DNA occurred when it was realized that the two strands of nucleotides are connected through hydrogen bonds. The target was to take these concepts and apply them to synthetic systems. The breakthrough came with the work of Charles J. Pedersen¹¹, who succeeded in the synthesis of the crown ethers in the 1960s. Then Donald J. Cram, Jean-Marie Lehn and Fritz Vogtle came and improved the technique for synthesizing selective receptors¹². To recognize the importance of their contributions in the field of supramolecular chemistry, Donald J. Cram, Jean-Marie Lehn, and Charles J. Pedersen were awarded with the Nobel prize in Chemistry in 1987. In the 1990s, supramolecular chemistry greatly developed, thanks to the integration of electrochemical and photochemical motifs, with researchers such as James Fraser Stoddart, Jean-Pierre Sauvage and Bernard Feringa¹³ building molecular machinery and highly complex self-assembled structures. This eventually led to the win of the Nobel prize in Chemistry in 2016 for their work on molecular machines. The new era of nanotechnology also had a strong influence on the topic, with fullerenes, nanoparticles, and dendrimers becoming relevant building blocks in synthetic systems.

Supramolecular chemistry deals with subtle interactions, and consequently control over the processes involved can require great precision. To do so, we have to limit the degrees of freedom of atoms and molecules, forcing them to take a definite spatial position, constant in time. Therefore, we have to put constraints: a molecule, for example, is a set of atoms, which, however, is more than the sum of the atoms that make it; a molecule is an ordered set of those atoms and that order is guaranteed and maintained by some constraints, that, in the case of molecules, are the covalent bonds. Therefore, the degrees of freedom of the individual atoms are reduced and

that reduction is the key for the inherent order in a molecule. The constraints are defined in terms of interactions: two objects are bound and they are no more independent from each other if there is an interaction that joins them. The covalent bond is an interaction between two or more atoms, based on the bonding electrons that occupy the binding molecular orbitals, situated at lower energies compared to the initial molecular orbitals. It's a strongly directional interaction and it involves energies of hundreds of kJ/mol. Besides the covalent bond there are other kinds of interactions, different from each other because of their various spatial and angular dependence and, above all, for their energy. These interactions, in order of decreasing intensity, are¹⁴:

- **interactions ion-ion and ion-dipole: 50-200 kJ/mol**
- **hydrogen bonding: 4-120 kJ/mol**
- **interaction cation- π : 5-80 kJ/mol**
- **interaction dipole-dipole: 5-50 kJ/mol**
- **London or dispersion forces: < 5 kJ/mol**

The interactions ion-ion and dipole-dipole have a non-directional character because they depend only on the distance between electrostatic charges and the dipoles involved; the interaction is long-range. The hydrogen bonding involves three atoms: a hydrogen one, covalently bounded to an electronegative acceptor atom, and another electronegative donor atom (donor and acceptor are in general fluorine, oxygen, sulfur or nitrogen). This kind of bonding has an angular dependence and it is short-range. The interactions cation- π are between a metallic cation and the electrons in the π orbitals of organic molecules, they are directional and short-range. The interactions dipole-dipole and the London forces are not directional and they are known as "Van der Waals forces". All these interactions are even known as "supramolecular" interactions: by definition they are interactions between separate molecules, interactions that go *beyond* the molecule¹. From a thermodynamic point of view, noncovalent bonds have low energies and often no activation energy for formation. As demonstrated by the Arrhenius equation¹⁵, this means that the rate of bond formation is not increased at higher temperatures. In fact, chemical equilibrium equations show that the low bond energy results in a shift towards the breaking of supramolecular complexes at higher temperatures. However, low temperatures can also be problematic to supramolecular processes. Supramolecular chemistry can require molecules to distort into thermodynamically disfavored conformations and cooling the system would slow these processes. Thus, thermodynamics is an important tool to design, control, and study supramolecular assemblies. The molecular environment around a supramolecular system is also of prime importance to its operation and stability. Many solvents have strong hydrogen bonding, electrostatic, and charge-transfer capabilities, and are therefore able to become involved in complex equilibria with the system, even breaking complexes completely. For this reason, the choice of solvent can be critical.

1.2 Supramolecular concepts

Nowadays, supramolecular chemistry is split in different interdisciplinary branches (chemical, physical, biological and technological) and the range of its research objects is very wide. To understand how molecules are assembled by non-covalent interactions, we first introduce the principle of *close packing*, established by A. I. Kitaigorodsky¹⁶. According to this principle, the molecules tend to fill available space in the most efficient way with the greatest number of energetically favorable intermolecular van der Waals contacts. Driven by this principle, self-assembly may be divided into *intermolecular* self-assembly (to form a supramolecular assembly), and *intramolecular* self-assembly (as demonstrated by foldamers and polypeptides). Moreover, *molecular* self-assembly also allows the construction of larger structures such as micelles, membranes, vesicles, liquid crystals, and is important to crystal engineering¹⁷.

Molecular recognition is the specific binding of a guest molecule to a complementary host molecule to form a host-guest complex. One of the most important category of host-guest systems are the *inclusion compounds*. Inclusion compounds or *clathrates* are formed as a result of inclusion of molecules of one kind into cavities formed by the molecules of another kind. These inclusion compounds reach close packing due to filling of the cavities of a porous network formed by the host molecules with the presence of guest molecules. Supramolecular chemistry's principles can be applied not only for the synthesis of self-assembled aggregates, but also to catalyze chemical reactions. Noncovalent bonds between the reactants and a "template" keep the reactive sites of the reactants close together. This pre-organization is particularly helpful for situations where the desired reaction conformation is thermodynamically or kinetically unlikely, such as in the preparation of large macrocycles. After the reaction, the template can be easily removed or de-complexed. Supramolecular templated-directed synthesis can efficiently produce complex compounds, like *catenanes*, *rotaxanes*, molecular *knots*, and molecular *Borrromean rings*, which represent examples of mechanically-interlocked molecular architectures. These systems consist of molecules that are linked only as a consequence of their topology¹⁸. The latest and most complex products in the supramolecular field are the well-known *molecular machines*, molecular assemblies that can perform functions such as linear or rotational movement, switching, and entrapment. With the development of experimental methods and growing experience in "molecular engineering," these mechanisms can carry out mechanical, electric, photochemical and other work in a similar way as their macroscopic analogs (motors, switches, muscles, etc)^{1,19}.

1.3 Crystal engineering

The main idea of *crystal engineering* exploits the principles of supramolecular chemistry for the design of periodic structures with a desired organization. Knowing the nature and the structure of the building blocks (molecules, ions, coordination centers, ligands), it is possible to predict the features of the resultant crystalline material. The term crystal engineering was validated for the first time by G. M. J. Schmidt, in a contribution to organic solid-state photochemistry²⁰. The link between crystal engineering and supramolecular chemistry was highlighted considering that crystals can be thought as the sum of a series of molecular recognition events.

According to this principle, crystalline materials can be considered as supramolecular entities or supermolecules. Organic crystals present physical and chemical characteristics due to both the properties of the molecular building units and to their distribution inside the network. Thanks to these versatile features, crystal engineering can develop in different areas, such as material science, pharmaceutical research and synthetic chemistry. However, crystal engineering has failed till now in finding a universal solution to the problem of forecasting the required properties of the resultant crystal, known the starting building blocks' ones. This problem was already underlined by Maddox²¹: "*One of the continuing scandals in the physical sciences is that it remains in general impossible to predict the structure of even the simplest crystalline solids from a knowledge of their chemical composition*". If this question is still unsolved, a number of good strategies have been developed to guide the work of crystal engineering. One, already cited above, is Kitaigorodsky's principle of close packing for molecular crystals. Other interesting ideas come from M. C. Etter's rules, for crystals based upon hydrogen bonds²², from concepts like the supramolecular synthon, a specific way of assembly through functional groups of adjacent molecules²³, and the tecton, a molecule forming strong directed interactions in crystals^{24,25}. On tectons is based molecular tectonics, a strategy which deals with complementary building units bearing recognition information and thus capable of finding a way to self-assemble in the most stable network, under given conditions²⁶. The introduction of additional components in the crystal can offer new opportunities. As reported in the previous paragraph, a second (*guest*) component is frequently used as a template to arrange molecules of the first (*host*) component in a desired way. This method is extensively applied in the manufacturing of synthetic zeolites^{27,28} and other porous sorbents²⁹⁻³¹ [86-88]. Multicomponent systems can open a new way to arrange atoms and molecules at a higher level, in order to widen the horizons of crystal engineering.

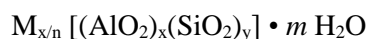
1.4 Microporous materials: a way for molecular control?

As said above, giving order to matter corresponds to limiting the degrees of freedom of matter itself. One possibility, although indirect, to achieve this goal consists in confining the molecules, by including them into architectures in which they are forced to assume a certain spatial arrangement, determined by the steric control of the cavity. The porous materials are solids, crystalline or amorphous, characterized by a discontinuous matter distribution: these materials show cavities that can act as a "mold" for other molecules, which, entering in the pores, can occupy the spatial "negative" of the porous material. The *bottom-up* approach, in this case, has a double function: on one hand, it leads to the application of its principles towards the synthesis and the preparation of microporous self-assembled structures, on the other hand, the microporous materials can open a series of possibilities for the scientist, who now has a tool of selection, manipulation and organization at the nanoscale. The microporous materials indeed can find an application in those areas in which is crucial to take control on the positioning of the molecular species: for example in catalysis, in gas purification and storage, in liquid purification, and in chemical sensors³²⁻³⁴. The cavities can also be functionalized to create sites of specific interaction between the matrix and the guest molecules: those specific interaction, thanks to the high

superficial area of the microporous materials, are maximized. We are now going to illustrate the most common microporous systems.

1.4.1 Zeolites

The zeolites are aluminosilicate minerals, with general formula:



From a structural point of view, they are characterized by tridimensional tetrahedral structures TO_4 ($T = Al, Si$), that delimit channels and or cavities interconnected, in which there are the ions, for the electroneutrality of the system, and the water molecules, that give the porosity when removed. The porosity depends on the number of polyhedral around the pore³⁵. Though they are the first synthetic porous system, zeolites still represent the most interesting porous material from a commercial point of view, with an annual production of about 5.5 million tones³⁶. For example, they're extensively used in detergents to soften the water, through ionic exchange between Ca^{2+} and Na^+ . Zeolites are mainly synthesized by hydrothermal³⁷: the reaction occurs in autoclave at high temperatures and pressures with surfactants as templates to obtain the desired porous structures.

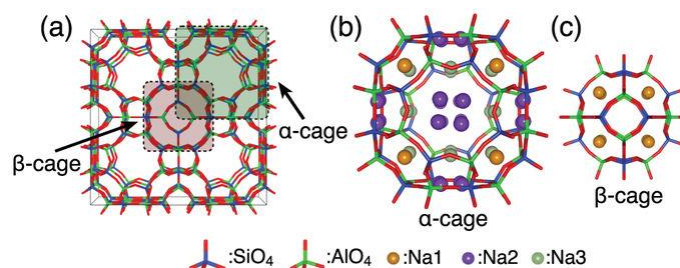


Figure 1. (a) [100]-projection of NaA zeolite structure; (b) schematic model of α -cage; (c) schematic model of β -cage³⁵.

1.4.2 Mesoporous silicas

Mesoporous silicas are systems of high relevance, because they were the first material to show structure with ordered channels; currently, there is a multiplicity of those systems, divided in two principal categories: the SBA and the MCM. The mesoporous silicas are characterized by large superficial area, good hardness, both chemical and mechanical, and they're akin to particular classes of molecules³⁸. These systems are mainly produced via template synthesis in aqueous environment from appropriate silica precursors; the choice of templates of different dimensions or micellar aggregation forms allows to modulate the pores geometry. The main applications of mesoporous systems are catalysis, gas storage and as loaders in polymer mixtures³⁹.

1.4.3 Organosilicas

The inclusion of organic components inside mesoporous silica systems allows obtaining materials with excellent structural properties, derived from the mesoporous silicas, and the chemical reactivity, associated with the organic functionalities⁴⁰. The organic component is intimately bounded to the inorganic one, and that bond can be obtained in different modes: we can do a grafting of the organic component directly on the silica matrix or we can bound the organic part to the silica one during the precursor synthesis that will be used later in the porous system synthesis⁴¹. One of the most common precursors of the organosilicas is bis-triethoxysililbenzene, that can condensate to obtain an hybrid system, with silica walls and benzene rings ordered in a crystal-like structure. The simple benzene ring can be replaced with more complex organic systems to get different organosilicas. The applications of those systems are similar to the silicas ones, with the extra possibility to exploit the organic functionalities to ensure greater chemical reactivity and selectivity⁴².

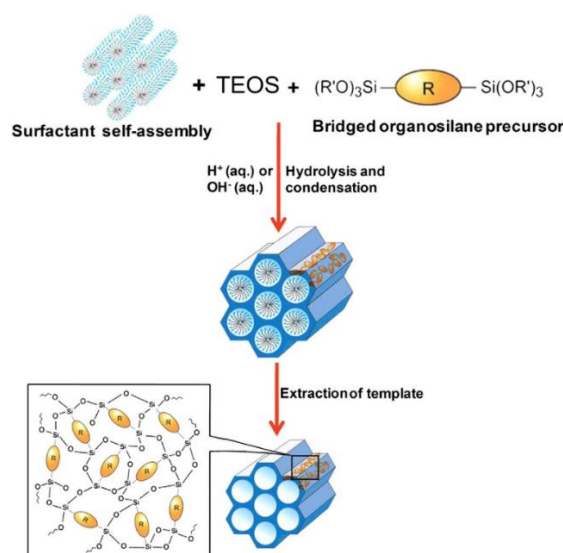


Figure 2. General synthetic pathway for periodic mesoporous silica (PMO). R = bridging organic linker⁴⁰.

1.4.4 Porous organic materials

The formation of porous organic materials is a consequence of the peculiar organization assumed by some organic molecules to obtain an energetic convenient structure (molecular crystals). The founder of this family is the urea. Urea belongs to the clathrate family, molecules that normally crystallize in non-porous systems, but in the presence of particular solvents can crystallize in a porous form, that can accommodate solvent molecules. When urea meets linear alkanes with chains of at least six atoms crystallizes, giving rise to channels with hexagonal geometry that hold the alkanes molecules; the driving force of this process is the creation of hydrogen bonds, that are preferentially formed with a precise geometry, stable unless the solvent molecules are removed⁴³. Thanks to its properties, urea has been widely used for linear alkanes separation from hydrocarbons mixtures. Another important organic crystal is tri(ophenilendioxy) cyclophosphazane (TPP), the first organic substance with a porous crystalline packing stable even when the clathrate is removed.

Synthesized by Allcock et al in 1963, it is formed by a triphosphazenic ring (P_3N_3), and every phosphorous atom is bounded to a cathecol in order to make the molecule similar to a helix⁴⁴. The TPP has two polymorphs: a monoclinic contact one and a hexagonal porous one, more stable thanks to the crystallization from benzene. The mono-dimensional channels of TPP are constituted by cathecol molecules and they result in a total apolar environment, tested for CO_2 , CH_4 and Xe adsorption⁴⁵. The natural world often provides excellent examples of functionalized materials; for example, the initial experiences with natural zeolites has led to very successful efforts to produce a wide variety of industrially relevant synthetic matrixes⁴⁶. Recently, supramolecular architectures based upon weaker interactions have motivated a number of studies⁴⁷: polypeptides that can build tubular and helical structures have attracted considerable attention because of their biological relevancy. A really important class of molecular assemblies which comes from the biologic world are the dipeptide crystals, which show a permanent porosity, with nanochannels characterized by targeted interactions, biocompatibility and biodegradation. These self-assembling structures, with chiral and biological nanochannels, have raised an increasing interest. Dipeptide crystals have demonstrated applicability as transmembrane pores and ion channels, as well as size-selective ion sensors⁴⁸. The nanochannels are formed by the aggregation of dipeptides in a head-to-tail hydrogen-bonded network, forming tubes with hydrophobic or hydrophilic interiors, depending on the lateral substituents on the different amino acids. An important example of microporous, hydrophobic, chiral class of dipeptide crystals is the Valyl-Alanine family⁴⁹: the molecules of Valyl-Alanine are ordered as a spiral around the structural hexagonal axis, with space group $P6_1$. The analysis of dipeptides sorption properties is fully described in chapter 3.

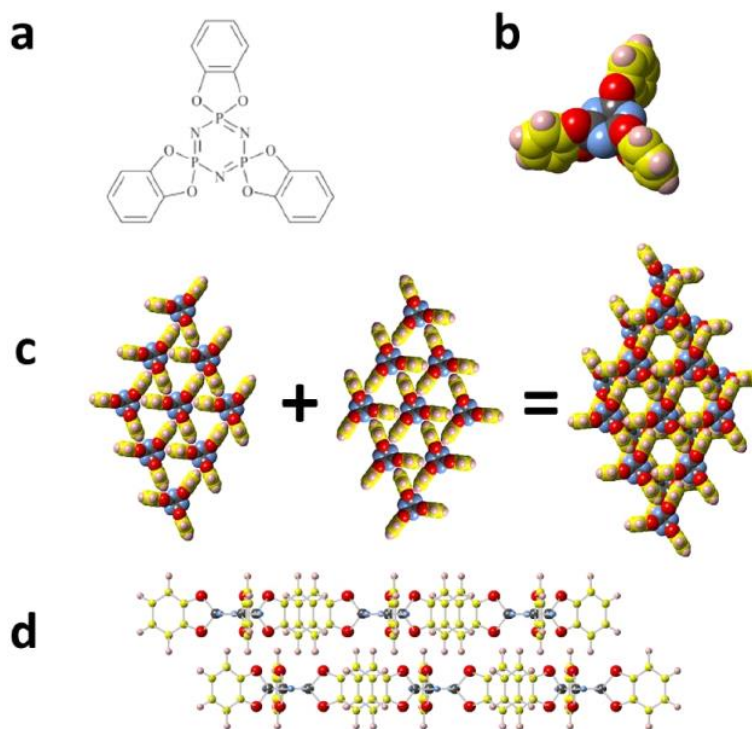


Figure 3. Crystal structure of hexagonal TPP. (a) Chemical structure and (b) space-filling model of a TPP molecule; two successive layers of a crystal viewed from the (c) top and (d) side⁴⁴.

1.4.5 Metal organic frameworks (MOFs)⁵⁰

MOFs are a prominent class of porous materials and, thanks to their considerable versatility and to their exceptional performances, they have been the center of a vivid research. The MOFs, also known as coordination polymers, are hybrid compounds based on coordinative bonds between metallic cations and organic molecules; the metallic ions are assembly nodes, while the organic molecules are used as *spacers* between the cation nodes, forming together a supramolecular architecture. They show a high crystalline order and good chemical and mechanical stability. The choice of the ion enables to modify both geometry and the number of spacers (from planar to octahedral geometry); different organic molecules can modulate the distance between the ions and the number of ions to be bound to. Currently, the Cambridge Structural Database counts over 13.000 different MOF structures. The organic molecules, to be good spacers, must comply with some common requirements: they have to be enough rigid to ensure stiffness at the crystal system and they must have functionalities able to form coordinative bonds. The best candidates are the conjugate molecules, with linear or polyhedral geometry, which possess electron-rich functionalities (amino and carboxyl groups). The spacer dimensions mustn't be too high, because, otherwise, this can provoke interpenetration phenomena and, consequently, the structure collapse. The first MOFs had simple metallic ions as assembly nodes, whereas, with the progress of synthetic procedures, they have been replaced by complex, which have the same ability to form coordinative bonds, but own a higher versatility for the assembly geometries. The various geometries that can be produced are then called SBU, *secondary building unit*. There are a lot of synthesis procedures for MOFs, for example solvothermal, electrochemical, solvent free chemo-mechanical synthesis. All these techniques must preserve the building block structure and provide the possible deprotonation of the functional groups to obtain the coordinative bonds. The most common applications for MOFs are gas storage and purification, catalysis, non-linear optics materials, and electric, optical, magnetic sensors⁵¹. Many efforts have been made to develop 3D structures with targeted features: the ability to incorporate chiral functionalities into porous entities offers the chance to expand their utility in catalytic and enantioselective processes⁵². Nevertheless, the synthesis and the characterization of robust porous homo-chiral metal-organic frameworks have not reached satisfying achievement yet⁵³. Most homo-chiral metal-organic frameworks are not robust enough to retain permanent porosity, nor porous enough to be exploited for enantiomer resolution or catalytic transformation of small molecules. However, many attempts have been made, since the potential application fields are appealing from an industrial point of view⁵⁴. For the synthesis of homo-chiral open tridimensional networks, two main methods have been followed: 1) the use of a rigid homo-chiral organic ligand as a linker⁵⁵; 2) the use of a chiral "template", which compels the structure to adopt a specific chiral topology^{52d}. Prof. Kim et al.⁵⁶ proposed a different approach, through which a metal ion and a simple homo-chiral organic linker are used to form homo-chiral secondary building units; as a second step, these are linked together by rigid polytopic connectors to build a porous network structure, in a one-pot reaction. A post-synthetic route provides the formation of homo-chiral MOFs from a chiral or achiral parent MOF by synthetic modification of the organic structures or the metal nodes and by guest exchange⁵⁷. The post synthesis choice allows for the fabrication of homo-chiral porous MOFs from either homo-chiral porous MOFs or achiral porous MOFs. The

synthetic pathway chosen in this PhD work belongs to the first route and implies the use of enantiomerically pure organic tectons, bearing the chiral functionalities on alkyl or alkoxy side chains, as illustrated in chapter 4. The efficiency in catalytic and enantioresolution fields strictly depends on the communication between the host framework and the guest molecules. In particular, the enantioselective separation of small guests by homo-chiral MOFs deals with two principal methods: the adsorption separation and the selective crystallization of diastereomeric of inclusion compounds.

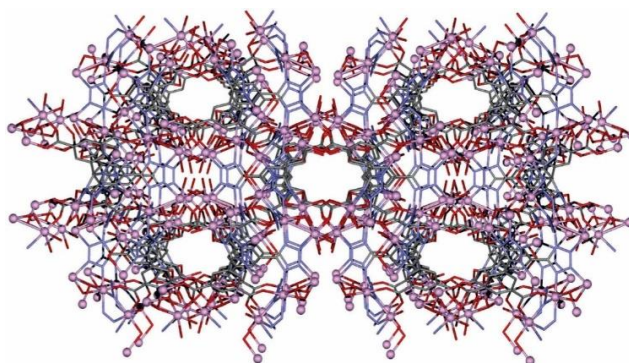


Figure 4. The view down the *c* axis of the channels in the three-dimensional network of a MOF based on 5-(1H-tetrazol-5-yl)isophthalic acid ligand. Color code N = blue, O = red, C = grey and cobalt = dark blue⁵¹.

The first approach has been deeply explored with the homo-chiral meta-organic frameworks involved in this PhD thesis, but many examples have come before our experiments. In 2001, Xiong and coworkers created the prototype of enantioselective sorption and separation with a homo-chiral 3D zeolite-like MOF⁵⁸. The compound [Cd(QA)₂] was obtained by treating enantiopure chiral bridging ligand quitenine (6'-methoxyl-(8*S*,9*R*)-cinchonane-9-ol-3-carboxylic acid (HQA)) with Cd(OH)₂. Under solvothermal conditions, treating the framework and racemic 2-butanol afforded colorless crystalline sample MOF · (*S*)-2-butanol, with an enantiomeric excess of 98.2%. In 2004, Rosseinsky and coworkers reported several homo-chiral MOFs displaying enantioselective sorption that is strongly dependent on guest size⁵⁹. The helix chirality of the Ni²⁺, six-coordinated with the trans diaxial positions occupied by two tridentate ligands, MOF is controlled by the 1,2-propanediol co-ligand. The chiral guest species chosen were ethyl-3-hydroxybutyrate, the terpenes menthone, fenchone and the aromatic diol binaphthol. The racemic samples were taken up by the evacuated matrixes from the liquid or vapor phase, and later removed from the resolved frameworks by washing with dichloromethane. While chiral-GC reveals no enantioselection for the former three desorbed chiral guests, binaphthol was sorbed with an enantiomeric excess of 8.3% (as determined by HPLC analysis). Clearly, a close match to the channel dimensions is required to bring the chiral guests sufficiently close to the helical internal surface of porous material to allow for discrimination between the enantiomers. In 2008, Cui et al. presented a wide array of cyclic clusters with enzyme-like chiral cavities for applications in separating chemical species^{60,61}. Heating a mixture of the semiflexible pyridyl-functionalized salen-based ligand with Zn(NO₃)₂ · 6H₂O in mixed solvent solutions of DMF-CH₃CN and DMF-THF led to crystalline products, then

coordinated to form a tetrameric or hexameric cyclic clusters with a chiral cavity at the core (as shown in figure 5). This resolution of 2-butanol was achieved by soaking the evacuated samples in neat racemic alcohols in a sealed vial at 40 ° C for 2-3 days. Chiral GC analysis of the desorbed 2-butanol from (*R*)-MOF by distillation showed the enantiomeric excess value was 99.8% and the absolute *R* configuration was obtained by comparing its optical rotation with that of the standard sample. Similar enantioselective inclusion was observed for racemic 3-methyl-2-butanol, whereby the same MOF exhibited remarkable sorption toward the *R* enantiomer over the *S* enantiomer as well. The enantiomeric excess value of the desorbed 3-methyl-2-butanol was determined to be 99.6% by chiral GC analysis. In 2006, Fedin and Kim et al. investigated the separation and catalytic properties of a homo-chiral porous MOF for enantioselective adsorption and oxidation of thioethers⁵⁶. In this case, the chiral centers of the L-lactate moieties were exposed within the channels. The obtained material showed an excellent sorption capability to the sulfoxides with smaller substituents. The enantiomeric excess values for the adsorbed guests were 20% ~ 27%, with the *S* enantiomer in excess for all the cases. However, sulfoxides with larger substituents could not be included in any significant amount. Such size- and enantioselective guest inclusion indicates that this structure had a robust structure with pores of uniform size and chiral environment. In conclusion, homo-chiral MOFs represent an emerging class of materials and, particularly those structures composed by enantiopure organic ligands, could be expected to offer new opportunities for chiral adsorption and resolution of pharmaceutical precursors in the near future. Some examples of these application fields are shown in chapter 4.

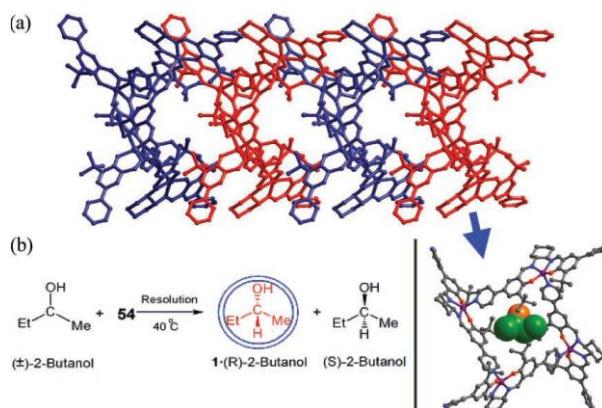


Figure 5. (a) Sideview of the packing of metallacycle 54 with 2-butanol molecules lying inside; (b) Schematic representation of the chiral separation of *rac*-2-butanol⁶⁰.

1.4.6 Microporous polymers

As in other scientific fields, also in the porous world the polymer systems have begun to become important thanks to their synthetic easiness and versatility and to the competitive performances that characterized them. To the microporous polymers belong a wide range of systems: COF (Covalent Organic Frameworks), HCP (Hyper-Crosslinked Polymers), CMP (Conjugated Microporous Polymers), PIM (Polymers of Intrinsic

Microporosity)⁶². COFs are crystalline systems, first synthesized by Yaghi⁶³, constituted by organic monomers connected by strong covalent bonds. A lot of these systems are characterized by the presence of boron-oxygen bonds, that give rise to five- or six-atom rings, with the same function of the metallic centers in MOFs. As for the MOFs, the use of different molecules can provide a high number of geometries and pore sizes. These porous systems present crystalline order, chemical stability and superficial areas that can rise up to 3500 m²/g⁶⁴. The other classes of microporous polymers aforementioned are have general characteristics in common, such as they don't assume an ordered structure and they usually are amorphous. The amorphous phase does not preclude the microporosity, as demonstrated by the structure of activated carbon⁶⁵. Amorphous polymeric hyper-cross-linked (HCP) networks have been synthesized tens of years ago; the solvent removal, in this case, involves the creation of a permanent porosity, with a large pore size distribution (from micro to macropores). The first derive from the template effect of the solvent, whereas the bigger ones are formed from the phase separation of the polymer and the solvent. They are an example of extrinsic porosity. The polymers of intrinsic microporosity (PIM) are systems with a twisted molecular structure, the polymer backbone doesn't have rotational degrees of freedom, and this prevent the macromolecule components to efficiently pack in compact structures, producing high superficial areas, microporosity and an amorphous structure. The typical porosity of PIMs is a direct consequence of the stiffness and the form of the single macromolecular components, but, unlike the HCPs, they don't have an extrinsic contribution to the porosity and then they have a narrower and homogenous pore size distribution. Recently, a large number of works about the synthesis and the characterization of these materials have been published^{66,67}. Cooper and his co-workers have reported the synthesis of a polyarilenethilene obtained by Pd-catalyzed Sonogashira-Hagihara coupling⁶⁸. This polymer is microporous, it exhibits a superficial area (BET) of 834 m²/g and it doesn't have any long-range order. Relating to PIMs, it is possible to control the pore size distribution and the superficial area varying the length and the rigidity of the organic linkers³⁹. These systems are more thermally and chemically stable than MOFs, as they're composed only by C-C and C-H bonds. The degradation temperatures are above 400° C and they are chemically stable to both acid and basic treatments. A particular class of microporous polymers, recently discovered, is the PAF (Porous Aromatic Framework) family. These systems have superficial areas between the more elevated ever reported in literature⁶⁹, and therefore they are really important for gas adsorption and storage.

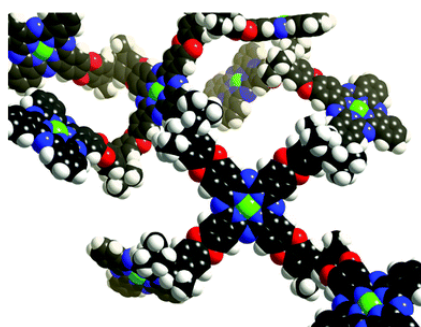


Figure 6. A molecular model of the phthalocyanine-based PIM⁶⁶.

1.5 References

- 1 J.-M. Lehn, *Supramolecular Chemistry: concepts and perspectives*, **1995**.
- 2 J.-M. Lehn, *PNAS*, **2002**, vol. 99 no. 8, 4763.
- 3 K. Y. C. Lee et al., *J. Am. Chem. Soc.*, 2001, 123, 6951.
- 4 D. E. Jr. Koshland, *Proc. Natl. Acad. Sci.*, **1958**, 44, (2), 98.
- 5 H. Epstein, Fischman D., *Science*, **1991**, 251, 1039.
- 6 T. A. Kunkel, *The Journal of Biological Chemistry*, **2004**, vol. 279, no. 17, 16895.
- 7 R. P. Feynmann, "There's plenty of room at the bottom", **1959**
- 8 <http://www.cordis.europa.eu/nanotechnology>
- 9 E. Drexler, "Engines of Creation. The coming era of nanotechnology.", **1986**
- 10 E. Roduner, *Chem. Soc. Rev.*, **2006**, 35, 583.
- 11 (a) J. Pedersen, *J. Am. Chem. Soc.*, **1967**, 89, 2495; (b) C. J. Pedersen, *J. Am. Chem. Soc.*, **1967**, 89, 7017; (c) C. J. Pedersen, *Angew. Chem., Int. Ed. Engl.*, **1988**, 27, 1021.
- 12 (a) D. J. Cram, J. M. Cram, *Acc. Chem. Res.*, **1978**, 11, 8; (b) J. M. Lehn, *Pure Appl. Chem.* **1978**, 50, 871; (c) J. M. Lehn, *Acc. Chem. Res.*, **1978**, 11, 49; (d) F. Vögtle and E. Weber, *Angew. Chem. Int. Ed. Engl.*, **1974**, 13, 814.
- 13 (a) V. Balzani, M. Gómez-López and J. F. Stoddart, *Acc. Chem. Res.*, **1998**, 31, 7, 405; (b) J.-P. Collin, C. Dietrich-Buchecker, P. Gaviña, M. C. Jimenez-Molero and J.-P. Sauvage, *Acc. Chem. Res.*, **2001**, 34, 6, 477; (c) R. Eelkema, M. M. Pollard, J. Vicario, N. Katsonis, B. Serrano Ramon, C. W. M. Bastiaansen, D. J. Broer and B. L. Feringa, *Nature*, **2006**, 440, 163.
- 14 J. W. Steed, J. L. Atwood, *Supramolecular Chemistry*, **2000**.
- 15 K. J. Laidler, *The World of Physical Chemistry*, **1993**.
- 16 A. I. Kitaigorodsky, *Molecular Crystals*, **1971**.
- 17 K. Ariga, J. P. Hill, M. V. Lee, A. Vinu, R. Charvet, S. Acharya, *Sci. Techno. Adv. Mater.*, **2008**, 9, 014109.
- 18 T. Ikeda, J. F. Stoddart, *Sci. Techno. Adv. Mater.*, **2008**, 9, 014104.
- 19 (a) Z. Asfari and J. Vicens, *J. Inclus. Phenom.*, **2000**, 36, 103; (b) J. F. Stoddart, *Acc. Chem. Res.*, **2001**, 34, 6.
- 20 G. M. Schmidt, *J. Pure Appl. Chem.*, **1971**, 27, 647.
- 21 J. Maddox, *Nature* **1988**, 335, 201.
- 22 M. C. Etter, *Acc. Chem. Res.*, **1990**, 23, 120.
- 23 G. R. Desiraju, *Angew. Chem. Int. Ed.*, **1995**, 34, 2311.

- 24** D. Su, X. Wang, M. Simard, and J. D. Wuest, *Supramol. Chem.*, **1995**, 6, 171.
- 25** M. W. Hosseini, *Coord. Chem. Rev.*, **2003**, 240, 157.
- 26** M. W. Hosseini, *Acc. Chem. Res.*, **2005**, 38, 313.
- 27** R. Szostak, *Molecular Sieves: Principles of Synthesis and Identification*, **1998**.
- 28** R. J. Francis and D. O'Hare, *J. Chem. Soc., Dalton Trans.*, **1998**, 3133.
- 29** A. K. Cheetham, G. Férey, and T. Loiseau, *Angew. Chem. Int. Ed.*, **1999**, 38, 3268.
- 30** G. J. A. A. Soler-Illia, C. Sanchez, B. Lebeau, and J. Patarin, *Chem. Rev.*, **2002**, 102, 4093.
- 31** S. Kitagawa, R. Kitaura, and S. Noro, *Angew. Chem. Int. Ed.*, **2004**, 43, 2334.
- 32** F. Fajula et al, *Microporous and Mesoporous materials*, **2005**, 82, 227.
- 33** M. E. Davis, *Nature*, **2002**, vol. 417, 813.
- 34** F. Shüth, W. Schmidt, *Adv. Mater.*, **2002**, 14, 629.
- 35** (a) G. Férey, *C. R. Acad. Sci. Paris*, **1998**, 1-13; (b) K. Yoshida, K. Toyoura, K. Matsunaga, A. Nakahira, H. Kurata, Y. H. Ikuhara, Y. Sasaki, *Scientific Reports*, **2013**, 3, 2457.
- 36** C. Rhodes, *Zeolites and World Markets*, **2003**.
- 37** R. Aiello, C. Collela, Soc. It. Min., rendiconto, **1975**.
- 38** U. Ciesla, F. Schult, *Microporous and Mesoporous materials*, **1999**, 27, 131.
- 39** K. W. Gallis, J. T. Araujo, K. J. Duff, J. G. Moore, C. C. Landry, *Adv. Mater.*, **1999**, 11, 17, 1452.
- 40** (a) A. Walcarius, L. Merier, *J. Mater. Chem.*, **2010**, 20, 4478; (b) N. Pal and A. Bhaumik, *Advances in Colloid and Interface Science*, **2013**, 189–190, 21.
- 41** F. Hoffmann, M. Cornelius, J. Morell, M. Foreba, *Angew. Chem. Int. Ed.*, **2006**, 45, 3216.
- 42** M. Beretta, J. Morell, P. Sozzani, M. Froba, *Chem. Commun.*, **2010**, 46, 2495.
- 43** L. J. Atwood, J. D. Davies, D. D. Macnicol, F. Vögtle, *Comprehensive Supramolecular Chemistry*, **1996**, Vol. 6, Chap. 7.
- 44** (a) H. R. Allcock, L. A. Siegel, *J. Am. Chem. Soc.*, **1967**, 86, 5140; (b) L. Kobr, K. Zhao, Y. Shen, R. K. Shoemaker, C. T. Rogers and J. Michl, *Cryst. Growth Des.*, **2014**, 14, 559.
- 45** P. Sozzani, S. Bracco, A. Comotti, L. Ferretti, R. Simonutti, *Angew. Chem. Int. Ed.*, **2005**, 44, 1816.
- 46** a) R. M. Barrer in *Inclusion Compounds*, Vol. 1 (Eds.: J. L. Atwood, J. E. D. Davies, D. D. MacNicol), Academic Press, London, **1984**, pp. 191 – 248; b) Nanoporous Materials III, *Studies in Surface Science and Catalysis*, Vol. 141 (Eds.: A. Sayari, M. Jaroniec), Elsevier, Amsterdam, **2002**.

- 47** (a) D. V. Soldatov, *J. Inclusion Phenom. Mol. Recognit. Chem.*, **2004**, 48, 3; (b) D. V. Soldatov in *Encyclopedia of Supramolecular Chemistry*, Marcel Dekker, New York, **2004**, 1302.
- 48** (a) M. R. Ghadiri, J. R. Granja, R. A. Milligan, D. E. McRee, N. Khazanovich, *Nature*, **1993**, 366, 324; (b) S. McKim, J. F. Hinton, *Biochim. Biophys. Acta*, **1994**, 1193, 186; (c) D. Seebach, P. E. Ciceri, M. Overhand, B. Jaun, D. Rigo, L. Oberer, U. Hommel, R. Amstutz, H. Widmer, *Helv. Chim. Acta*, **1996**, 79, 2043; (d) J. D. Hartgerink, T. D. Clark, M. R. Ghadiri, *Chem. Eur. J.*, **1998**, 4, 1367; (e) M. Rechez, E. Gazit, *Science*, **2003**, 300, 625; (f) T.-L. Lau, K. J. Barnham, C. C. Curtain, C. L. Masters, F. Separovic, *Aust. J. Chem.*, **2003**, 56, 349.
- 49** (a) D. V. Soldatov, I. Moudrakovski, J. A. Ripmeester, *Angew. Chem. Int. Ed.*, **2004**, 43, 6308; (b) D. V. Soldatov, I. Moudrakovski, E. V. Grachev and J. A. Ripmeester, *J. Am. Chem. Soc.*, **2006**, 128, 6737; (c) C. H. Gorbitz and E. Gundersen, *Acta Cryst.*, **1996**, C52, 1764.
- 50** (a) J. L. C. Rowsell, O. M. Yaghi, *Microporous and Mesoporous materials*, **2004**, 73, 3; (b) H. K. Zhou, J. R. Long and O. M. Yaghi, *Chem. Rev.*, **2012**, 112 (2), 673; (c) H. Furukawa, K. E. Cordova, M. O'Keeffe and O. M. Yaghi, *Science*, **2013**, Vol. 341, 6149, 1230444; (d) H. C. Zhou and S. Kitagawa, *Chem. Soc. Rev.*, **2014**, 43, 5415.
- 51** (a) M. Dinca, J. R. Long, *Angew. Chem. Int. Ed.*, **2008**, 47, 6766; (b) A. J. Calahorra, A. Salinas-Castillo, J. M. Seco, J. Zuniga, E. Colacio and A. Rodriguez-Dieguez, *CrystEngComm*, **2013**, 15, 7636.
- 52** (a) K. S. Min, M. P. Suh, *Chem. Eur. J.* **2001**, 7, 303; (b) K. Uemura, S. Kitagawa, M. Kondo, K. Fukui, R. Kitaura, H.-C. Chang, T. Mizutani, *Chem. Eur. J.* **2002**, 8, 3587; (c) D. N. Dybtsev, H. Chun, S. H. Yoon, D. Kim, K. Kim, *J. Am. Chem. Soc.* **2004**, 126, 32; (d) D. Bradshaw, T. J. Prior, E. J. Cussen, J. B. Claridge, M. J. Rosseinsky, *J. Am. Chem. Soc.* **2004**, 126, 6106; (e) M. Dinca, J. R. Long, *J. Am. Chem. Soc.* **2005**, 127, 9376; (f) T. K. Maji, K. Uemura, H.-C. Chang, R. Matsuda, S. Kitagawa, *Angew. Chem.* **2004**, 116, 3331; *Angew. Chem. Int. Ed.* **2004**, 43, 3269; (g) K. S. Suslick, P. Bhyrappa, J.-H. Chou, M. E. Kosal, S. Nakagaki, D. W. Smithenry, S. R. Wilson, *Acc. Chem. Res.* **2005**, 38, 283; (h) R.-G. Xiong, X.-Z. You, B. F. Abrahams, Z. Xue, C.-M. Che, *Angew. Chem.* **2001**, 113, 4554; *Angew. Chem. Int. Ed.* **2001**, 40, 4422.
- 53** (a) B. Kesanli, W. Lin, *Coord. Chem. Rev.*, **2003**, 246, 305; (b) M. E. Davis, *Nature*, **2002**, 417, 813.
- 54** (a) M. Fujita, Y.-J. Kwon, S. Washizu, K. Ogura, *J. Am. Chem. Soc.* **1994**, 116, 1151; (b) J. S. Seo, D. Wand, H. Lee, S. I. Jun, J. Oh, Y. Jeon, K. Kim, *Nature* **2000**, 404, 982; (c) C.-D. Wu, A. Hu, L. Zhang, W. Lin, *J. Am. Chem. Soc.* **2005**, 127, 8940; (d) O. R. Evans, H. L. Ngo, W. Lin, *J. Am. Chem. Soc.* **2001**, 123, 10395; (e) T. Dewa, T. Saiki, Y. Aoyama, *J. Am. Chem. Soc.* **2001**, 123, 502; (f) O. Ohmori, M. Fujita, *Chem. Commun.* **2004**, 1586.
- 55** (a) C. D. Wu, W. Lin, *Chem. Commun.* **2005**, 3673; (b) C.-D. Wu, W. Lin, *Angew. Chem.* **2005**, 117, 1994; *Angew. Chem. Int. Ed.* **2005**, 44, 1958; (c) Y. Cui, S. J. Lee, W. Lin, *J. Am. Chem. Soc.* **2003**, 125, 601; (d) C. J. Kepert, T. J. Prior, M. J. Rosseinsky, *J. Am. Chem. Soc.* **2000**, 122, 5158.
- 56** D. N. Dybtsev, A. L. Nuzhdin, H. Chun, K. P. Bryliakov, E. P. Talsi, V. P. Fedin, K. Kim, *Angew. Chem. Int. Ed.* **2006**, 45, 916.
- 57** (a) L. Ma, C. Abney, W. Lin, *Chem. Sov. Rev.*, **2009**, 38, 1248; (b) B. Kesanli, W. Lin, *Coord. Chem. Rev.* **2003**, 246, 305.
- 58** R. Xiong, X. You, B. F. Abrahams, Z. Xue, C. Che, *Angew. Chem. Int. Ed.*, **2001**, 40, 4422.
- 59** D. Bradshaw, T. J. Prior, E. J. Cussen, J. B. Claridge, M. J. Rosseinsky, *J. Am. Chem. Soc.*, **2004**, 126, 6106.
- 60** G. Li, W. Yu, J. Ni, T. Liu, Y. Liu, E. Sheng, Y. Cui, *Angew. Chem. Int. Ed.*, **2008**, 47, 1245.
- 61** G. Li, W. Yu, Y. Cui, *J. Am. Chem. Soc.*, **2008**, 130, 4582.

- 62** R. Dawson, A. I. Cooper, D. J. Adams, *Progress in polymer science*, **2012**, 37, 530.
- 63** A. Cote, A. Benin, N. Ockwig, M. O’Keefe, A. Matzeger, O. M. Yaghi, *Science*, **2005**, 310, 1166.
- 64** H. Furukawa and O. M. Yaghi, *Science*, **2007**, 131, 8875.
- 65** N. B. McKeown, P. M. Budd, K. J. Msayib, B. S. Ghanem, E. J. Kingston, C. E. Tattershall, S. Makhseed, *Chem. Eur. J.*, **2005**, 11, 2610.
- 66** (a) N. B. McKeown and P. M. Budd, *Chem. Soc. Rev.*, **2006**, 35, 675; (b) M. D. Allendorf, A. Schwartzberg, V. Stavila, A. A. Talin, *Chem. Eur. J.*, **2011**, 17, 11372.
- 67** Lee J. Y., Wood C. D., Bradshaw D., Rosseinsky M. J., Cooper A. I., *Chem. Commun.*, **2006**, 2670.
- 68** J. X. Jiang, A. Trewin, C. D. Wood, N. L. Campbell, C. Dickinson, M. J. Rosseinsky, Y. Z. Khimyak, A. I. Cooper, *Angew. Chem. Int. Ed.*, **2007**, 46, 8574.
- 69** (a) T. Ben, H. Ren, H. Ma, D. Cao, J. Lan, X. Jing, W. Wang, J. Xu, F. Deng, J. M. Simmons, S. Qui, G. Zhu, *Angew. Chem. Int. Ed.*, **2009**, 48, 9457; (b) T. Ben and S. Qui, *CrystEngComm*, **2013**, 15, 17; (c) M. H. Alkordi, Y. Belmabkhout, A. Cairns and M. Eddaoudi, *IUCrJ.*, **2017**, 4, 131.

Chapter 2

Microporous materials: gas adsorption characterization

All the processes concerning the solid surface of materials are of vital importance, both from a constructive (for example, catalysis) and a destructive (corrosion) point of view. Chemistry itself develops in a different way on the surface, because new reaction paths with a lower activation energy barrier can be available. In recent years, the concept of *solid surface* has been largely extended, due to the properties of microporous materials¹. Physical adsorption is a technique used to characterize the surface of the solids. It consists in exposing a carefully prepared sample to a proper gas. When a gas molecule randomly encounters the surface of the sample, it is attracted to the surface by the intrinsic surface energy of the material. The forces that bring about adsorption include attractive and repulsive ones, in addition to the Coulombic forces, if either the solid and the gas is polar in nature. As the pressure is increased, the number of molecules bounded increases too, and then, the quantity adsorbed. The number of adsorbed molecules at any time is a function of the increasing pressure. As the pressure increases, multiple layers of molecules are formed on the pore walls, till the surface is completely covered.

2.1 Physisorption

To avoid ambiguities, IUPAC recommends to specify the following definitions². The *adsorbent* is the material into which adsorption takes place- The *adsorptive* is the substance to be adsorbed or after it has been adsorbed, while the *adsorbate* is the substance when it is in the adsorbed state. When there is adhesion to the surface by atoms or molecules from a gas, liquid or dissolved solid, the phenomenon is known as adsorption, whereas *absorption* occurs when atoms and molecules enter in the bulk phase. Guest entities can be bonded to the surface in two ways. We talk about *physisorption* when there is a van der Waals interaction between the adsorbent and the adsorbate. The van der Waals interactions are long-distance but weak forces, thus the energy involved in physisorption is approximately the same of condensation. Energies of this kind are assimilated by the solid through lattice vibrations and are dissipated as thermal stirring. The physisorption enthalpy can be measured by the temperature increase of a sample with known thermal capacity and the typical values are around 20 kJ/mol. This tiny enthalpy variation is not enough to break bonds, therefore the molecule adsorbed

retains its chemical identity. The forces involved in physisorption are of the same kind as those responsible for the imperfection of real gases and the condensation of vapors, and which do not involve a significant change in the electronic orbital patterns of the species involved. Some features which are useful in recognizing physisorption include:

- I. the phenomenon is a general one and occurs in any solid/fluid system, although certain specific molecular interactions may occur, arising from particular geometrical or electronic properties of the adsorbent and/or adsorptive;
- II. evidence for the perturbation of the electronic states of adsorbent and adsorbate is minimal;
- III. the adsorbed species are chemically identical with those in the fluid phase, so that the chemical nature of the fluid is not altered by adsorption and subsequent desorption;
- IV. the energy of interaction between the molecules of adsorbate and the adsorbent is of the same order of magnitude as, but is usually greater than, the energy of condensation of the adsorptive;
- V. the elementary step in physical adsorption from a gas phase does not involve an activation energy. Slow, temperature dependent, equilibration may however result from rate-determining transport processes;
- VI. in physical adsorption, equilibrium is established between the adsorbate and the fluid phase. In solid/gas systems at not too high pressures the extent of physical adsorption increases with increase in gas pressure and usually decreases with increasing temperature. In the case of systems showing hysteresis the equilibrium may be metastable;
- VII. under appropriate conditions of pressure and temperature, molecules from the gas phase can be adsorbed in excess of those in direct contact with the surface (multilayer adsorption or filling of micropores).

The physisorption technique is that useful to classify and to characterize porous materials:

- porous materials with pore widths exceeding about 50 nm are called **macroporous**;
- porous materials with pore widths between 2 nm and 50 nm are called **mesoporous**;
- porous materials with pore widths not exceeding about 2 nm are called **microporous**.

These limits are really arbitrary since the pore filling mechanisms are dependent on the pore shape and are influenced by the properties of the adsorptive and by the adsorbent-adsorbate interactions. It is important to precise that the accessible volume present in micropores is regarded as adsorption space and the *micropores filling* is a primary physisorption process; on the contrary, about macropores and mesopores, it is possible to speak about surface coverage of walls and the physisorption takes place in two or more distinct stages (monolayer-multilayer adsorption and capillary condensation). In *monolayer condensation* all the adsorbed molecules are in contact with the surface layer of the adsorbent. In *multilayer adsorption* the adsorption space accommodates

more than one layer of molecules so that not all adsorbed molecules are in direct contact with the surface layer of the adsorbent. In *capillary condensation* the residual pore space which remains after multilayer adsorption has occurred is filled with condensate separated from the gas phase by menisci. Capillary condensation is often accompanied by hysteresis. The term capillary condensation should not be used to describe micropore filling. For physisorption, the *monolayer capacity* (n_m) is usually defined as the amount of adsorbate needed to cover the surface with a complete monolayer of molecules. The *surface coverage* (θ) is defined as the ratio of the amount of adsorbed substance to the monolayer capacity. The *surface area* (A_s) of the adsorbent may be calculated from the monolayer capacity (n_m^a , in moles) provided that the area (a_m) effectively occupied by an adsorbed molecule in the complete monolayer is known. Thus,

$$A_s = n_m^a N_A a_m$$

where N_A is the Avogadro constant. The *specific surface area* (a_s) refers to unit mass of adsorbent:

$$a_s = \frac{A_s}{m}$$

In the case of micropore filling, the interpretation of the adsorption isotherm in terms of surface coverage may lose its physical significance, for this reason, sometime, it may be convenient to define a *monolayer equivalent area* calculated from the amount of adsorbate required to fill the micropores.

2.2 Chemisorption

In the second case, molecules and atoms create a chemical bond with the surface: this phenomenon is known as *chemisorption*. The enthalpy of chemisorption is higher compared to physisorption and the average value is 200 kJ/mol. When it is chemisorbed, a molecule can be broken to satisfy the incomplete valence bands of the atoms on the surface and this represents the reason why solid surfaces can be used as catalysts. The adsorption enthalpy depends on the fractional occupancy of the adsorption sites θ thanks to the interaction between the adsorbate particles. If the interaction is repulsive, the adsorption becomes less exothermic as the molecules spread to cover the entire surface. If the interaction is attractive, the guest molecules tend to form clusters and from their borders the expansion on the surface keeps on³. The forces involved are valence forces of the same kind as those operating in the formation of chemical compounds. The problem of distinguishing between chemisorption and physisorption is basically the same as that of distinguishing between chemical and physical interaction in general. No absolutely sharp distinction can be made and intermediate cases exist, for example, adsorption involving strong hydrogen bonds or weak charge transfer. Some features which are useful in recognizing chemisorption include²:

- I. the phenomenon is characterized by chemical specificity;

- II. changes in the electronic state may be detectable by suitable physical means (e.g. u.v., infrared or microwave spectroscopy, electrical conductivity, magnetic susceptibility);
- III. the chemical nature of the adsorptive(s) may be altered by surface dissociation or reaction in such a way that on desorption the original species cannot be recovered; in this sense chemisorption may not be reversible;
- IV. the energy of chemisorption is of the same order of magnitude as the energy change in a chemical reaction between a solid and a fluid: thus chemisorption, like chemical reactions in general, may be exothermic or endothermic and the magnitudes of the energy changes may range from very small to very large;
- V. the elementary step in chemisorption often involves an activation energy;
- VI. where the activation energy for adsorption is large (*activated adsorption*), true equilibrium may be achieved slowly or in practice not at all. For example, in the adsorption of gases by solids the observed extent of adsorption, at a constant gas pressure after a fixed time, may in certain ranges of temperature increase with rise in temperature. In addition, where the activation energy for desorption is large, removal of the chemisorbed species from the surface may be possible only under extreme conditions of temperature or high vacuum, or by some suitable chemical treatment of the surface;
- VII. since the adsorbed molecules are linked to the surface by valence bonds, they will usually occupy certain *adsorption sites* on the surface and only one layer of chemisorbed molecules is formed.

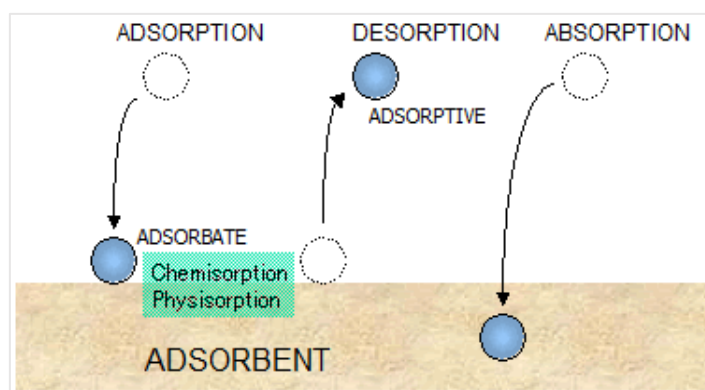


Figure 1. IUPAC definitions in surface characterization².

2.3 Adsorption isotherm

Adsorption starts to build up as the gas pressure increases. However, we often referred to relative pressure rather than absolute pressure. Relative pressure is simply the ratio of absolute pressure to the saturation pressure, being the saturation pressure the vapor pressure of the pure liquid. During an adsorption analysis, the absolute pressure approaches the saturation pressure, which, for the most commonly used gases, is close to atmosphere pressure. At this point, adsorption is maximum. As the pressure is systematically reduced, desorption occurs. The quantity of molecules adsorbed, or desorbed, as a function of the relative pressure, is

known as adsorption or desorption *isotherm*, respectively. The shape of the adsorption isotherm is the fingerprint of the texture of the solid, as shown in Figure 2. Adsorption isotherms are currently classified in five classes (I - V) according to the Brunauer, Deming, Deming, Teller (BDDT) original classification, which is often referred to as the Brunauer, Emmet, and Teller (BET), or simply to as the Brunauer classification. An extra type of isotherm (the stepped Type VI isotherm, which is relatively rare) is also reported. Type IV and V isotherms typically exhibit a hysteresis loop, which is characteristic of porous systems, involving capillary condensation³.

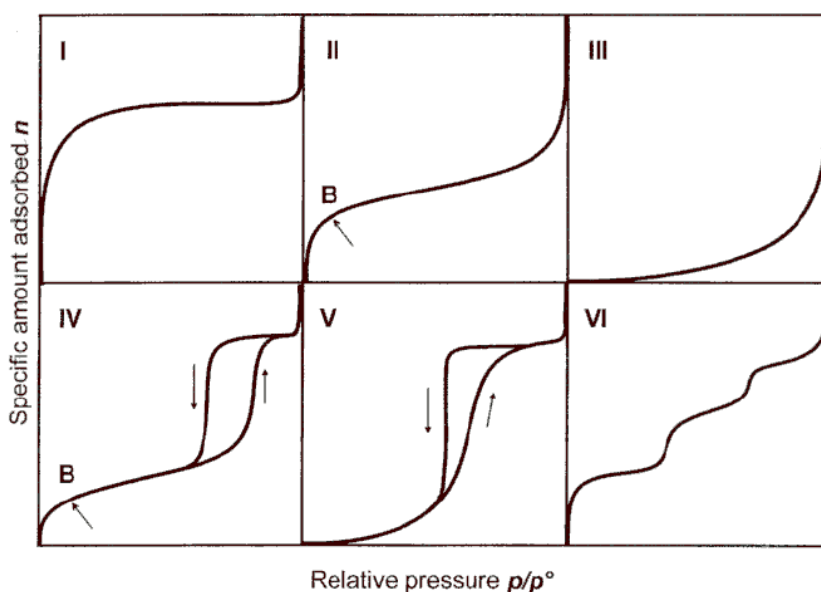


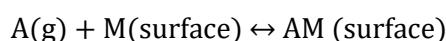
Figure 2. Types of physisorption isotherms³.

2.4 Langmuir isotherm

The simplest adsorption isotherm, namely the Type I in Figure 2, is based on three assumptions³:

- I. Adsorption is completed when the surface is covered by a monolayer
- II. All the adsorption sites are equivalent and the surface is uniform
- III. The attitude of a molecule to be adsorbed does not depend on the occupation rate of the near sites

The third assumption is based on the hypothesis that adsorbed molecules do not interact between each other. The dynamic equilibrium is:



with kinetic constants k_a for the adsorption and k_d for the desorption. The variation in time of the fractional occupancy, or coverage rate, θ is proportional to the partial pressure p of A and to the number of empty sites $N(1-\theta)$, where N is the total number of sites:

$$\frac{d\theta}{dt} = k_a p N(1-\theta)$$

The variation in time of θ due to desorption is proportional to the number of desorbed guests, $N\theta$:

$$\frac{d\theta}{dt} = -k_d N\theta$$

At the equilibrium, there is no variation and therefore we obtain the *Langmuir isotherm*:

$$\theta = \frac{Kp}{1 + Kp}$$

with $K = k_a / k_d$.

The fractional occupancy increases with pressure, and at high pressures, when the gas molecules are forced to cover every available site, it tends to 1. Different temperatures determine different isotherms and the dependence of K from temperature can help to quantify the *isosteric heat of adsorption*, the standard adsorption enthalpy at constant θ . Assuming K as equilibrium constant, we can apply the van't Hoff equation and obtain:

$$\left(\frac{\partial \ln K}{\partial T}\right)_\theta = \frac{\Delta_{ads}H}{RT^2}$$

The Langmuir isotherm is described by a sharp increase of the relative pressure at low coverage, which is followed by a *plateau*, usually before 0,1 of relative pressure. The *plateau* occurs because the pores of the host material are so narrow that they are filled at low pressure. Once the pores are filled, the remaining adsorption is on the exterior of the material. Therefore, this isotherm shape is associated with microporous solids, in which pores don't exceed 2 nm of diameter. If the isotherm conforms to the Langmuir model, a simple graph of pressure divided by the quantity adsorbed versus pressure will yield a linear relationship. The slope allows the numerical value of the monolayer capacity to be determined.

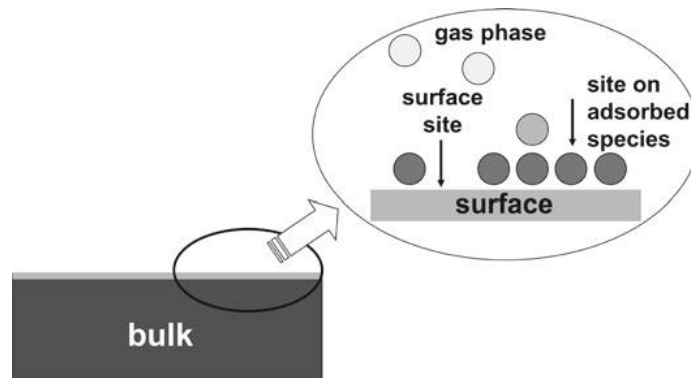


Figure 3. Schematic picture of adsorption process at the surface of a solid material³.

2.5 The BET isotherm

Deviations from the Langmuir model are often observed in real systems. The Langmuir model assumptions listed above are indeed very limitative and severe: (I) the solid surface is rarely uniform, there are always defects, (II) the mechanism of adsorption is not the same for the first molecules as for the last to adsorb. When two or more kind of sites characterized by different adsorption energies are present at the surface (as stated in point I), and when lateral interactions among adsorbed species occur (as stated in point II), the equivalence/independence of adsorption sites assumption fails. The most energetic sites are expected to be occupied first, and the adsorption enthalpy $\Delta_a H$ (per site) instead of keeping a constant, coverage-independent value, exhibits a declining trend as far as the coverage θ increases. Further, the adsorbed molecules are not necessarily inert, and on the top of the monolayer other molecules may adsorb and multi-layers build up: this is properly described by the Brunauer, Emmet and Teller (BET) model. When the first monolayer becomes a substrate for other layers of adsorbed molecules, the isotherm curve doesn't stop with the *plateau*, but it starts again to increase with pressure, as seen for Type IV in Figure 2. In this case, we can describe the adsorption curve with the *BET* model, named by Stephen Brunauer, Paul Emmett and Edward Teller, who postulated it in 1938⁴:

$$\frac{V}{V_{mon}} = \frac{cz}{(1-z)\{1-(1-c)z\}}$$

with $z = p/p^*$.

In this formula, p^* is the vapor pressure above a multilayer of adsorbate and V_{mon} is the volume of the first monolayer. The constant c is associated with the adsorption energy and it is significant when the desorption enthalpy from the monolayer is bigger than the vaporization enthalpy of the liquid adsorbate:

$$c = e^{(\Delta_{des}H - \Delta_{vap}H)/RT}$$

When $c \gg 1$ the BET isotherm becomes:

$$\frac{V}{V_{mon}} = \frac{1}{1-z}$$

This expression can be applied to inert gases on polar surfaces, for which $c = 10^2$, because $\Delta_{des}H \gg \Delta_{vap}H$. The BET method is the most used to estimate the surface area. As the pressure increases, the isotherm curves rise indefinitely, because, when a multilayer formation occurs, there is no limit to the quantity of molecules that can condense. The BET isotherm is not precise in all the range of pressures, because it underrates the fractional occupancy at low pressure and overestimates it at high pressure. The BET isotherm corresponds to mesoporous materials, with pore width ranging between 2 and 50 nm. Hysteresis is commonly observed in this

kind of porous materials, because the pore shape causes the adsorption and the desorption portions of the curve to have a different path.

2.6 The other isotherms

One of the basic assumptions of the Langmuir model is that all the adsorption sites are equivalent. Therefore, the deviations of the method from the experimental isotherms are caused by the failure of this hypothesis. For example, as θ rises, the adsorption enthalpy becomes less negative, showing that firstly, the most energetically favored sites are occupied. To supply these failings, other models were postulated. For example, the *Temkin equation*

$$\theta = c_1 \ln(c_2 p)$$

where c_1 and c_2 are constants, is based on the idea that the adsorption enthalpy varies with pressure in a linear way. Temkin equation too is a purely empirical formula, where θ represents the adsorbed amount and p the adsorptive pressure; c_1 and c_2 are suitable empirical constants for a given adsorbent-adsorbate pair at temperature T . Also in this case, the adsorbed amount is normalized either to the mass of the adsorbent or to the exposed surface area. The Temkin isotherm assumes that the adsorption enthalpy $\Delta_a H$ (per site) decreases linearly upon increasing coverage. On the other side, the *Freundlich equation*:

$$\theta = c_1 p^{\frac{1}{c_2}}$$

suggests a logarithmic trend between adsorption enthalpy and pressure³. It is the normal form of isotherm obtained with a nonporous or macroporous adsorbent or with a porous material in which there are different adsorption sites, some having high affinity and others having a low affinity for that specific adsorptive. The high affinity sites are occupied first and the point B indicates the stage at which monolayer coverage is complete and multilayer adsorption begins. In this case, the interactions substrate-substrate on the surface are included in the model. The Freundlich isotherm assumes that the adsorption enthalpy $\Delta_a H$ (per site) varies exponentially with increasing equilibrium pressure. The isotherms classification deals with ideal cases which in practical work are rarely encountered. Actually, most often the adsorption process over the whole interval of pressure is described by an experimental isotherm which does not fit into the classification. Nonetheless, each of the equations described above may be used over restricted ranges of equilibrium pressure, so allowing to describe the experimental isotherm through the combination of individual components to the process. In such a way the surface properties of the solid, and the thermodynamics features of processes taking place at the interface can be quantitatively described.

2.7 Adsorption hysteresis

Hysteresis appearing in the multilayer range of physisorption isotherms is usually associated with capillary condensation in mesopore structures. Such hysteresis loops may exhibit a wide variety of shapes, some of those represented in Figure 4.

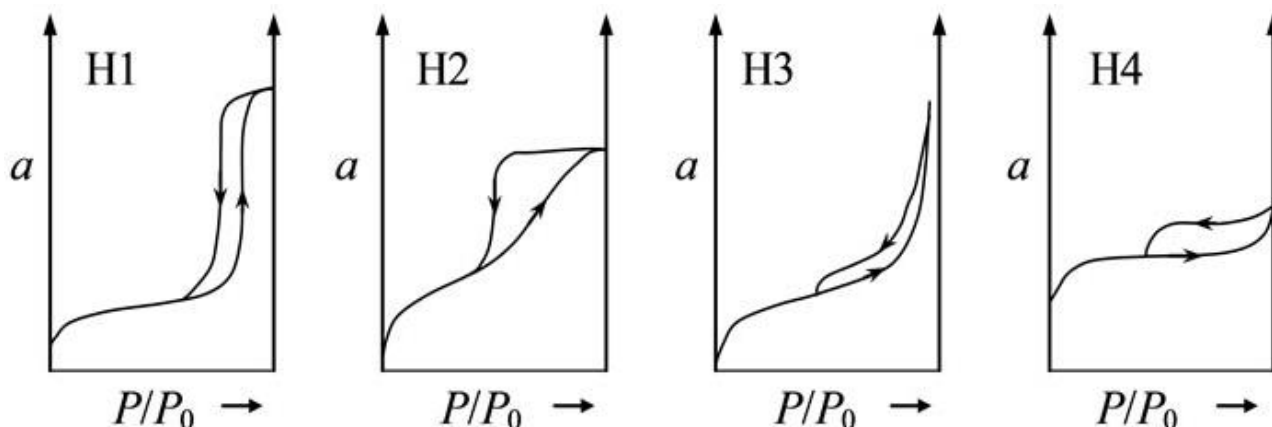


Figure 4. Types of hysteresis loops³.

H1 and H4 types are the two extremes: in the former the two branches are almost vertical and nearly parallel over an appreciable range of gas uptake, whereas in the latter they remain nearly horizontal and parallel over a wide range of p/p_0 . Types H2 and H3 are the intermediate between the previous two. A common feature is that the steep region of the desorption branch leading to the closure point occurs at a relative pressure which is almost dependent of the nature of the porous adsorbent but depends mainly on the nature of the adsorptive. The shape of hysteresis loops has often been identified with specific pore structures:

- Type H1 is associated with porous materials consisting of well-defined cylindrical-like pore channels or agglomerates or compacts of approximately uniform spheres in fairly regular array;
- Type H2 is due to disordered materials with not well-defined distribution of pore size and shape;
- Type H3 is observed with aggregates of plate-like particles giving rise to slit-shape pores;
- Type H4 is often associated with narrow slit-like pores and in the case of Type I isotherm it is indicative of microporosity.

With many systems, especially those containing micropores, low pressure hysteresis may be associated with the swelling of a non-rigid porous structure or with the irreversible uptake of molecules in pores of about the same width as that of the adsorbate molecule or in some instances with an irreversible chemical interaction of

the adsorbate with the adsorbent. In these systems the removal of the residual adsorbed molecules is then possible only if the adsorbent is outgassed at higher temperatures. It is widely accepted that two mechanisms contribute to the observed hysteresis³. The first mechanism has thermodynamic origins. At low pressure, a thin layer of vapor condenses onto the walls of the pore. With increasing pressure, the thickness of this layer increases, leading to a reduced radius of curvature for the liquid layer. Once a critical radius is reached, capillary condensation sets in and the whole pore fills with the liquid. When decreasing the pressure again, the liquid starts to evaporate and, accordingly, the pressure is lower. In the second mechanism the topology of the pore network plays a role. During the desorption process, vaporization can occur only from pores that have access to the vapor phase, and not from pores that are surrounded by other liquid-filled pores. There is a “pore blocking effect” in which a metastable liquid phase is preserved below the condensation pressure until the vaporization occurs in a neighboring pore. The relative pressure at which vaporization occurs depends on the size of the pore, the connectivity of the network, and the state of the neighboring pores. The adsorption process is dominated by the radius of the larger inner cavity while the desorption process is limited by the smaller neck.

2.8 Determination of surface area

Adsorption begins with relatively few molecules adsorbed on the surface as pressure starts to increase. At about relative pressure 0,05, the filling of the first layer on the surface has been established, which is reflected by the first inflection point on the isotherm. The linear region following the first increase is attributed to the multilayer adsorption. The Langmuir and BET models may be used to assess the monolayer capacity and to estimate the specific surface area. The *specific surface area*⁵ of a solid is the number of molecules in the monolayer multiplied by the surface area occupied by one molecule at the analysis temperature, divided by the sample mass.

$$\text{Specific surface area} = \frac{q_m \sigma N_a}{m}$$

where q_m is the monolayer capacity, σ is the surface area occupied by a molecule and N_a is the Avogadro number. It is calculated as it follows: the monolayer capacity, expressed in moles, determined by BET or Langmuir, is multiplied by the Avogadro number, to yield the number of molecules required to completely recover the surface. This number is multiplied by the area occupied by each molecule. To determine the specific surface area, the total surface area is divided by the mass of the sample. For materials with similar chemical composition, the general trend is that as the pore size decreases, the surface area increases. Therefore, to determine the surface area, the relative pressure doesn't need to exceed 0,4. There are many different procedures for the determination of the amount of gas adsorbed, but all of them are divided into two groups. The first, which depends on the measurement of the uptake of the gas by the adsorbent, is known as *gravimetric method*. To measure surface area and porosity, the *volumetric method*, which concerns the measurement of the amount of gas removed from the gas phase is mainly applied.

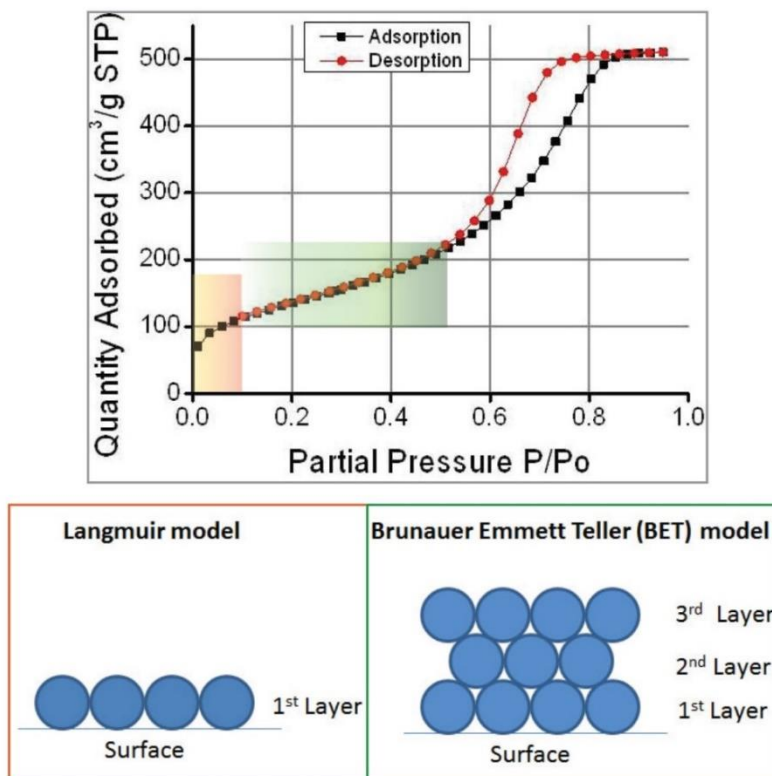


Figure 5. Comparison of Langmuir and BET models for gas adsorption^{3b}.

The volumetric method is based on the measurement of the gas pressure in a calibrated constant volume, at a known temperature. A known quantity of pure gas is usually admitted to a confined volume containing the adsorbent, previously outgassed and weighed, maintained at a constant temperature. As adsorption takes place, the pressure in the confined volume falls until equilibrium is established. The amount of gas adsorbed at the equilibrium pressure is given by the difference between the amount of gas admitted and the amount of gas required to fill the space around the adsorbent (*dead space*) at that pressure. The adsorption isotherm is constructed point-by-point by the admission of the adsorbent of successive charges of gas with the aid of a volumetric dosing technique and application of the gas laws. The volume of the dead space must be known accurately by a pre-calibration of the confined volume and subtracting the volume of the adsorbent. The amount of the adsorbed gas can be expressed by its mass or volume (often given in STP per unit mass; STP: standard pressure and temperature, namely 273,15 K and 760 Torr or 10⁵11325 Pa). Recent developments in vacuum microbalance techniques have revived the interest in gravimetric methods. The change in weight of the adsorbent may be followed directly during the outgassing and adsorption stages.

2.9 Ideal Adsorbed Solution Theory (IAST) Selectivity

In 1965, Prausnitz and Myers pioneered the work of ideal adsorbed solution theory or IAST in the article entitled “Thermodynamics of mixed-gas adsorption”⁶. IAST has been frequently used as the benchmark to

evaluate experimental data and to validate new theories for adsorption equilibria of gas mixtures. On the basis of solution thermodynamics, IAST is a predictive model which does not require any mixture data and is independent of the actual model of physical adsorption⁷. Because of the thermodynamic consistency, it has been used to study adsorption equilibria for gas mixtures which are ideal or non ideal and on surfaces which are homogeneous or heterogeneous⁸. Here, IAST is used to estimate the selectivity of all the samples for mixtures of CO₂ and N₂ both at 273 and at 298 K. The selectivity factor, S, is defined according to following equation, where n is the amount adsorbed of each component as determined from IAST and X is the mole fraction of each component in the gas phase at equilibrium, specifically X_{CO₂} is 0,15 and X_{N₂} is 0,85.

$$S = \frac{\frac{n_{CO_2}}{n_{N_2}}}{\frac{X_{CO_2}}{X_{N_2}}}$$

It is important to note that calculated IAST selectivities are highly dependent on the adsorption model used to describe the single component isotherm data. Specifically, isotherm fits at low pressures are most important for the strongest adsorbing component of a mixture (CO₂), while isotherms fit at high pressures are most important for the weakest adsorbing component (N₂).

2.10 Thermodynamics of adsorption

The adsorption of a gas at a solid surface is an exothermic process. This is required by the thermodynamic condition for a spontaneous process, illustrated by:

$$\Delta_a G = \Delta_a H - T \Delta_a S < 0$$

Actually, the adsorption phenomena are necessarily accompanied by a decrease in entropy ($\Delta_a S < 0$) because the degrees of freedom of the molecules in the adsorbed state are lower than in the gaseous state. Therefore, it turns out that the adsorption enthalpy change $\Delta_a H$ must be negative⁹. Since heat is not a state function, the value of the heat of adsorption depends on both the experimental conditions and the employed method of measurement. As a consequence, any physical interpretation of the experimentally determined heats of adsorption requires an accurate thermodynamic definition. Physical adsorption of gases on solid surfaces is caused by the attractive van der Waals interactions of gas molecules (adsorptive) with a solid (adsorbent). The interaction energy $U_S(z)$ of a gas molecule at distance z from a solid surface is approximately given as:

$$U_S(z) = - \frac{(\pi/6)C_{sf}\rho_s}{z^3}$$

where C_{sf} is a measure for the strength of attractive fluid-wall interactions and ρ_s represents the solid density¹⁰.

Physical adsorption of gases on solids is virtually always enthalpically driven. Entropically driven adsorption can exist but usually the entropy of molecules on a surface is much lower than in gas phase. Vibrational, rotational and translational degrees of freedom are restricted on surfaces. Sometimes it is useful to calculate the differential enthalpy of adsorption to characterize the energetic heterogeneity of solid surfaces. The simplest way to do it is to apply the isosteric method, which involves the measurement of at least two isotherms for that system, at different temperatures, and the application of the Clausius-Clapeyron equation on those systems. Integrating this equation, the isosteric heat formula results in:

$$\Delta H_{iso} = R \frac{\log \frac{p_2}{p_1}}{\frac{1}{T_1} - \frac{1}{T_2}}$$

where p and T are the pressure and the temperature and 1 and 2 indicate the two isotherms considered.

2.11 References

- 1 (a) K. S. Walton and R. Q. Snurr, *J. Am. Chem. Soc.*, **2007**, 129 (27), 8552; (b) D. M. E. *Nature*, **2002**, 417.6891, 813; (c) D. Avnir and M. Jaroniec, *Langmuir*, **1989**, 5 (6), 1431; (d) M. Thommes, K. Kaneko, A. V. Neimark, J. P. Olivier, F. Rodriguez-Reinoso, J. Rouquerol and K. S. W. Sing, *Pure Appl. Chem.*, **2015**, 87(9-10), 1051; (e) A. Galarneau, F. Villemot, J. Rodriguez, F. Fajula and B. Coasne, *Langmuir*, **2014**, 30 (44), 13266.
- 2 J. Rouquerol, D. Avnir, C. W. Fairbridge, D. H. Everett, J. H. Haynes, N. Pernicone, J. D. F. Ramsay, K. S. W. Sing and K. K. Unger, *Pure & Appl. Chem.*, **1994**, 66, 8, 1739.
- 3 (a) P. Atkins and J. De Paula, *Atkins' Physical Chemistry*, **2002**, 7th Ed., Oxford University Press; (b) <http://www.cchem.berkeley.edu/molsim/teaching/fall2011/CCS/Group7/adsorption.htm>.
- 4 S. Brunauer, P. H. Emmett and E. Teller, *J. Am. Chem. Soc.*, **1938**, 60 (2), 309.
- 5 A. D. McNaught and A. Wilkinson, *IUPAC Compendium of Chemical Terminology*, **1997**, 2nd Ed., Oxford, Blackwell Scientific Publications.
- 6 A. L. Myers and J. M. Prausnitz, *Thermodynamics of mixed-gas adsorption.*, **1965**, AIChE J., 11 (1), 121.
- 7 J. A. O'Brien and A. L. Myers, *Rapid calculations of multicomponent adsorption equilibria from pure isotherm data.*, *Ind. Eng. Chem. Process Des. Dev.* **1985**, 24 (4), 1188.
- 8 A. Ahmadpour, K. Wang and D. D. Do, *Comparison of models on the prediction of binary equilibrium data of activated carbons.*, *AIChE J.* **1998**, 44 (3), 740.
- 9 J.M. Thomas, W.J. Thomas, *Principles and Practice of Heterogeneous Catalysis*, VCH, Weinheim, Germany, **1997**; G. Attard, C. Barnes, *Surfaces. Oxford Chemistry Primers N. 59*, Oxford Science Publications, Oxford, **1998**.
- 10 Lu, G. Q.; Zhao, X. S. *Nanoporous Materials: Science and Engineering*, Imperial College Press, London, **2004**.

Chapter 3

Dipeptide-based crystals as volatile-drug vessels

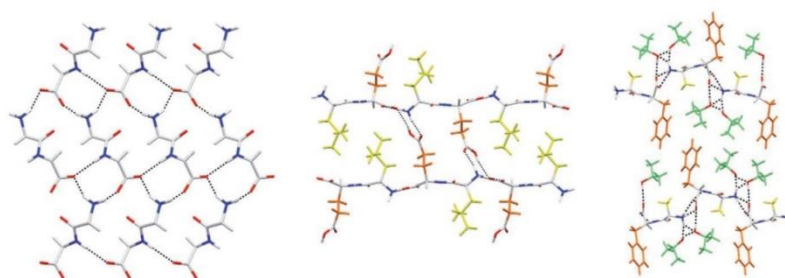
In recent years an intense development has occurred in the field of porous materials with nanometric channels, which improved the efficiency in the confinement and release of volatile molecules and gases¹. Indeed, hybrid materials, metal-organic and fully organic frameworks have been proposed in addition to the traditional inorganic materials, such as zeolites². Thus, the nature of the bonds sustaining the structure was extended to carbon-carbon covalent, organo-metallic and supramolecular interactions. As mentioned in the previous chapter, molecular porous materials are increasingly attractive since they are prone to self-assemble from their molecular constituents³. One of the most important feature is the permanent porosity, which allows to reuse the matrix for several absorption/desorption cycles without the reassembly of the material *ex novo*. Within this class, porous dipeptide crystals are outstanding for their biological origin, since they are formed by common proteinogenic amino-acids. Hybrid proteogenic/non-proteogenic dipeptide crystals enriched recently the library of molecular porous materials based on amino-acids^{4,5}. Porous dipeptides structures are self-assembled by crystallization from water (and guest hydrocarbons) and they are sustained by charge-assisted hydrogen bonding between ammonium and carboxylate end-groups to yield low-density, yet robust, crystalline materials. In addition, they are biodegradable and thus environmentally friendly, as opposed to the majority of porous materials. Thus far, they have been proposed for capture, sequestration and separation of gases of large interest for energetic and environmental purposes, such as carbon dioxide, methane and hydrogen⁶. Desorption step occurs easily under reduced pressure. Several further possibilities derived by their absorptive properties have been envisaged, such as gamma-ray polymerization of included monomers, in order to generate polymeric nanocomposites and oriented carbon nanofibers⁷. Such dipeptides are outstanding for their large variety of available channels. Supramolecular interactions as stable as charge assisted hydrogen bonding between ammonium and carboxylate end groups support the porous structure. They are biodegradable and thus environmentally friendly, as opposed to the majority of porous materials. However, their use as volatile drug vessels has never been explored⁸. Halogenated ethers and alkanes have extensive applications in general anesthesia, although there are still difficulties in their storage and delivery without dispersion into the environment⁹. Halothane, enflurane, desflurane and isoflurane, and the nonhalogenated diethyl ether, are among the most commonly used substances as anesthetics. These compounds, administered by inhalation, interact with GABA_A receptors in synaptic membranes and cause a reversible loss of consciousness¹⁰.

Moreover, most of them belong to the category of chlorofluorocarbon ethers (CFCs) and thus represent a constant danger for the environment¹¹. The use of biocompatible porous dipeptides for hosting/releasing volatile drugs appears particularly intriguing. The reduction of the vapor pressure of commonly-used volatile anesthetics upon nanoconfinement may give rise to practical advantages in handling and storage¹², as well as in delivery for controlled administration¹³. Herein we present adsorption isotherms of ultra-microporous dipeptide crystals and spectroscopic evidences for guest-anesthetic arrangement in the nanochannels. In particular, I investigated five porous dipeptides belonging to the Valyl-Alanine family: L-Valyl-L-Alanine (VA), L-Alanyl-L-Isoleucine (AI), L-Valyl-L-Valine (VV), L-Isoleucyl-L-Valine (IV) and L-Isoleucyl-L-Alanine (IA), whose hexagonal crystal structures (space group P_{61}) exhibit one-dimensional chiral channels⁴.

3.1 Microporous matrices from hydrophobic dipeptides

The pioneering work of Gorbitz¹⁴ illustrates the remarkable features and the 3D porous packing of crystalline dipeptide-based systems, also known as *biozeolites*. In particular, the dipeptides containing two hydrophobic residues have emerged as a new interesting class of microporous materials with pore diameters in the range 3–10 Å. The crystal structure of these matrices presents a challenging interpretation of their tridimensional porosity. Generally, dipeptides with sizeable hydrophobic side groups pack in hydrophobic and hydrophilic layers¹⁵, with the hydrophilic layers composed by head-to-tail chain $\text{-NH}^3+\cdots\text{-OOC}$ bonding motifs, as shown in Figure 1. The third H of the amino group lines to the close hydrophobic layer and it is usually accepted by a functional group in one of the side chain or by a co-crystallized solvent molecule¹⁶. In the case of dipeptides with two hydrophobic residues crystallized from solvents without strong hydrogen-bonding-accepting groups, the amino H has to find another way to arrange, highlighting the “packing problem” of these structures. Before Gorbitz et al. contribution¹⁴, only the crystal structures of the two dipeptides L-Alanyl-L-Alanine (Ala-Ala) and L-Methionine-L-Methionine (Met-Met) were known. The first is characterized by hydrophobic columns and a 3D hydrogen bond pattern belonging to the tetragonal space group¹⁷. The second is a 2D hydrogen bond layered structure. Both structures are not porous. In the review¹⁴ mentioned above, the combination of five amino acids have been investigated and their crystal structure is proposed in Figure 1. We can clearly understand that porous matrixes are obtained when both residues are Alanine, Valine or Isoleucine, which form the Val-Ala class, or when both side chains are Leucine or Phenylalanine, which represent the Phe-Phe family. Given this brief description on the crystalline arrangement of dipeptides, I will focus on the Val-Ala group, that include the five porous hosts I tested for the adsorption of anesthetic vapors.

a



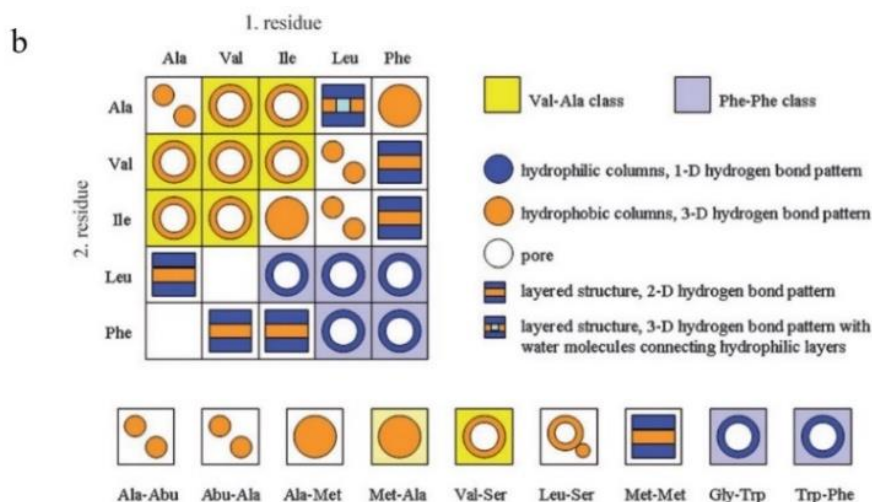


Figure 1. a) Left: Typical hydrophobic layer in a structure of a dipeptide. Middle: Acceptance of the third amino H atom by a side-chain carboxyl group in the structure of Val–Glu^{16a}. Right: Acceptance of the third amino H atom by a co-crystallized solvent molecule in the structure of Ala–Phe · 2-propanol (1:2)^{16b}.

b) General description of the structures of hydrophobic dipeptides showing pattern for separation between hydrophobic and hydrophilic moieties and the presence of pores¹⁴.

3.1.1 The Val-Ala class

The peptide dimer L-Valyl-L-Alanine (Val-Ala) is the head of the most important class of microporous crystalline dipeptide-based matrices. Val-Ala and the other isostructural dipeptides assemble into porous structure thanks to charge-assisted hydrogen bonds after the solvent removal. They crystallize in a honeycomb-shaped hydrogen-bonding network, with P_{61} space group, holding the left-handed double helices of the side-groups around the hexagonal axis. All the dipeptides mentioned above, L-Alanyl-L-Isoleucine (AI), L-Valyl-L-Valine (VV), L-Isoleucyl-L-Valine (IV) and L-Isoleucyl-L-Alanine (IA), belong to the Val-Ala family and therefore form an isostructural series. The structures and the pore space inside the hydrophobic channels of the Val-Ala class are illustrated in Figure 2. A model of the Val-Ala structure is presented in Figure 2. The number of chemical formula units per unit cell, Z , is 6 for all the dipeptides. The channels are formed half from one nanotube and half from the six parallel adjacent nanotubes. All the channels are isolated from each other. In the inner walls of the channels are lined the hydrocarbon fragments of both residues of the dipeptide molecule, giving a hydrophobic character to the pores space. The mono-dimensional nanotubes are inherently chiral and the pores can be adjusted within a considerable range by altering the size of the side groups. The pore sizes vary from the 5.01 Å (Val-Ala) to 3.41 Å (Ile-Val)^{4c}. The versatility of these systems is enhanced by the possibility of exchanging the amino acids in order to obtain different channels, as evident in the case of Ala-Ile (4.31 Å diameter) and Ile-Ala (3.61 Å). Another remarkable property of the Val-Ala family of dipeptides is that, after the solvent evacuation in vacuum at mild temperatures, the matrices retain their crystallinity and intrinsic porosity. Inside the empty channels, new guest molecules can be introduced from a liquid or gas phase. A model of the Val-Ala family structure is presented in Figure 3.

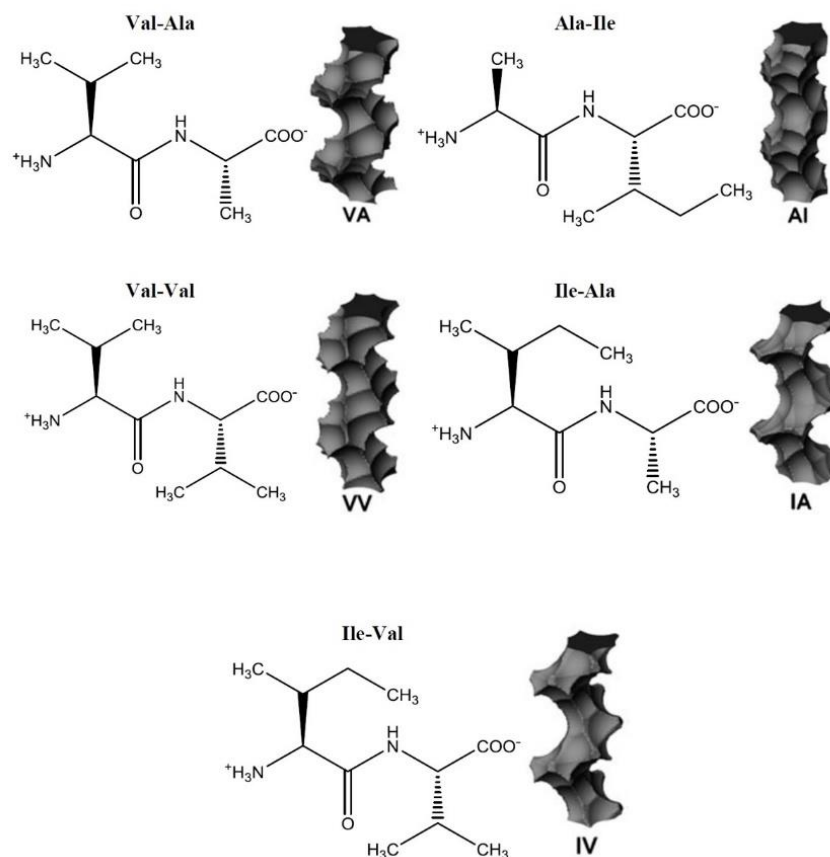


Figure 2. Structures and hydrophobic channels of the Val-Ala class dipeptides^{4c}.

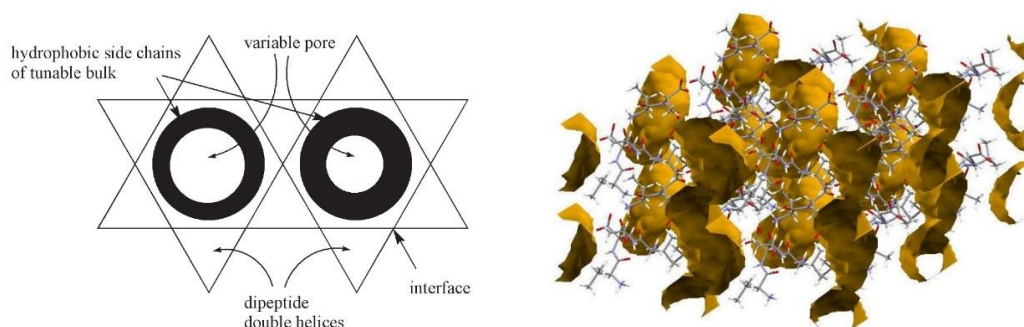


Figure 3. Illustration of Val-Ala class structure (left)¹⁸. Crystal channels of Val-Ala: cross-section of 5.1-5.3 Å (right).

3.1.2 Microporous materials for anesthetic drugs delivery

Many of the anesthetic agents currently used consist in halogenated molecules, belonging to the same class of chlorofluorocarbons (CFCs), and can be considered as aggressive greenhouse gases. Fluorinated anesthetics such as enflurane, isoflurane and halothane produce only the 0.03% of the global warming damage, but this percentage is very low because their concentrations in the atmosphere are negligible. If we consider the contribution per unit of mass, these drugs are quite dangerous. Furthermore, their tropospheric lifetimes are long (for example, from 1.2 years for sevoflurane to 10 years for desflurane) and their 20 year global warming

potentials (GWP₂₀) are three orders of magnitude higher than carbon dioxide¹⁹. The emission of these noxious vapors can be reduced by 80-90% if anesthesia was practiced in closed circuits; indeed, the global usage of inhalation anesthetics is growing fast, due to the fact general anesthesia becomes available to the world population, aggravating the environmental problem. This kind of volatile drugs is widely used also in dentistry, veterinary medicine and research activities involving *in vivo* experiments. In 2012, about 313.4 million surgical procedures were performed throughout the world²⁰ and all these data increases the request for materials able to store and recycle anesthetic agents and prevent their diffusion outside the clinical wards. From another point of view, the possibility to capture and reuse these volatile drugs can guarantee remarkable economic benefits. Moreover, the storage reduces the post-operation exposure of the medical personnel to the harmful anesthetic vapors and provide a well-defined control on the adsorption conditions, fundamental for controlled-release devices. The inhalation anesthetics are metabolized just in small amounts: to compensate, these drugs have to be administered in bigger quantities. For the treatment of volatile anesthetic agents, microporous materials represent the most promising technology and their adsorption properties have been investigated in the last years²¹. Both traditional absorbing materials (silica-gel, activated carbons, activated alumina, soda lime) and aluminosilicates, as for example zeolites, have been studied²². However, these materials lack of pore size tunability to entrap specific vapors and therefore should be substituted by more flexible solutions. In addition to inorganic materials, hybrid and fully organic frameworks, such as hydrogen bonded organic frameworks (HOFs), supramolecular organic frameworks (SOFs) and porous molecular crystals (PMCs), have been proposed³. Thanks to their easy self-assemble from the molecular building units, a great number of different structures can be synthesized, with large variety of pore sizes and shapes. Among the hydrogen bond-based 3D networks, the dipeptide crystals combine a high structural versatility with a biocompatible feature, given by the fact that the molecular constituents themselves come from the biological world. The dipeptides are outstanding not only for the large variety of channels and the permanent porosity, but also for their biodegradability, which makes them environmentally friendly, as opposed to the majority of porous materials. Their good stability, high tunability and biological origin allowed us to test them for the first time as volatile-drug vessels, owing the perspective of improving anesthesia clinical practice with a less dispersive and more efficient delivery system.

3.2 Administration of volatile anesthetics

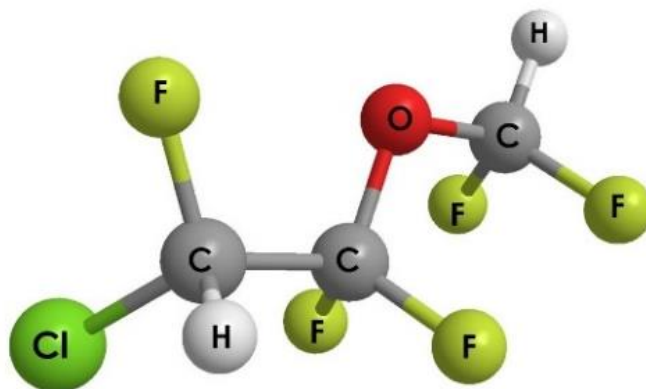
The administration of drugs is a process through which a xenobiotic, a generic molecule stranger to the organism, natural or synthetic, reaches the site of action where it is intended to perform its pharmacological function. There are two principal modalities of drug administration: the enteral routes, which includes the oral pathway, and the parenteral routes, in which the drugs are delivered through percutaneous tract or by inhalation. The inhalation route takes advantage of the airways and it has both a local and a systematic effect: the administration is made by nebulizers that vaporize the active or reduce it in small particles that are dispersed in the gas or in the air, pumped by a compressor. This method can be effectively used also with diseases that alter the gastrointestinal absorption, it doesn't require a particular training of the patients, and drugs can be

even inhaled without specialized staff. The only disadvantage is the need of a specific equipment. The oral is the less invasive route for the patient and it's the main way of medication, thanks to the possibility for the patient to comply the prescription and to complete the duration of the drug. Counter this administration has the principal problem of the reduced efficacy with gastrointestinal diseases, and drugs unstable to the gastric enzymes cannot be used with this method²³; secondly some patients do not appreciate it and have difficulties to swallow. An anesthetic is a drug that causes anesthesia, namely the reversible loss of sensation. Anesthetics differ from analgesics, which relieve pain without eliminating sensation. These drugs are generally administered to facilitate surgery. A wide variety of drugs are used in modern anesthetic practice. Anesthetics are categorized into two classes: general anesthetics, which cause a reversible global loss of consciousness, and local anesthetics, which cause a reversible loss of sensation for a limited region of the body while maintaining consciousness²⁴. For my thesis project, I worked with a particular class of general anesthetics, the inhaled agents, organic liquids with high vapor pressure, that easily pass into the vapor phase. Since their introduction into clinical use, in the middle of the 19th century, inhaled anesthetics were divided in three major groups: hydrocarbons, ethers, and other (non-carbon-based) gases. The first analgesic was nitrous oxide, but, due to its low potency, its use had to be supported by other agents. The hydrocarbons, like chloroform, cyclopropane and ethylene, and the diethyl ether were either highly toxic and/or explosive. Later, it was found out that halogenation could reduce the flammability of both alkanes and ethers. However, fluroxene, introduced in 1954, was later withdrawn from use because of residual combustibility. Halothane, the first noncombustible halogenated alkane, was introduced in clinical practice in 1956. Enflurane and isoflurane, structural isomers halogenated ethers, were first used clinically in 1972 and 1981, respectively. These anesthetics are less soluble in blood, compared to diethyl ether and halothane, and therefore can be fast adsorbed by the lungs and easily eliminated from the organism. This rapid uptake is quicker for sevoflurane and desflurane, in use for general anesthesia since the 1990s. The anesthetic agent which proved to have the best performances is xenon gas, introduced in 1951. Xenon has no taste nor odor, rapid pulmonary uptake and elimination, no hepatic or renal metabolism, and minimal cardiovascular depression and arrhythmogenicity. Nevertheless, the extraction of Xe from the atmosphere and its limited availability make it too expensive for a widespread use in clinical surgery²⁵. Taking into account all these considerations, the choice of halogenated drugs for the adsorption in nano-vessels was natural. In particular, I focused on *enflurane*, *isoflurane*, *halothane* and *desflurane*. Most of the halogenated anesthetics are irritating to the airway, perhaps leading to coughing, laryngospasm and overall difficult inductions. Even though these volatile agents can cause cardiopulmonary depression and death at concentrations near those that produce deep anesthesia, the clinical practice has reduced mortality to 1 per 250,000 patients²⁶. General anesthetics are used in surgery because they induce sedative effects that slow the stimuli responses, amnesia and loss of memory, insensitivity to pain, immobility and unconsciousness: for a long time, the anesthetics function was considered to depress the nervous system with a non-specific perturbation of the nerve membranes. Recent researches have showed that anesthetics action is more specific and it is promoted by a direct bond with proteins²⁷. A brief description of the inhale agents studied, of the

mechanism of action of general anesthesia and the relative pharmacokinetics will be illustrated in the next sections.

3.2.1 Enflurane

Enflurane (2-chloro-1,1,2-trifluoroethyl-difluoromethyl ether) is a halogenated ether. Developed by Ross Terrell in 1963, it was first used clinically in 1966. It was increasingly used for inhalational anesthesia during the 1970s and 1980s²⁸ but now it is used mostly in veterinary medicine. Enflurane is a structural isomer of isoflurane. It vaporizes readily, but is a liquid at room temperature. Enflurane is extremely stable and allows rapid adjustments of anesthesia depth with little change in pulse or respiratory rate. Enflurane induces muscle relaxation and reduces pains sensitivity by altering tissue excitability. Induction of and recovery from anesthesia with enflurane are rapid. Enflurane may provide a mild stimulus to salivation or tracheobronchial secretions. Pharyngeal and laryngeal reflexes are readily obtunded. In the cardiovascular system, enflurane is a mild negative inotrope, causing a marked decrease in systemic vascular resistance, thus leading to a decrease in mean arterial pressure. This results in a reflex tachycardia. Enflurane also decreases coronary vascular resistance and sensitizes the myocardium to circulating catecholamines. Enflurane is a strong respiratory depressant. It decreases tidal volume but may increase respiratory rate. It also causes bronchodilation and inhibits pulmonary macrophage activity and mucociliary activity. Enflurane principle action in the central nervous system is general anesthesia with little analgesic effect. It causes increased cerebral blood flow in concentrations and may induce tonic/clonic muscle activity and epileptiform EEG traces. It also causes a marked decrease in skeletal muscle tone. Actions in the genitourinary system include a decreased renal blood flow and glomerular filtration rate and the tone of pregnant uterus is decreased. Enflurane induces a reduction in junctional conductance by decreasing gap junction channel opening times and increasing gap junction channel closing times. Enflurane also activates calcium dependent ATPase in the sarcoplasmic reticulum by increasing the fluidity of the lipid membrane. It also appears to bind the D subunit of ATP synthase and NADH dehydrogenase. Enflurane also binds to and angonizes the GABA receptor, the large conductance Ca^{2+} activated potassium channel, the glycine receptor, and antagonizes the glutamate receptor. These yield a decreased depolarization and therefore, tissue excitability which results in anesthesia²⁹. The structure and the main properties of enflurane are shown in Figure 4.

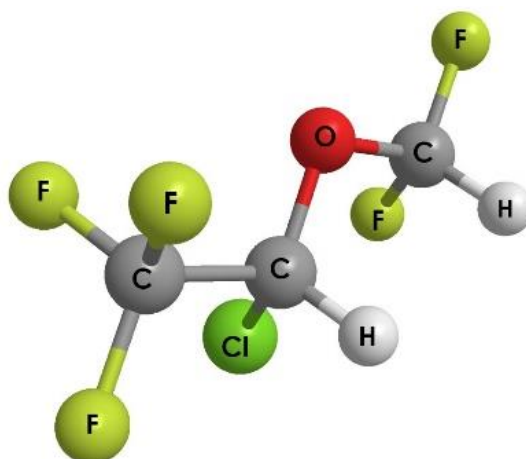


Property	Value
Boiling point at 1 atm (°C)	56.5
MAC	1.68
Vapor pressure at 20°C (kPa)	22.9
Blood:gas partition coefficient	1.9
Density (g/ml)	1.51
Volume (Å ³)	110.3

Figure 4. Structure (up) and principal physico-chemical characteristics (down) of enflurane.

3.2.2 Isoflurane

Isoflurane (*2-chloro-2-(difluoromethoxy)-1,1,1-trifluoro-ethane*) is a halogenated ether used for inhalational anesthesia. Together with enflurane and halothane, it replaced the flammable ethers used in the pioneer days of surgery. Its name comes from being a structural isomer of enflurane, hence they have the same empirical formula. It is a racemic mixture of (R) and (S) optical isomers. Its use in human medicine is now starting to decline, being replaced with sevoflurane, desflurane and the intravenous anesthetic propofol. Isoflurane is still frequently used for veterinary anesthesia. Isoflurane is always administered in conjunction with air and/or pure oxygen. Often nitrous oxide is also used. Although its physical properties imply that anesthesia can be induced more rapidly than with halothane²⁸, its pungency can irritate the respiratory system, negating this theoretical advantage conferred by its physical properties. It is usually used to maintain a state of general anesthesia that has been induced with another drug, such as thiopentone or propofol. It vaporizes readily, but is a liquid at room temperature. It is completely nonflammable. It induces muscle relaxation and reduces pains sensitivity by altering tissue excitability. It does so by decreasing the extent of gap junction mediated cell-cell coupling and altering the activity of the channels that underlie the action potential. Like enflurane, isoflurane activates calcium dependent ATPase in the sarcoplasmic reticulum by increasing the fluidity of the lipid membrane and binds to the GABA receptor, the large conductance Ca²⁺ activated potassium channel, the glutamate receptor and the glycine receptor²⁹. It is on the World Health Organization's List of Essential Medicines, a list of the most important medication needed in a health system³⁰.

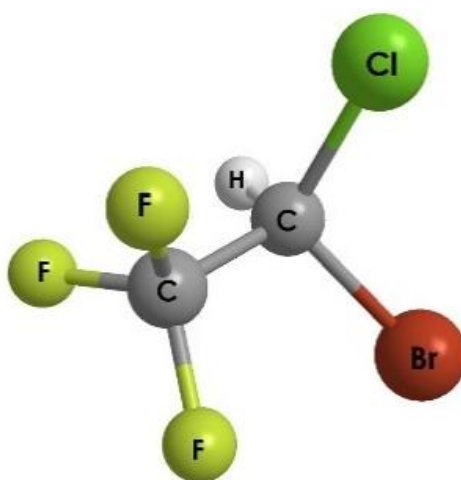


Property	Value
Boiling point at 1 atm (°C)	48.5
MAC	1.15vol%
Vapor pressure at 20°C (kPa)	32
Blood:gas partition coefficient	1.4
Density (g/ml)	1.51
Volume (Å ³)	108.3

Figure 5. Structure (up) and principal physico-chemical characteristics (down) of isoflurane.

3.2.3 Halothane

Halothane (*2-bromo-2-chloro- 1,1,1-trifluoroethane*) is a nonflammable, halogenated, hydrocarbon anesthetic that provides relatively rapid induction with little or no excitement. Analgesia may not be adequate. Nitrous oxide is often given concomitantly. Side effects include an irregular heartbeat, decreased effort to breathe (respiratory depression), and liver problems. It should not be used in people with porphyria or a history of malignant hyperthermia either in themselves or their family members³¹. Halothane causes general anesthesia due to its actions on multiple ion channels, which ultimately depresses nerve conduction, breathing, cardiac contractility. Its immobilizing effects have been attributed to its binding to potassium channels in cholinergic neurons. Halothane's effects are also likely due to binding to NMDA and calcium channels, causing hyperpolarization. It is on the World Health Organization's List of Essential Medicines³⁰.

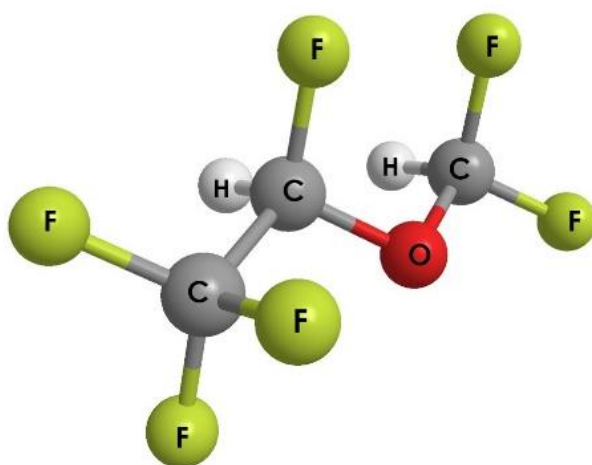


Property	Value
Boiling point at 1 atm (°C)	50.2
MAC	0.75vol%
Vapor pressure at 20°C (kPa)	32
Blood:gas partition coefficient	2.3
Density (g/ml)	1.86
Volume (Å ³)	88.7

Figure 6. Structure (up) and principal physico-chemical characteristics (down) of halothane.

3.2.4 Desflurane

Desflurane (*1,2,2,2-tetrafluoroethyl difluoromethyl ether*) is a highly fluorinated methyl ethyl ether used for maintenance of general anesthesia. Together with sevoflurane, it is gradually replacing isoflurane for human use. It has the most rapid onset and offset of the volatile anesthetic drugs used for general anesthesia due to its low solubility in blood. Some drawbacks of desflurane are its low potency, its pungency and its high cost. It may cause tachycardia and airway irritability when administered at concentrations greater than 10 vol%. Due to this airway irritability, desflurane is infrequently used to induce anesthesia via inhalation techniques. Desflurane preconditions human myocardium against ischemia through activation of mitochondrial K(ATP) channels, adenosine A1 receptor, and alpha and beta adrenoceptors²⁹.



Property	Value
Boiling point at 1 atm (°C)	23.5
MAC	6 vol%
Vapor pressure at 20°C (kPa)	88.5
Blood:gas partition coefficient	0.42
Density (g/ml)	1.46
Volume (Å ³)	134.8

Figure 7. Structure (up) and principal physico-chemical characteristics (down) of desflurane.

3.3 Pharmacokinetics

The drug development and design are carried out assessing the pharmacodynamic, namely the interaction between the drug and the target, whereas the pharmacokinetics focus on the ADME parameters: absorption, distribution, metabolism, elimination, that a drug must address before being approved by the FDA (Food&Drug Administration) for clinical use. To be effective, an anesthetic must have good pharmacokinetics characteristics. The absorption phase is very important and to evaluate the anesthetic goodness for the assimilation the *partition coefficient* (P) is used, a parameter that suggests the relative distribution in a n-octanol/water mixture of a lipophilic drug. The octanol well represents the characteristics of cell membranes,

therefore, if the drug concentration is higher in octanol, the drug will be hydrophobic; vice versa, it will be hydrophilic and water-soluble. Hydrophobicity is essential to cross the cell membranes and it can influence the interactions with the receptor. General anesthetics have *P* values of 2, that underlines their hydrophobic character and their adequate anesthetic power because they are able to cross the cell membranes. Once absorbed, the anesthetic passes into the bloodstream, is distributed to the most vascularized organs, as the central nervous system, the heart, the lungs and the liver, and subsequently to the targeted organs. After performing their action, the anesthetics must be metabolized and degraded to be eliminated from the body. In this phase the main role is played by the *P450 cytochrome*, a hemoprotein able to oxidize a part of the drug molecule through the homolytic splitting of an oxygen molecule: an oxygen atom will be incorporated in the drug and the other atom will bond to the water. So, the drug becomes polar, water-soluble and easily removed by the kidney.

3.4 Mechanism of general anesthesia

Anesthesia, considered as insensibility to surgical pain, is a complex phenomenon, still not completely understood and without an objective definition. The effects of inhaled anesthetics heavily depend on the concentrations administered: amnesia, euphoria, analgesia, hypnosis, excitation and hyperreflexia at low dosage; deep sedation, muscle relaxation and diminished motor and autonomic responses to noxious stimuli at higher levels. The potency of volatile anesthetics is determined through scales based on alveolar anesthetic concentrations, that are associated with defined behavioral end points. The most commonly used scale is the minimal alveolar concentration of anesthetic that suppresses purposeful movement in response to a standard noxious stimulus (MAC or MAC-immobility)³². The median alveolar concentration (MAC) is the end-tidal concentration of inhaled anesthetic that ablates movement in response to surgical incision in 50% of a test population. MAC is a synonymous with MAC-immobility. MAC-immobility increases as the intensity of the stimulus increases. For more than a century, after their introduction in the clinical use, the mechanism of action of general anesthetics has been deeply investigated. The anesthetics reversibly bond to the central nervous system and their effects depend on their molecular structure properties. On the basis of the first experiments, the theory of Meyer and Overton³³ has dominated for years, and according to this model the anesthetizing power is strongly related to their relative solubility in apolar solvents and therefore the cell membrane is the first site for the anesthetics action. The anesthetic molecules are able to dissolve in the cell membrane perturbing it and changing its cell functions. This theory has been supported by several experimental tests. However, this lipid theory has been almost completely abandoned, because the effects of anesthetics on the cell membranes are negligible³⁴. Furthermore, it now appears unlikely that the different classes of inhaled anesthetics act through a single common mechanism. Anesthetics act on different regions of the nervous system. The anesthetic-induced ablation of movement in response to pain is mediated primarily by the spinal cord³⁵. General anesthetics decrease the transmission of noxious information ascending from the spinal cord to the brain³⁶. Above the spinal cord, inhaled agents globally depress blood flow and glucose metabolism and selectively depress several supra-spinal regions³⁷. Although it has been found yet a correlation between specific

regions of the brain and inhaled anesthetics, researchers focused on structures with roles in anesthetic-sensitive functions. Therefore, the research shifted the focus on proteins: general anesthetics are known for their interactions with small cavities within most globular proteins, but with considerable selectivity³⁸. Thanks to the increasing number of crystalline structures with ionic channels well-resolved and to other integral membrane proteins, as well as to the abundance of powerful computers, the function-structure relation of the anesthetic and its interactions with the proteins can be studied in detail.

3.5 Interactions between anesthetics and proteins

Anesthetic agents influence the functions of a wide number of proteins, which mostly belong to the cytoplasmic signaling groups, but the most likely molecular targets are the ion channels. Ion channels are proteins that regulate the flow of ions across the cytoplasmic membrane. At clinical levels, the ion channels most involved in the anesthesia mechanism are the “cysteine-loop” neurotransmitter receptors, which include nicotinic acetylcholine, serotonin type 3, GABA_A and the glycine receptors, and the glutamate receptors³⁹. Within synapses, ion channels can influence the presynaptic release of neurotransmitters and alter the postsynaptic excitability in response to the release of neurotransmitters. Inhaled agents are supposed to enhance inhibitory postsynaptic channel activity (GABA_A and glycine receptors) and inhibit excitatory synaptic channel activity²⁵(Fig. 8). The GABA_A receptors are the most abundant inhibitory neurotransmitter receptors in the human brain. General anesthetics at clinically effective levels increase receptors’ sensitivity to GABA_A and prolong the receptor-mediated inhibitory current after a pulse of GABA release. The modulation of GABA_A receptors is not enough to account for every effect of anesthetics. In addition to GABA_A receptors, other ion channels are involved in the anesthetic-induced immobility. In spinal motor neurons, volatile anesthetics augment the activity of glycine receptors⁴⁰ and inhibit postsynaptic N-methyl-D-aspartate (NMDA) and α -amino-3-hydroxy-5-methyl-4-isoxazolepropionic acid (AMPA) receptors⁴¹. Ion channels work within the lipid membranes and therefore it is complicated to understand if their modulation by anesthetic drugs is caused indirectly by changes in membrane structure or directly by binding to protein sites. At the beginning, the principal hypothesis was based on key-lock interaction between the membrane proteins and the volatile agents, but a large amount of evidence was produced against it⁴². Thanks both to experimental and computational studies^{43,44}, the modern theory proposes the idea that general anesthetics do not change the structure of the membrane proteins, but they are able to modify their dynamics; it is well known, actually, that dynamics of proteins in the microsecond-millisecond range is often coupled with their function. Therefore, it can be assumed that if inhaled general anesthetics frequently do not change the structure of their target protein, they are able to change its dynamics, especially the dynamics in the flexible loops that connect α -helices in a bundle, thus disrupting modes of motion essential for the protein function⁴⁵. However, deep investigations are still required to distinguish between specific and non-specific hypotheses concerning the real interaction of volatile general anesthetics with the human membrane receptors.

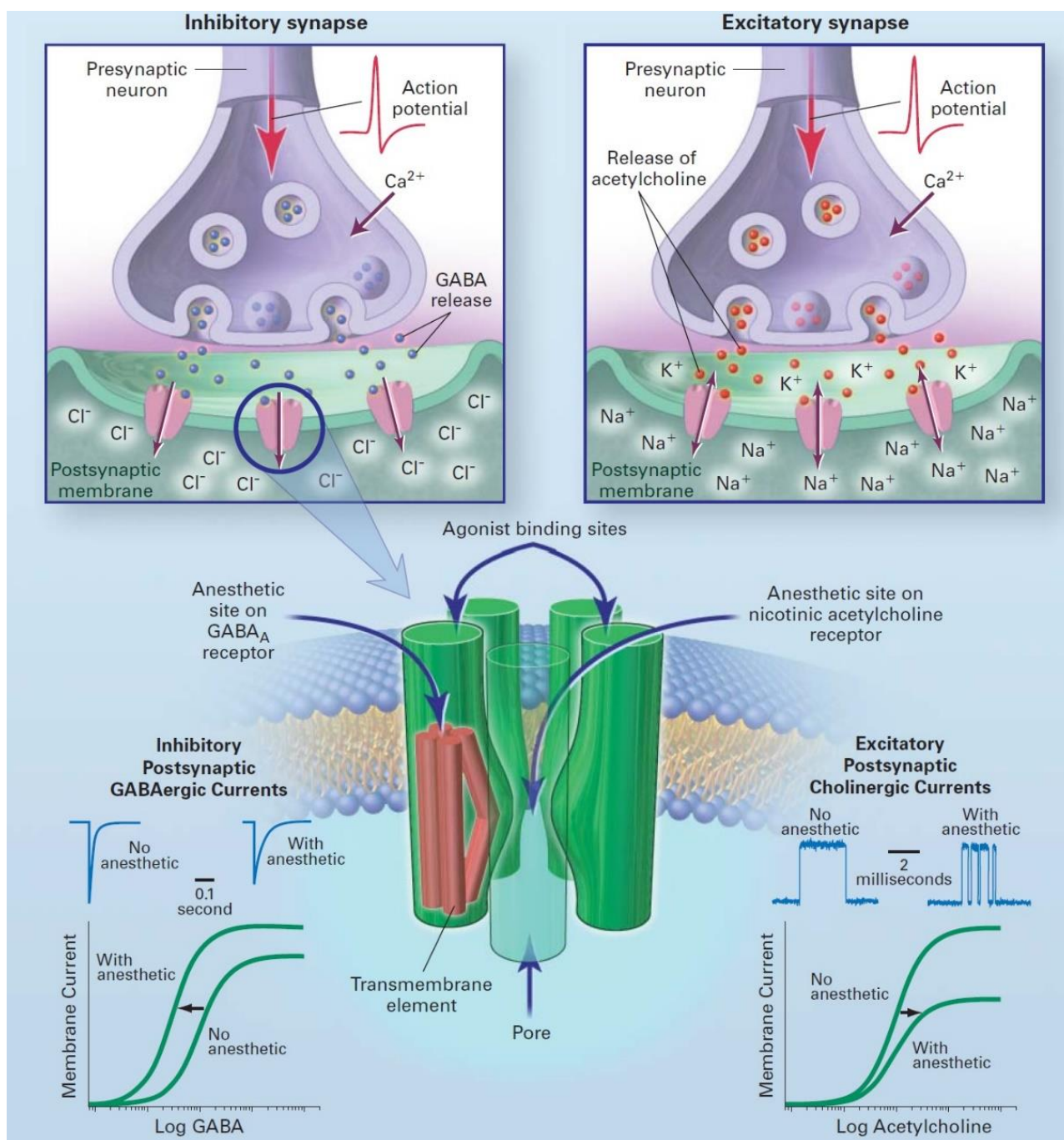
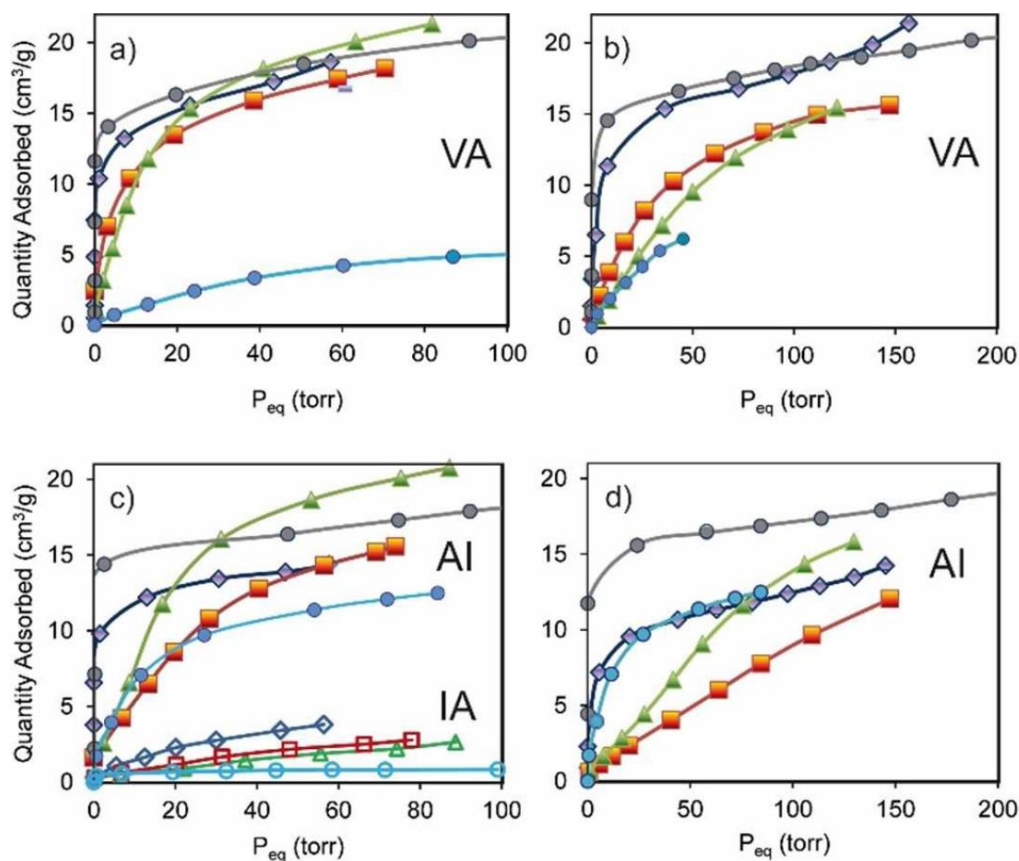


Figure 8. Effects of inhaled anesthetics on ion channels²⁵.

3.6 Anesthetics adsorption isotherms

This section is dedicated to the analysis of the adsorption isotherms of the above mentioned volatile anesthetics and diethyl ether, used as a reference, in the dipeptide crystals. The adsorption isotherms were measured through a vacuum system using the cumulative loading volumetric method. Indeed, adsorption experiments with halogenated vapors could not be estimated with the analytical Micromeritics instruments, because this kind of guests can be potentially dangerous for the analyzers. These fluorinated anesthetics can abrade the butadiene gauges present inside the systems to close the valves. Therefore, we exploited a manual tool, composed of a vacuum ramp and vacuum chambers of known volumes, closed by Teflon taps. The

experimental conditions are briefly discussed in Appendix A. Before the adsorption measurements, a weighted amount of the chosen dipeptide was thermally treated in vacuum at 60°C for 8 hours, in order to evacuate the nanochannels. The main warning concerning the use of dipeptides is that they cannot be heated at high temperature without risking the structural collapse, thus the removal of crystallization solvents and moisture can be sometimes challenging. Moreover, the dipeptides are bacteria-sensitive and they can be degraded if exposed to the atmosphere for a long period of time. Starting from these considerations, the pre-adsorption phases were realized avoiding a long open-air exposure of the matrixes. Two temperatures were chosen for the adsorption isotherm measurements, 273 and 298 K. This choice is justified by two main reasons: first, the manual vacuum systems does not provide a temperature-control system for the thermal bath in which the sample holder is dip; therefore, only simple thermal bath with water and ice mixed water could be employed. Then, at least two isotherms at different temperatures were necessary to calculate the isosteric heat of adsorption, i.e. the interaction energy between the host-framework and the guest-molecules, as described in Chapter 2. The maximum quantity adsorbed is higher at lower temperature because the kinetic energy of the guest molecules decreases reducing the temperature and, hence, they can be more easily captured by the porous matrixes. Vapor isotherms in Valyl-Alanine (VA), Alanyl-Isoleucine (AI) and Valyl-Valine (VV) were performed at 273 and 298 K, whereas in Isoleucyl-Valine (IV) and in Isoleucyl-Alanine (IA) only at 273 K. The last two dipeptides presented a very low adsorption capacity already at 273 K, with maximum loading lower than 5 cm³/g; for this reason, we chose not to perform the measurements at higher temperatures, since the adsorption would had been negligible.



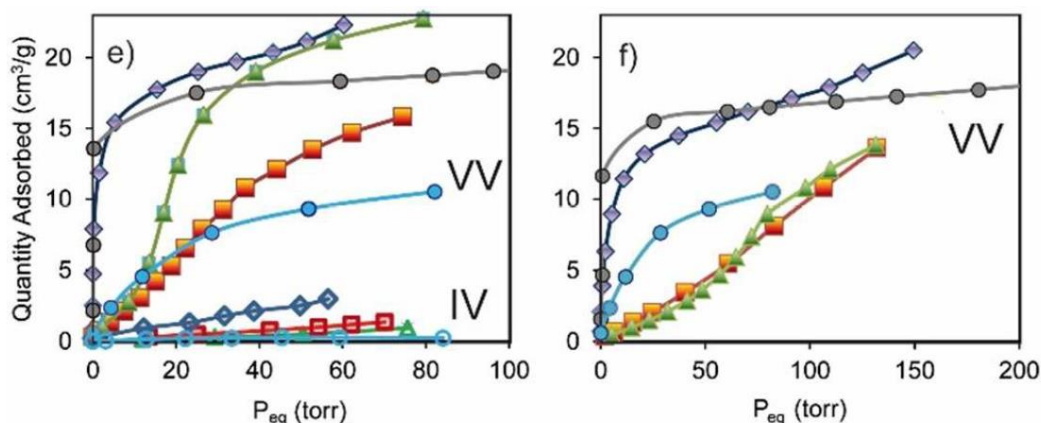


Figure 9. Anesthetics adsorption isotherms for dipeptides Val-Ala (a), Ala-Ile (b) and Val-Val (c) up to 100 torr and 200 torr, respectively. Ether (grey circle), enflurane (violet diamond), isoflurane (orange square), halothane (green triangle), desflurane (light blue circle). In IA and IV the labels are empty.

As shown in Figure 9, the adsorption isotherms in IV and IA do not present a Langmuir shape, whereas the curves display a linear trend with the increasing pressure. It was not possible to reach the vapor pressures, because the guests simply could not penetrate inside the matrixes and started to accumulate in the sample holder. Actually, pore size plays a key role in the selective recognition of the guests: matrixes with channels larger than 4 Å such as VA, AI and VV efficiently absorb the guests and reach maximum loading, whilst IA and IV with pore sizes of about 3.5 Å exclude the anesthetics. The steric hindrance of the halogenated guests prevents their capture inside the nanochannels of IA and IV, while in VA, VV and AI the pores can accommodate or adapt to the molecules dimensions. The vapor isotherms at 273 K in VA channels exhibited Langmuir-type profiles for all the halogenated guests, showing maximum absorption values of 170-200 mmol mol⁻¹ at 273 K and 80-100 torr, which corresponds to a virtually complete loading of available volume and more than 20% by weight, as shown in Figure 9. The only exception is the fully fluorinated desflurane, which displayed an uptake lower than 60 mmol mol⁻¹. The unit cell parameters of the samples upon loading remain substantially unaltered, indicating the zeolitic behavior of this molecular crystalline material (see PXRD in Figure 10 and in Appendix C). This structural robustness, clearly indicated by the negligible variations in the PXRD patterns, means that the VA dipeptide does not need to modify its cell parameters to host the anesthetic molecules, but its cross section is large enough to entrap the guests retaining the crystallinity. Therefore, the VA matrix resulted to be the most efficient adsorbent for this kind of halogenated guests. Langmuir-type isotherms for enflurane are also shown in the smaller channels of AI and VV, owing to the limited steric requirements of the chlorine on the terminal methyl group, which allows easy adjustment in the channels. On the contrary, the isotherms of isoflurane, enflurane's isomer bearing the chlorine substituent on the methylene group, and halothane (containing F, Cl and Br halogens) in VV do not follow a Langmuir profile. Isoflurane and halothane isotherms in AI do not follow the Langmuir profile either, and this behavior is accentuated at 298 K. This different behavior is particularly highlighted in the case of halothane in VV. In fact, in the channels of VV, halothane isotherms exhibited a minimal adsorption at low pressures followed by an increased uptake above 10 torr. Thus, at low pressures a selective absorption of enflurane with respect to halothane is exhibited.

This behavior is fully reproducible over a few cycles and can be attributed to the flexibility of the structure that expanded upon crossing a pressure threshold. The PXRD patterns of AI and VV, performed after the anesthetics adsorption, present too small changes in the cell parameters to indicate a structural rearrangement of the dipeptides and, moreover, they do not lose their crystallinity (see Appendix C).

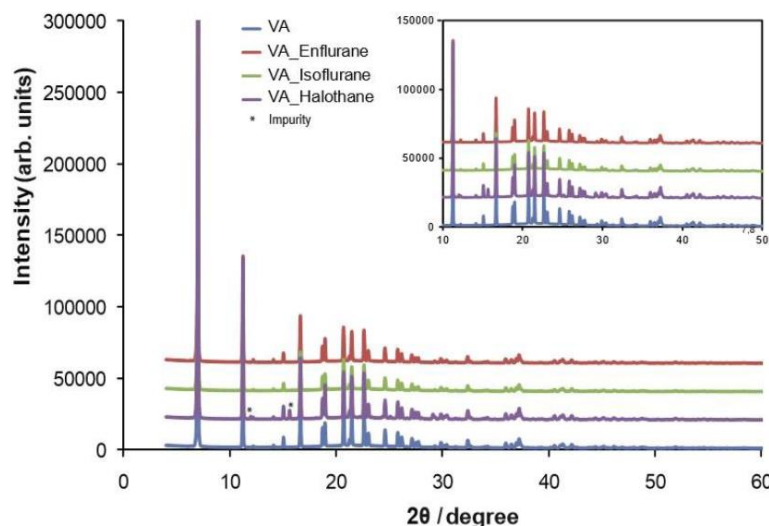


Figure 10. Powder X-ray diffraction patterns of empty Valyl-Alanine (blue) and with halogenated guests (red, enflurane; green, isoflurane; purple, halothane). The unit cell parameters of empty VA are the following: $a=14.46 \text{ \AA}$, $c=10.08 \text{ \AA}$, $V=1826.03 \text{ \AA}^3$, $\sigma=1 \times 10^{-4}$.

This phenomenon clearly proves the versatile nature of these porous materials, which are able to adequately and reassemble to host bulky molecules. Desflurane, bearing exclusively fluorine atoms as halogens and exhibiting the highest volatility (b.p. = 23°C), shows in all dipeptides modest absorption values at 273 K, particularly in VA, whilst diethyl ether is absorbed with high efficiency in the hydrocarbon environment. The diethyl ether, the only non-halogenated guest, established the highest quantities adsorbed in all the matrixes, following a perfect Langmuir-shape behavior. In the cases of VA, AI and VV, both at 273 and 298 K, all the guests reach maximum adsorption values at the vapor pressure in a range between 10 and $20 \text{ cm}^3/\text{g}$, with the only exception of desflurane. Desorption branches show complete reversibility of the isotherms and no hysteresis, indicating possible reuse of dipeptides without regeneration (see Appendix C). In Figure 11, enflurane adsorption and desorption isotherms at both temperatures are reported. The low boiling points of the volatile anesthetics allow their easy evacuation from the dipeptide crystals, by heating the matrixes at 60°C under vacuum, expanding therefore their possible applications for pre-surgery devices. From adsorption isotherms at various temperature, the isosteric heats of adsorption (values are reported in Appendix C) were evaluated by applying the Clausius-Clapeyron equation at low coverage degree. The values are in the range of $35\text{-}50 \text{ kJmol}^{-1}$, which demonstrate the strong affinity between the dipeptide hosts and the halogenated guests, owing to multiple interactions installed within the narrow channels. The higher is the maximum quantity adsorbed, the stronger is the interaction energy between the matrix and the guest, the higher is the isosteric heat of adsorption. These

adsorption energies are comparable to the highest values reported for adsorbed anesthetics in porous materials⁴⁶. Prompted by these good adsorption data, the next step was the measure of the crystallites dimensions, in order to understand their possibilities as vessels for anesthesia injection therapies. Dynamic Light Scattering analysis of a suspension of VA crystals proved that their particle size falls in the nanometric range with a distribution centered at about 30 nm. This evidence enforces the perspectives for the use of dipeptides in nanomedicine, because this dimension is suitable for blood stream transport and cell internalization (see Appendix C for the DLS particle size distribution graph).

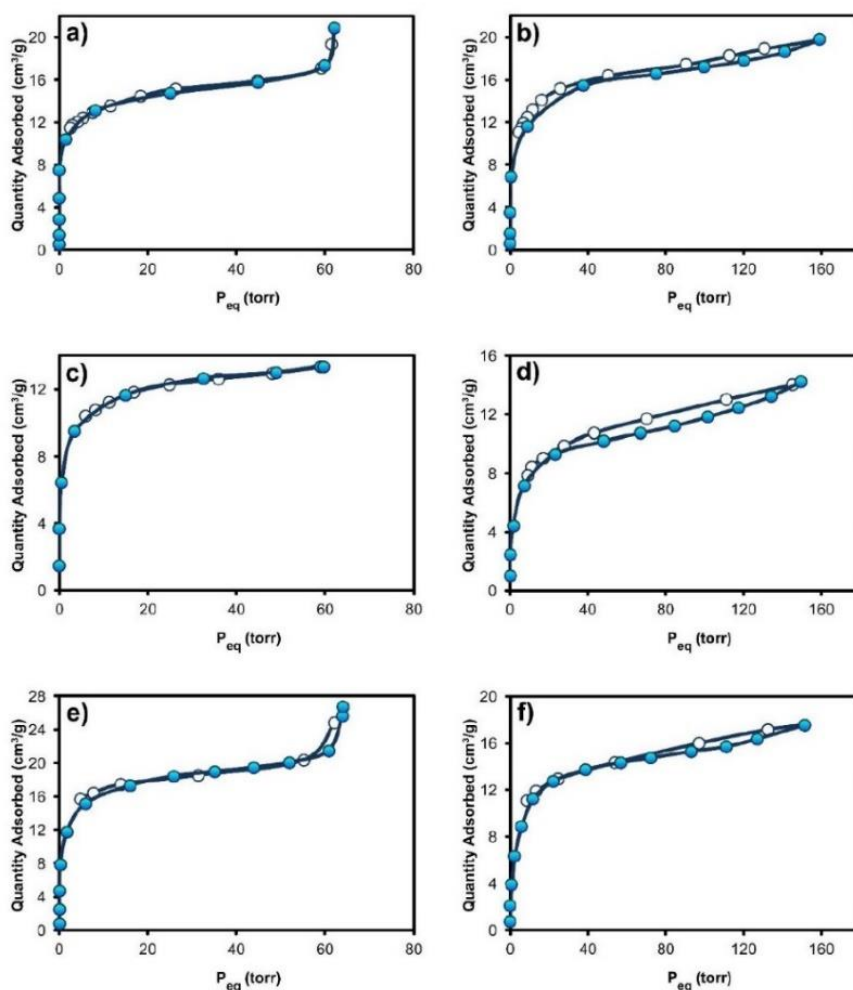


Figure 11. Adsorption/desorption isotherms of enflurane in VA at 273 K (a) and 298 K (b), in AI at 273 K (c) and 298 K (d), and in VV at 273 K (e) and 298 K (f).

3.7 NMR spectroscopic detection

After the adsorption properties, I focused on the solid-state NMR characterization of the host/guest adducts. Our purpose was to demonstrate from a spectroscopic point of view the presence of the anesthetic molecules inside the tubular channels of the three main dipeptides, namely VA, AI and VV. Since we proved their

capability to adsorb without dramatic structural changes the halogenated guests, also at room temperature, the following step was the investigation of the dipeptides/anesthetics reciprocal interactions.

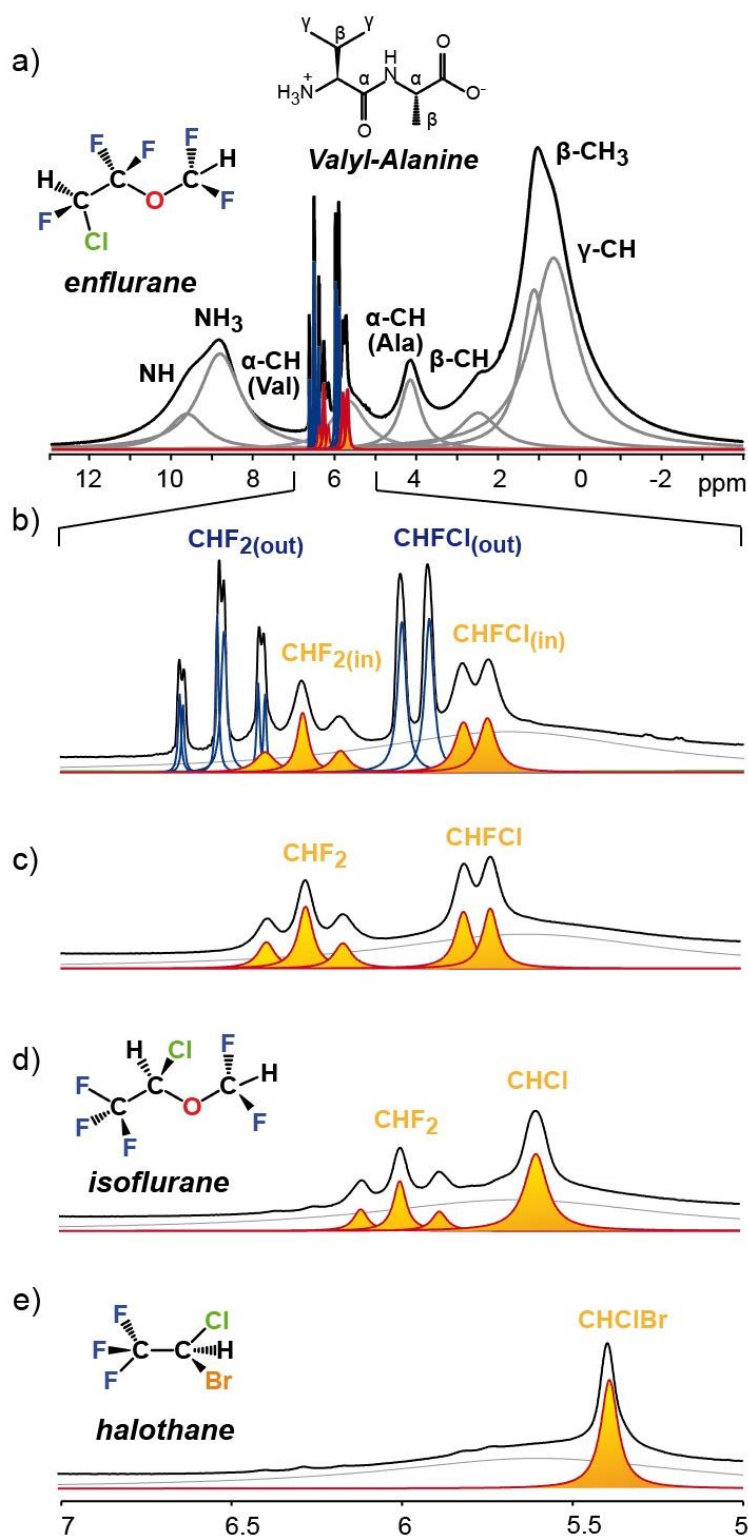


Figure 12. 600 MHz ^1H fast-MAS NMR (35 kHz spinning speed): a) VA with enflurane both inside and outside the nanochannels; b) enlargement of the above spectrum in the 5-7 ppm range. ^1H spectra (5-7 ppm range) of VA fully loaded with c) enflurane, d) isoflurane and e) halothane. The signals of halogenated ethers confined in the nanochannels and outside the pores are highlighted in orange and blue, respectively.

Nuclear magnetic resonance experiments performed after the guest adsorption from the vapor phase established the basis of a deep analysis, developed to understand the dipeptides' potentialities as anesthetic agents' vessels. First of all, evacuated crystals of VA, AI and VV underwent adsorption measurements, as they were put in presence of the halogenated guests for 4 hours. Then, few rotors were filled with dipeptides/guests adducts and solid-state NMR measurements were performed at different temperatures and spinning speeds and for diverse nuclei, ^1H , ^{13}C and ^{19}F . NMR experiment of the evacuated dipeptide crystals were also performed, to have a term of comparison between the pre- and post-adsorption situations. The case of ^1H solid-state NMR is straightforward. All the 600 MHz ^1H measurements were realized applying a 30 kHz spinning speed and the signals of the anesthetic molecules (enflurane, isoflurane and halothane) appeared in a range between 5 and 7 ppm. Due to its lower adsorption, desflurane was not employed in this spectroscopic analysis; diethyl ether, despite its good affinity with the dipeptides, was excluded too, because it has no medical application nowadays. All the anesthetic peaks partially overlap one of dipeptides' central signals, but they are easily distinguishable from the matrixes ones. Fast magic angle spinning ^1H NMR spectra provided direct evidence of the inclusion of the anesthetics in the crystalline channels of VA, AI and VV upon sorption from the gas phase. In Figure 12 the significative example of VA with enflurane, isoflurane and halothane is reported. Indeed, VA was let adsorbing the different anesthetic vapors and, in the case of enflurane, two situations were explored. In the first case, shown in Figure 12b, the VA crystals were overloaded with enflurane, and therefore in the NMR spectrum appear two different groups of signals: the peaks belonging to the anesthetic adsorbed inside the nanochannels and the peaks due to the molecules present on the surface of the porous matrix. When a porous material is completely filled, the guest in excess covers the surface and it is present at the liquid state. An interesting feature is the upfield shift ($\delta = -0.2$ ppm) of included halogenated ethers with respect to the pure compounds, owing to the magnetic susceptibility generated by the dipeptide environment⁴⁷. Therefore, the sample with an excess of enflurane in VA allowed us to distinguish the signals of free (in blue in Figure 12) and included enflurane (in orange in Figure 12). A comparison between anesthetics included in the nanochannels and anesthetics adsorbed just on the surface of a non-porous material, the tricalcium aluminate celite, enhance the different chemical shift range of the two groups of signals. A good match between the chemical shifts of the guests adsorbed on celite and in excess on VA demonstrate the correspondence between the two groups of signals (see Table 1).

Enflurane	-CHF ₂ (ppm)			-CHF ₂ (ppm)	
<i>Liquid in celite</i>	6,64	6,53	6,41	6,00	5,92
<i>Liquid in excess on VA surface</i>	6,64	6,53	6,41	6,00	5,92
Adsorbed in excess inside VA	---	6,29	6,18	5,82	5,75
Adsorbed in VA	6,39	6,28	6,17	5,81	5,74

Table 1. Chemical shifts of enflurane adsorbed on celite and on VA.

Moreover, the signals of the guest halogenated molecules have a linewidth wider than that of free molecules, owing to stronger ^1H homonuclear coupling, indicating a motion restriction. A quantitative analysis of the amount of included anesthetics with respect to the dipeptide hosts allowed us to measure the maximum loading of the channels.

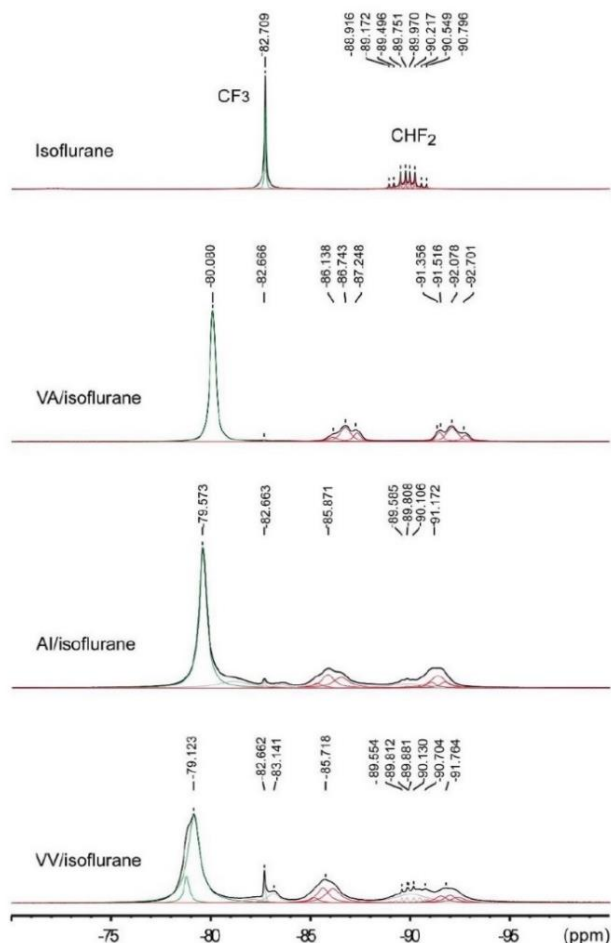


Figure 13. ^{19}F SPE MAS NMR spectra of pure isoflurane (298 K) and isoflurane in dipeptides (249 K).

The target of this second analysis was the comparison between the maximum loading values coming from the adsorption isotherms and the corresponding amounts evaluated from ^1H NMR experiments. To calculate the host/guest molar ratio from the NMR data, the intensities of the simulated peaks (shown in colors under the spectra in Figure 12 and in Appendix C) were divided for the number of hydrogen atoms belonging respectively to the dipeptide and to the anesthetic molecule. Dividing the value obtained from the guest peaks by the number obtained from the matrix, the molar ratio was achieved, which indicated the loading level of the porous crystals. Enflurane, isoflurane and halothane in VA were found to be 0.19, 0.16 and 0.19 mol mol $^{-1}$, respectively, in agreement with the amount measured from adsorption isotherms at 273K (0.18, 0.16 and 0.19 mol mol $^{-1}$). The adsorption values at 273 K were preferred to the 298 K ones because the NMR experiments were performed at 250 K. The ^1H NMR spectra of enflurane, isoflurane and halothane inside AI and VV, together with the spectra of the empty matrixes, are listed in Appendix C. $^{13}\text{C}\{^{19}\text{F}\}$, $^{13}\text{C}\{^1\text{H}\}$ CP MAS and ^{19}F solid-state NMR

spectra at low temperature of the adducts dipeptides/anesthetics were also performed to expand the comprehension of the host-guest interactions. Concerning the carbon spectra, both decoupled from proton or from fluorine, the guest signals appear with low peak intensities and hardly recognizable from the signal/noise ratio. For the same reason, it was difficult to identify the different guest's multiplets and to provide the correct assignment to the various peaks. Therefore, the carbon spectra needed a deeper investigation through the simulation analyses, as explained in the next paragraph. The fluorine NMR spectra, instead, supplied interesting considerations on how the anesthetic molecules arrange inside the dipeptide nanochannels. Looking at Figure 13, the ^{19}F NMR series of isoflurane, at the liquid state on celite (top) and adsorbed in the three dipeptides (bottom), is illustrated. We can first observe that the $-\text{CHF}_2$ group, present as a multiplet in the liquid state, splits in two different triplets when the anesthetic is adsorbed inside a porous matrix. Moreover, all the peaks shift to lower chemical shifts when the guest is included in the crystalline frameworks. There is another important feature we can notice: in all the adsorbed guest's spectra are still present low amounts of isoflurane at the liquid state, as clearly identified by the $-\text{CF}_3$ singlet at -82 ppm in all the three cases, and by the $-\text{CHF}_2$ signals between -89 and -90 ppm for AI and VV. This interesting trend is reasonable, since the isoflurane loading performed was the same for all the dipeptides: the smaller is the room available to host the anesthetic guests, the higher is the amount of guest in excess on the surface. In this way, we understood the reason why the VV/isoflurane spectrum presents more intense peaks of the free molecule compared to the other two matrixes, since VV has the smallest pore diameter. Other innovative characteristics were derived from the comparison between solid-state NMR and simulations, as highlighted in the next paragraph.

3.8 Conformational analysis

As one of the still unsolved mystery of general anesthesia is the way anesthetics structure alter proteins functions, understanding how these drugs rearrange in confined spaces can represent a promising starting point. Furthermore, a conformational analysis of anesthetics in nanochannels has never been conducted before. As promising guests, we chose the two isostructural isomers enflurane and isoflurane. These two compounds, known for their active role as inhalation anesthetics, can represent ideal probes to investigate the conformation-properties relationship in a confined space, since they are formed by the same atoms disposed in a different spatial arrangement. The first theoretical study allowed us to establish the most stable conformers of isoflurane and enflurane, using the hybrid density functional method B3LYP/6-311++G(2df,p). For isoflurane we found two main conformational minima, while for enflurane four principal minima and other three with slightly higher energy, for a total of seven conformations. In Appendix C are reported all the conformational minima found. About isoflurane, the dihedral angles θ_1 and θ_2 (C-C-O-C and $\text{F}_1\text{-C-O-C}$, respectively) were investigated and it was observed the stability of two conformational minima in the energy map, with values as close as $\Delta = 0.5 \text{ kcal mol}^{-1}$. In conformer I, the F-C-O-C dihedral angles for F_1 and F_2 are -63° and 58° (i.e. both in *gauche* conformation); on the contrary, in conformer II the $\text{F}_1\text{-C-O-C}$ and $\text{F}_2\text{-C-O-C}$ dihedral angles are 177° and -62° , respectively (i.e. F_1 in *trans* and F_2 in *gauche* conformations)⁴⁸. Once the two most stable conformers were evaluated, the simulation of their NMR spectra followed, aiming to correlate the experimental data with

the calculations, using the B3LYP/6-311G++(2df,p) GIAO method. As mentioned above, ^{19}F MAS NMR spectra of isoflurane in the all the dipeptides show a dramatic change with respect to the spectra in the liquid state. Indeed, the ^{19}F NMR spectra of isoflurane confined in VA showed two distinct triplets separated by about 5.3 ppm for the two fluorine nuclei of the CHF_2 group, in contrast to a single multiplet recorded for pure isoflurane in the bulk wherein fast exchange among conformers occurs. Such large separation must be ascribed to the conformational arrangement of the two fluorine atoms and the γ -*gauche* effect that produces an upfield shift of 5 ppm when the observed nucleus changes from a *trans* to a *gauche* conformation⁴⁹. The experimental spectrum clearly indicates that the conformer II (with the torsional angle θ_2 setting F_1 in *trans* and F_2 in *gauche* conformation) provides the only feasible arrangement of isoflurane confined in the narrow dipeptide channels: in fact, the behavior of included isoflurane is common to all the observed dipeptide crystals, such as AI and VV. Indeed, the lateral steric encumbrance is reduced in conformer II because at least one of the two fluorine atoms is set in the more elongated *trans* arrangement, whereas in conformer I both fluorines protrude laterally in *gauche* arrangement. Conformer II also displayed a θ_1 torsional angle close to a *trans* arrangement, setting the main chain in the most elongated conformation, which is reasonable for a molecule confined in a channel. ^{13}C CP MAS spectra decoupled from ^1H or ^{19}F are in agreement with the stretched conformation preferred for the steric requirements imposed by the crystalline channels. As shown in Figure 14, the simulated spectra of both isoflurane conformers present the same signal multiplicity, well reproducing the experimental ones. However, in the carbon spectra the chemical shifts of the two minima are not influenced by the conformational structure and the simulations are not diagnostic of the conformation of the adsorbed isoflurane.

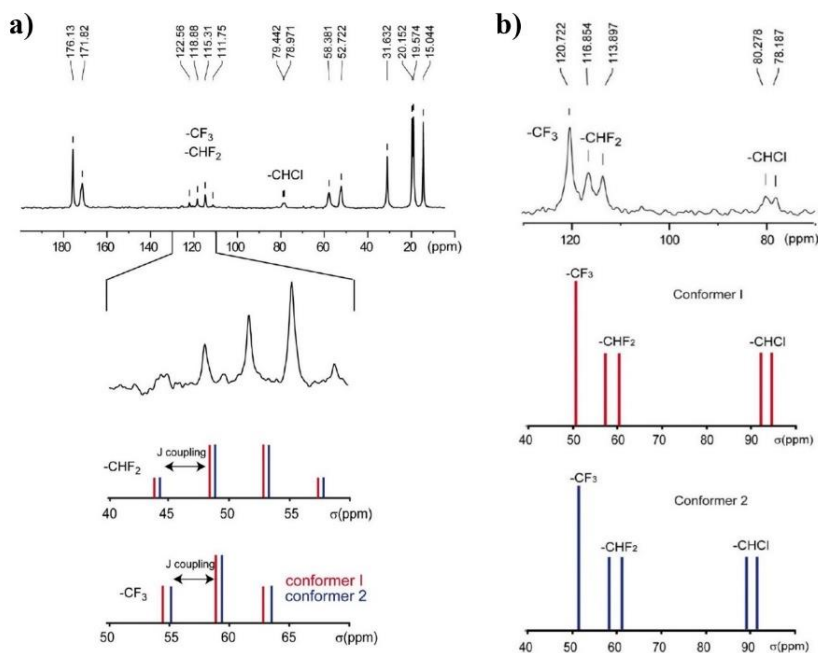


Figure 14. Isoflurane ^{13}C NMR spectra: a) $^{13}\text{C}\{^1\text{H}\}$ CP MAS NMR spectrum of isoflurane in VA at 249 K (ss= 8 kHz, ct= 5 ms) (above), predicted ^{13}C chemical shifts of the two conformers (below); b) zoom of $^{13}\text{C}\{^{19}\text{F}\}$ CP MAS NMR spectrum of isoflurane in VA at 249 K (ss= 8 kHz, ct= 5 ms) (above), predicted ^{13}C chemical shifts of the two conformers I and II (below).

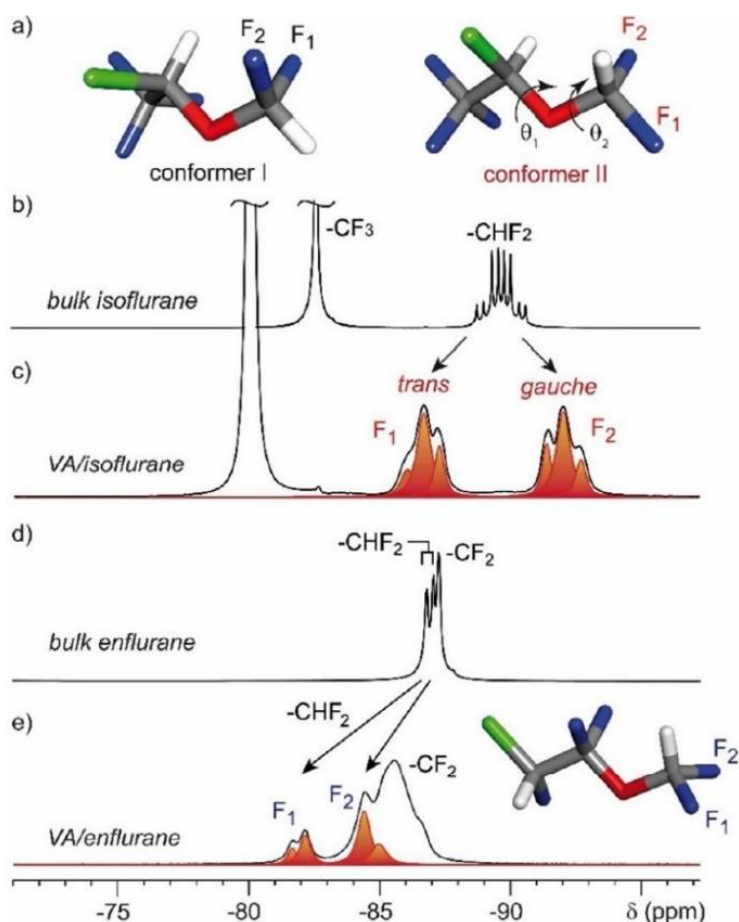


Figure 15. Conformational analysis. In a) the two minima of isoflurane: conformer I and II with C-C-O-C of 139° and of 166°, respectively. ^{19}F MAS NMR spectra in a) isoflurane on celite, b) isoflurane in VA, d) enflurane on celite, e) enflurane in VA.

With the help of the conformation analysis we were able to interpret the complicated guest's signal multiplicity of the solid-state ^{13}C NMR, developing a deeper knowledge of the structural arrangements inside the porous crystalline dipeptides. It was also highlighted that ^{19}F NMR is a sensitive tool for understanding the relationship between halogenated guests inside 1D nanochannels. In the case of enflurane, a different behavior is observed for the CHF_2 group and this feature strongly influences our considerations on its conformational array in a porous material. Actually, the two fluorine nuclei resonate downfield with respect to those of the structural isomer isoflurane. This is due to the conformation of the two fluorine atoms which are set at F-C-O-C dihedral angles of -105° and 135° and that thus do not undergo γ -gauche effect when enflurane is included in the VA channels. Therefore, the simulated NMR spectra for all the seven enflurane conformational minima present the same signal multiplicity of the $^{13}\text{C}\{^1\text{H}\}$ and $^{13}\text{C}\{^{19}\text{F}\}$ SPE MAS NMR experimental spectra in VA (reported in Appendix C). We were not able to determine the principal conformation through which enflurane is included in VA and we concluded that the real conformer is a medium of all the possible minima. In Figure 15 are displayed the conformational minima of isoflurane and the series of ^{19}F NMR spectra involved in the spectroscopic comparison with the calculations. The Gran Canonical Monte Carlo simulations of enflurane and isoflurane isotherms in VA show that the energetically stable conformers occupy the channels with a

maximum loading corresponding to that of the experimental isotherms and the guests are not periodically distributed along the channels (Figure 16).

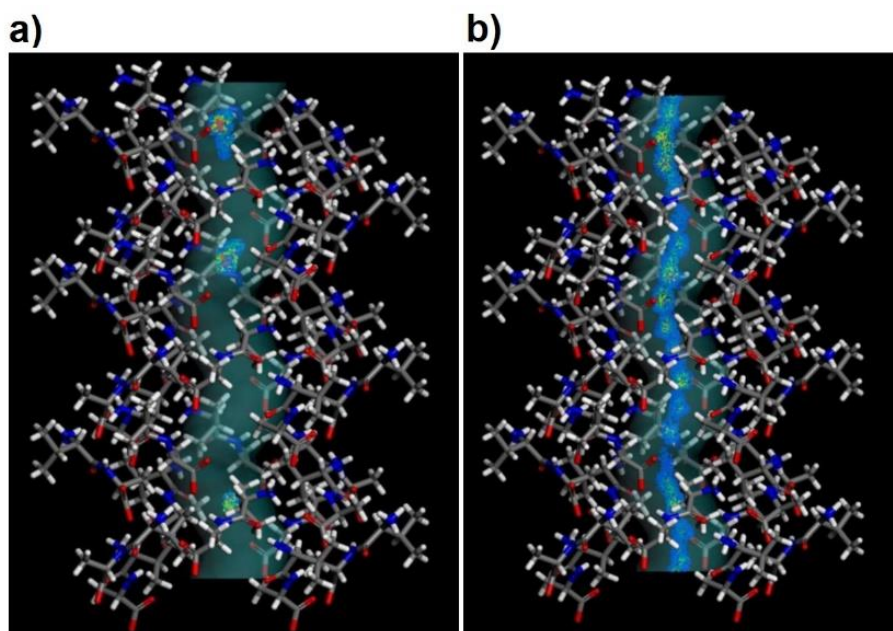


Figure 16. Crystal structure of VA, as viewed perpendicular to the channel axis, showing the mass centers of: a) *S*-isoflurane as determined by the GCMC simulation of isoflurane adsorption at 298 K and at a pressure of 150 torr; b) enflurane in the same temperature and pressure conditions.

3.9 Conclusions

In conclusion, dipeptide crystals, with their chiral ultra-micropores, offer suitable room for hosting anesthetic molecules and tuning their volatility. The diversity in the size and shape of the space available for the guests in the numerous dipeptide structures enabled the selection of the most appropriate dipeptide crystals for specific guests and showed the remarkable selectivity. For the first time, nanoporous materials of biological origin were tested for the adsorption of volatile drugs commonly used in general anesthesia. The adsorption capacities of the dipeptide crystals were probed through isotherms performed at 273 and 298K until the vapor pressure was reached. The guests included in the dipeptide crystals were detected by ^{13}C , ^{19}F and fast ^1H MAS NMR spectroscopy, which provided a detailed analysis of the arrangement of the guest molecules in the cavities and the amount of loaded anesthetics, in agreement with the adsorption isotherms. Despite their biological nature, these systems retain the crystallinity upon the vapors adsorption, as highlighted by PXRD analysis. A conformational study was also performed to understand the arrangement of the anesthetic molecules confined inside the dipeptide channels. This investigation may shed light on the way volatile anesthetics adapt to variable-size sub-nanometric channels, miming biological receptors. Moreover, the biodegradability and biocompatibility of porous dipeptide materials encourages their use in biomedical applications.

3.10 References

1. S. Kitagawa, *Angew. Chem. Int. Ed.*, **2015**, 54, 10686.
- 2 (a) D. W. Breck, *Zeolite Molecular Sieves. Structure, Chemistry and Use*, Wiley, New York, 1974, 593; (b) H-C. Zhou, J. R. Long and O. M. Yaghi, *Chem. Rev.*, **2012**, 112, 673; (c) S. Das, P. Heasman, T. Ben and S. Qiu, *Chem. Rev.*, **2017**, 117, 1515; (d) Z. Zhang and M. J. Zaworotko, *Chem. Soc. Rev.*, **2014**, 43, 5444; (e) N. Huang, P. Wang and D. Jiang, *Nature Rev. Mater.*, **2016**, 1, 1; (f) P. J. Waller, F. Gandara, O. M. Yaghi, *Acc. Chem. Res.*, **2015**, 48, 3053.
- 3 (a) H. Wang, B. Li, H. Wu, T.-L. Hu, Z. Yao, W. Zhou, S. Xiang and B. Chen, *J. Am. Chem. Soc.*, **2015**, 137, 9963; (b) S. A. Dalrymple and G. K. H. Shimizu, *J. Am. Chem. Soc.*, **2007**, 129, 12114; (c) N. B. Mckewon, *J. Mater. Chem.* **2010**, 20, 10588; (d) P. Sozzani, S. Bracco, A. Comotti, L. Ferretti and R. Simonutti, *Angew. Chem. Int. Ed.*, **2005**, 44, 1816; (e) M. Baroncini, S. d'Agostino, G. Bergamini, P. Ceroni, A. Comotti, P. Sozzani, I. Bassanetti, F. Grepioni, T. M. Hernandez, S. Silvi, M. Venturi and A. Credi, *Nature Chem.*, **2015**, 7, 634; (f) A. Comotti, S. Bracco, A. Yamamoto, M. Beretta, T. Hirukawa, N. Tohnai; M. Miyata and P. Sozzani, *J. Am. Chem. Soc.*, **2014**, 136, 618; (g) A. Pulido, L. Chen, T. Kaczorowski, D. Holden, M. A. Little, S. Y. Chong, B. J. Slater, D. P. McMahon, B. Bonillo, C. J. Stackhouse, A. Stephenson, C. M. Kane, R. Clowes, T. Hasell, A. I. Cooper, and G. M. Day, *Nature*, **2017**, 543, 657; (h) W. Yang, A. Greenaway, X. Lin, R. Matsuda, A. J. Blake, C. Wilson, W. Lewis, P. Hubberstey, S. Kitagawa, N. R. Champness and M. Schroder, *J. Am. Chem. Soc.*, **2010**, 132, 14457; (i) M. Mastalerz and I. M. Oppel, *Angew. Chem. Int. Ed.*, **2012**, 51, 5252; (l) R. S. Patil, D. Banerjee, C. Zhang, P. K. Thallapally and J. L. Atwood, *Angew. Chem. Int. Ed.*, **2016**, 55, 4523; (m) V. N. Yadav, A. Comotti, P. Sozzani, S. Bracco, T. Bonge-Hansen, M. Hennum, and C.-H. Gorbitz, *Angew. Chem. Int. Ed.*, **2015**, 54, 15684; (n) Y. Liu, C. Hu, A. Comotti and M. D. Ward, *Science*, **2011**, 333, 436; (o) I. Bassanetti, F. Mezzadri, A. Comotti, P. Sozzani, M. Gennari, G. Calestani and L. Marchio, *J. Am. Chem. Soc.*, **2012**, 134, 9142.
- 4 (a) C. H. Gorbitz, E. Gundensen, *Acta Crystallogr., Sect. C: Cryst. Struc. Commun.*, **1996**, 52, 1764; (b) A. Comotti, A. Fraccarollo, S. Bracco, M. Beretta, G. Distefano, M. Cossi, L. Marchese, C. Riccardi, P. Sozzani, *Cryst. Eng. Comm.*, **2013**, 15, 1503; (c) D. V. Soldatov, I. L. Moudrakoski and J. A. Ripmeester, *J. Am. Chem. Soc.*, **2006**, 128, 6737.
- 5 (a) R. V. Alfonso, J. Durao, A. Mendes, A. M. Damas and L. Gales, *Angew. Chem. Int. Ed.*, **2010**, 49, 3034; (b) S. Lim, H. Kim, N. Selvapalam, K.-J. Kim, S. J. Cho, G. Seo and K. Kim, *Angew. Chem. Int. Ed.*, **2008**, 47, 3352; (c) V. N. Yadav, A. Comotti, P. Sozzani, S. Bracco, T. Bonge-Hansen, M. Hennum, C.H. Gorbitz, *Angew. Chem. Int. Ed.*, **2015**, 54, 15684.
- 6 A. Comotti, S. Bracco, G. Distefano, P. Sozzani, *Chem. Comm.*, **2009**, 284.
- 7 G. Distefano, A. Comotti, S. Bracco, M. Beretta and P. Sozzani, *Angew. Chem. Int. Ed.*, **2012**, 51, 9258.
- 8 S. Bracco, D. Asnaghi, M. Negroni, P. Sozzani, A. Comotti, *Chem. Comm.*, **2017** (accepted).
- 9 J. F. Hendrick, E. I. Eger, J. M. Sonner and S. L. Shafer, *Anesth. Analg.*, **2008**, 107, 494.
- 10 (a) P. S. Garcia, S. E. Kolesky and A. Jenkins, *Curr. Neuropharmacol.*, **2010**, 8, 2; (b) P. S. Miller and A. Radu Aricescu, *Nature*, **2014**, 512, 270.
- 11 (a) S. M. Ryan and N. J. Claus, *Anesth. Analg.*, **2010**, 111, 92; (b) S. Y. Jeffrey and J. White, *Anesth Prog*, **2012**, 59, 154; (c) J. Sherman, C. Le, V. Lamers and M. Eckelman, *Anesth. Analg.*, **2012**, 114, 108; (d) M. P. Sulbaek Andersen, S. P. Sander, O. J. Nielsen, D. S. Wagner, T. J. Sanford Jr and T. J. Wallington, *Br. J Anaesth.*, **2010**, 6, 760.
- 12 (a) B. F. Abrahams, A. D. Dharma, P. S. Donnelly, T. A. Hudson, C. J. Kepert, R. Robson, P. D. Southon and K. F. White, *Chem. Eur. J.*, **2017**, 23, 7871; (b) T.H. Chen, W. Kaveevivitchai, A. J. Jacobson and O. S. Miljanic, *Chem. Comm.* **2015**, 51, 14096; (c) N. Gargiulo, A. Peluso, A. P. Aprea, Y. Hua, D. Filipovi, D. Caputo and M. Eic, *RSC Adv.*, **2014**, 4, 49478.
- 13 M. Vallet-Regi, F. Balas and D. Arcos, *Angew. Chem. Int. Ed.*, **2007**, 46, 7548.
- 14 C. H. Gorbitz, *Chem. Eur. J.*, **2007**, 13, 1022.

- 15** C. H. Gcrbitz, M. C. Etter, *Int. J. Pept. Protein Res.*, **1992**, 39, 93.
- 16** (a) D. S. Eggleston, *Acta Crystallogr. Sect. C*, **1984**, 40, 1250; (b) C. H. Gcrbitz, *Acta Crystallogr. Sect. C*, **1999**, 55, 2171.
- 17** R. J. Fletterick, C. Tsai, R. E. Hughes, *J. Phys. Chem.* 1971, 75, 918.
- 18** C. H. Gcrbitz, *New J. Chem.*, **2003**, 27, 1789.
- 19** Y. Ishizawa, *Anesth. Analg.*, **2011**, 112, 213.
- 20** T. G. Weiser, A. B. Haynes, G. Molina, S. R. Lipsitz, M. M. Esquivel, T. Uribe-Leitz, R. Fu, T. Azad, T. E. Chao, W. R. Berry, *The Lancet*, **2015**, 385, S11.
- 21** (a) F. Maggs, M. Smith, *Anaesthesia*, **1976**, 31, 30; (b) J. C. Smith, B. Bolon, *Contemp. Top. Lab. Anim. Sci.*, **2003**, 42, 10; (c) N. Birgenheier, R. Stoker, D. Westenskow, J. Orr, *Anesth. Analg.*, **2011**, 112, 1363; (d) D. J. Doyle, R. Byrick, D. Filipovic, F. Cashin, *Can. J. Anaesthesia*, **2002**, 49, 799; (e) D. Saha, Z. Bao, F. Jia, S. Deng, *Environ. Sci. Technol.*, **2010**, 44, 1820; (f) D. Saha, S. Deng, *J. Chem. Eng. Data*, **2010**, 55, 3312; (g) M. Guillemot, B. Castel, *Ind & Eng. Chem. Res.*, **2015**, 54, 7760; *Eng. Chem. Res.*, **2015**, 54, 7760;
- 22** (a) N. Gargiulo, F. Pepe and D. Caputo, *J. Nanosci. Nanotechnol.*, **2014**, 14, 1811; (b) L. Perhag, P. Reinstrup, R. Thomasson and O. Werner, *Br. J. Anaesth.*, **2000**, 85, 482; (c) D. J. Doyle, R. Byrick, D. Filipovic and F. Cashin, *Can. J. Anaesth.*, **2002**, 49, 799; (d) W. K. Grodin, M. A. Epstein and R. A. Epstein, *Anesthesiology*, **1985**, 62, 60; (e) B. M. Kim and S. Sircar, *Anesthesiology*, **1977**, 46, 159.
- 23** Patrick Graham L., *Introduzione alla chimica farmaceutica*, **2010**, ed. 2a Edisis.
- 24** J. F. Hendrickx, E. I. Eger, J. M. Sonner and S. L. Shafer, *Anesth Analg.*, **2008**, 107 (2): 494.
- 25** J. A. Campagna, K. W. Miller and S. A. Forman, *N Engl J Med*, **2003**, 348, 2110.
- 26** L. T. Kohn, J. M. Corrigan, M. S. Donaldson, eds., *To err is human: building a safer health system*, Washington, D.C., National Academy Press, **2000**.
- 27** S. Vemparala, C. Domene, M. Klein, *Accounts of chemical research*, **2012**, 43, 103.
- 28** E. S. Niedermeyer and F. H. Lopes, *Electroencephalography: Basic Principles, Clinical Applications, and Related Fields*, Lippincott Williams & Wilkins, **2005**.
- 29** V. Law, C. Knox, Y. Djoumbou, T. Jewison, A. C. Guo, Y. Liu, A. Maciejewski, D. Arndt, M. Wilson, V. Neveu, A. Tang, G. Gabriel, C. Ly, S. Adamjee, Z. T. Dame, B. Han, Y. Zhou and D. S. Wishart, *DrugBank 4.0: shedding new light on drug metabolism.*, *Nucleic Acids Res.*, **2014**, 42(1): D1091-7.24203711.
- 30** “WHO Model List of Essential Medicines (19th List)”, World Health Organization, **2015**.
- 31** “WHO Model Formulary 2008”, World Health Organization, **2009**.
- 32** E. I. Eger II, L. J. Saidman and B. Brandstater, *Anesthesiology*, **1965**, 26, 756.
- 33** (a) E. Overton., *Studien über die Narkose Zugleich ein Beitrag zur Allgemeinen Pharmakologie.*, Jena, Germany, Verlag von Gustav Fisher, **1901**; (b) H. Meyer, *Arch Exp Pathol Pharmacol*, **1899**, 42, 109.
- 34** N. P. Franks and W. R. Lieb, *Nature*, **1982**, 300, 487.
- 35** J. F. Antognini and E. Carstens, *Br J Anaesth*, **2002**, 89, 156.

- 36 (a) A. Angel, *Br J Anaesth*, **1993**, 71, 148; (b) J. G. Collins, J.J. Kendig and P. Mason, *Trends Neurosci*, **1995**, 18, 549.
- 37 W. Heinke and C. Schwarzbauer, *Br J Anaesth*, **2002**, 89, 112.
- 38 (a) K. W. Miller, *Br J Anaesth*, **2002**, 89, 17; (b) N. P. Franks, A. Jenkins, E. Conti, W. R. Lieb and P. Brick, *Biophys J*, **1998**, 75, 2205; (c) R. G. Eckenhoff, *Mol Interventions*, **2001**, 1, 258.
- 39 (a) N. P. Franks and W. R. Lieb, *Toxicol Lett*, **1998**, 100-101, 1; *Nature*, **1994**, 367, 607; (b) S. Mennerick, V. Jevtovic-Todorovic, S. M. Todorovic, W. Shen, J. W. Olney and C. F. Zorumski, *J Neurosci*, **1998**, 18, 9716; (c) T. Narahashi, G. L. Aistrup, J. M. Lindstrom et al., *Toxicol Lett*, **1998**, 100-101, 185.
- 40 (a) J. J. Kendig, *Br J Anaesth*, **2002**, 89, 91; (b) S. Daniels and R. J. Roberts, *Toxicol Lett*, **1998**, 100-101, 71.
- 41 G. Cheng and J. J. Kendig, *Anesthesiology*, **2000**, 93, 1075.
- 42 (a) J. S. Johansson, B. R. Gibney, F. Rabanal, K. S. Reddy and P.L. Dutton, *Biochemistry*, **1998**, 37(5), 1421; (b) T. Cui, V. Bondarenko, D. Ma, C. Canlas, N. R. Brandon, J. S. Johansson, Y. Xu and P. Tang, *Biophys. J.*, **2008**, 94 (11): 4464; (c) D. Ma, N. R. Brandon, T. Cui, V. Bondarenko, C. Canlas, J. S. Johansson, P. Tang and Y. Xu, *Biophys. J.*, **2008**, 94 (11), 4454; (d) R. Liu, P. J. Loll and R. G. Eckenhoff, *FASEB J.*, **2005**, 19 (6), 567.
- 43 P. Tang and Y. Xu, *Proc. Natl. Acad. Sci. U.S.A.*, **2002**, 99 (25), 16035.
- 44 C. G. Canlas, T. Cui, L. Li, Y. Xu and P. Tang, *J. Phys. Chem. B.*, **2008**, 112 (45), 14312.
- 45 S. J. Mihic, Q. Ye, M. J. Wick, V. V. Koltchine, M. D. Krasowski, S. E. Finn, M. P. Mascia, C. F. Valenzuela, K. K. Hanson, E. P. Greenblatt, R. A. Harris and N. L. Harrison, *Nature*, **1997**, 389 (6649), 385.
- 46 N. Gargiulo, A. Peluso, P. Aprea, Y. Hua, D. Filipovi, D. Caputo and M. Eic, *RSC Adv.*, **2014**, 4, 49478.
- 47 (a) S. Brown, *Prog. Nucl. Magn. Reson. Spectroscop.*, **2007**, 50, 199; (b) S. Bracco, A. Comotti, P. Valsesia, M. Beretta and P. Sozzani, *Cryst. Eng. Commun.*, **2010**, 12, 2318; (c) S. Bracco, A. Comotti, L. Ferretti and P. Sozzani, *J. Am. Chem. Soc.*, **2011**, 133, 8982; (d) P.A. Williams, C.E. Hughes, J. Martin, E. Courvoisier, A.B.M. Buanz, S. Gaisford and K.D.M. Harris, *J Phys. Chem. C*, **2016**, 120, 9385.
- 48 (a) A. Lesarri, A. Vega-Toribio, R. D. Suenram, D. J. Brugh, D. Nori-Shargh, J. E. Boggsd and J-U. Grabowe, *Phys. Chem. Chem. Phys.*, **2011**, 13, 6610; (b) A. Pfeiffer, H-G. Mack and H. Oberhammer, *J. Am. Chem. Soc.*, **1998**, 120, 6384.
- 49 D. G. Gorenstein, *J. Am. Chem. Soc.*, **1977**, 99, 2254.

Chapter 4

Metal-organic frameworks: gas adsorption and enantioselectivity properties

In the last decades, porous materials have grabbed considerable attention because of their applications in gas and vapor storage, in separation of industrial gas mixtures, in catalysis, but also for their potentialities in nanomedicine^{1,2}. In this field, two main routes have been followed: the first is based on the use of biocompatible macromolecules or polymers^{3,4}, while the second is supported by inorganic hosts, such as zeolites^{5,6} and mesoporous silicates⁷. The first solution offers a great variety of drugs which can be encapsulated, but the lack of a defined porosity makes the controlled release quite difficult. In the second case, drugs are grafted on the pore walls, reducing in this way the inner guest-loading capacity of the inorganic matrices⁸. Metal-organic frameworks (MOFs), formed by the self-assembly between organic linkers and metallic nodes, can represent a new and suitable platform for improving the biomedical solutions of the porous materials. The mostly organic structure, combined with a regular porosity, can provide both a good drug loading and a controlled release. Another important feature of metal-organic frameworks consists in the possibility to articulate the structures with desirable pore shapes and functionalizations, following the molecular tectonics approach^{9,10}. This peculiarity takes this class of materials a step forward inside the nanomedicine development, making them innovative tools for the separation of racemic drug precursors. Actually, a wide range of pharmaceuticals and chemicals come from racemic mixtures, but the two enantiomers often show different biological responses^{11,12}. A chiral molecule (from the Greek word *χείρ*, “hand”) has a nonsuperimposable mirror image, called enantiomer. Due to their identical physical and chemical characteristics, enantiomers represent an ongoing challenge to be separated. According to the three-point rule¹³, chiral recognition requires at least three interactions (two attractive and one repulsive) between the selector and the analyte. One of these interactions must be stereoselective to enable chiral separation. Nowadays mature techniques, such as high performance liquid chromatography, capillary electrophoresis and electrochromatography, gas chromatography, supercritical fluid chromatography, simulated moving bed chromatography and other miscellaneous technologies (high-speed counter-current chromatography, thin layer chromatography)¹⁴ are successfully employed. However, the use of chiral separation stationary phases is expensive and the critical necessity of cheaper chiral selectors prompted the role of porous 3D networks as promising enantioselective materials, thanks to their low cost, high surface areas, easy scale-up and chemical

versatility. Moreover, the presence of multiple chiral recognition sites inside the porous structure allows to exert the necessary stereocontrol on the analytes. Among porous materials, homo-chiral porous coordination polymers (PCPs) and metal-organic frameworks represent an important sub-class, able to offer tailored chiral cavities and high density of active sites. Examples of chiral extended architectures of the metal-organic frameworks or PCPs have been reported¹⁵. Chiral metal-organic frameworks are therefore of particular interest for enantiomeric discrimination¹⁶. In this chapter, six new homo-chiral microporous metal-organic frameworks are presented. Their gas sorption properties, with respect to gases important for energetic and environmental reasons, such as methane and carbon dioxide, have been firstly investigated. Once proved the permanent porosity, we studied the enantioselective performances towards different organic molecules of biomedical interest, such as the proteogenic amino-acid tryptophan¹⁷ and racemic mixtures of small molecules.

4.1 Homo-chiral metal-organic frameworks: synthetic procedures

Herein I report briefly on the preparation of the six metal-organic networks used, **1**-Zn, **3**-Zn, **1**-Cu, **3**-Cu, **1**-Cu(OH) and **3**-Cu(OH), synthesized by the group of prof. Mir Wais Hosseini of Strasbourg university. The design is based on the use of enantiomerically pure organic linkers bearing two homo-chiral side chains and four carboxylate coordinating groups. Therefore, here we followed the first route for the synthesis of homo-chiral open tridimensional frameworks, as cited in Chapter 1, which implies the use of a rigid homo-chiral organic ligand as linkers. Their combinations with Zn (II) or Cu(II) lead to the formation of porous crystals displaying channels lined with homo-chiral alkyl or hydroxyl moieties. The choice of Zn(II) and Cu(II) salts resulted natural, since they are able to form paddle-wheel nodes, ideal for the construction of porous tridimensional networks. The possibility of having mobile, chiral fragments, lined inside the cavities, prompted us to attach them to the central phenyl ring of the organic ligand. Consequently, the idea was to change the groups bonded to the stereogenic carbons, in order to modify the steric encumbrance inside the channels and to differentiate the possible intermolecular interactions that can be established between the chiral fragments and the guest molecules. All the six MOFs are different in the metal node or in the chiral chains attached to the same organic linker. Tectons of **1**-Zn and **1**-Cu differ from **3**-Zn and **3**-Cu in both connectivity of the alkyl fragment bearing the stereocenter (C*HMeEt for **1** and C*(CH₂)MeEt for **3**) and in their handedness ((*R,R*) enantiomer for the **1** compounds and (*S,S*) enantiomer for **3** compounds). On the other side, tectons of **1**-Cu(OH) and **3**-Cu(OH) present the same alkyl fragment connectivity, but differ in the handedness of the hydroxyl chiral centers ((*R,R*) enantiomer for the **1** compounds and (*S,S*) enantiomer for **3** compounds), as shown in Figure 1.

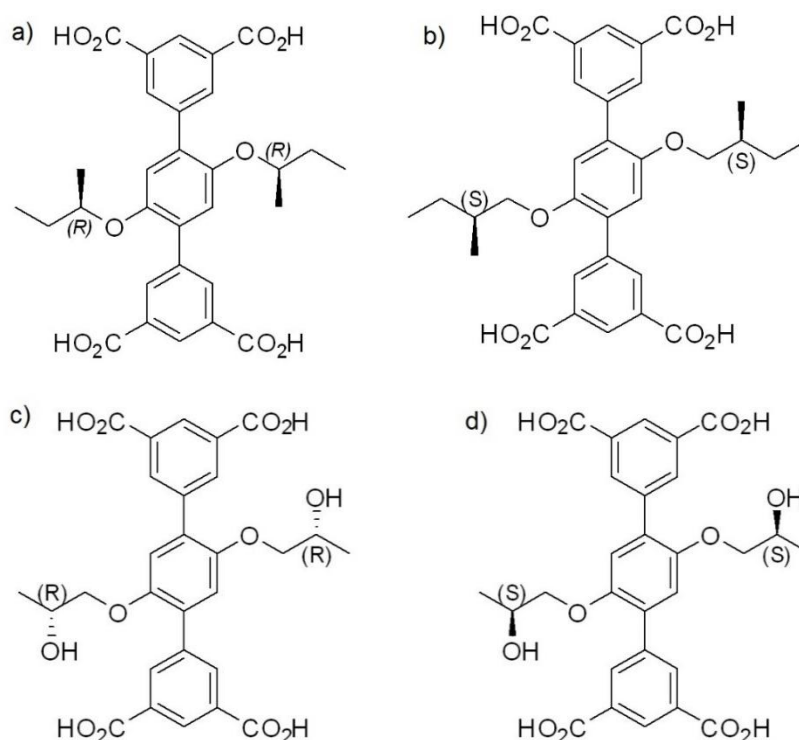
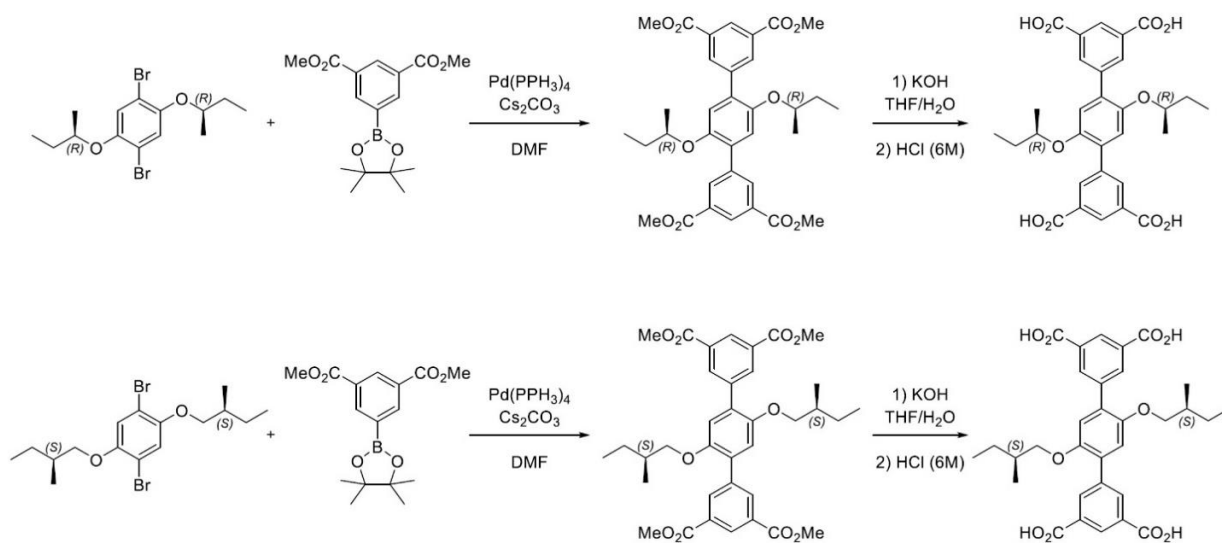


Figure 1. Chiral organic tectons of: a) **1-Zn** and **1-Cu**; b) **3-Zn** and **3-Cu**; c) **1-Cu(OH)**; d) **3-Cu(OH)**.

4.1.1 Synthesis of **1-Zn**, **3-Zn**, **1-Cu** and **3-Cu** tectons

For the first four MOFs, the synthesis of the organic linker started from 1,4-dibromo-2,5-di((*R*)-sec-butoxy)benzene and 1,4-dibromo-2,5-bis((*S*)-2-methylbutoxy)benzene, synthesized as described in the literature¹⁸. The coupling of the dibromo derivatives with 3,5-bis(methoxycarbonyl)phenylboronic acid pinacol ester afforded the respective tetraesters. The desired tectons were obtained upon saponification of the tetraesters. As metallic centers Zn (II) and Cu(II) cations were chosen owing to their propensity to form paddlewheel-type nodes with carboxylate moieties, as mentioned above. The reaction of the carboxylate tetraesters with $\text{Zn}(\text{NO}_3)_2$ in DMF at 100°C afforded single crystals of **1-Zn** and **3-Zn** after just 24 hours of heating. The SC-XRD analysis revealed the formation of tridimensional porous isostructural frameworks in both cases. The two 3D networks crystallize in a rhombohedral system, with $R\bar{3}$ space group; they are composed by the organic tetracarboxylate ligands, Zn (II) cations and solvent molecules (water and DMF). The DMF molecules are highly disordered inside the channels, therefore the “squeeze” computational procedure needed to be applied to refine the structures. Under similar conditions, combinations of the same tectons with $\text{Cu}(\text{NO}_3)_2$ in DMF at 85 °C and in the presence of HCl (1 drop, 3.7%) afforded, after 24 h, blue microcrystalline powders of **1-Cu** and **3-Cu**.

Scheme 1. Synthesis of **1-Zn**, **1-Cu**, **3-Zn** and **3-Cu** tectons.**1-Zn and 1-Cu**

$^1\text{H-NMR}$ (DMSO- d_6 , 400 MHz): δ (ppm) = 13.29 (br, 4H), 8.45 (t, 2H, $^4J = 1.6$ Hz), 8.37 (d, 4H, $^4J = 1.6$ Hz), 7.18 (s, 2H), 4.43 (m, 2H), 1.60-1.45 (m, 4H), 1.13 (d, 6H, $^3J = 6.0$ Hz), 0.82 (t, 6H, $^3J = 7.4$ Hz).

$^{13}\text{C-NMR}$ (DMSO- d_6 , 100 MHz): δ (ppm) = 166.7, 148.5, 138.5, 134.2, 131.2, 130.0, 128.6, 117.5, 75.5, 28.5, 18.7, 9.2

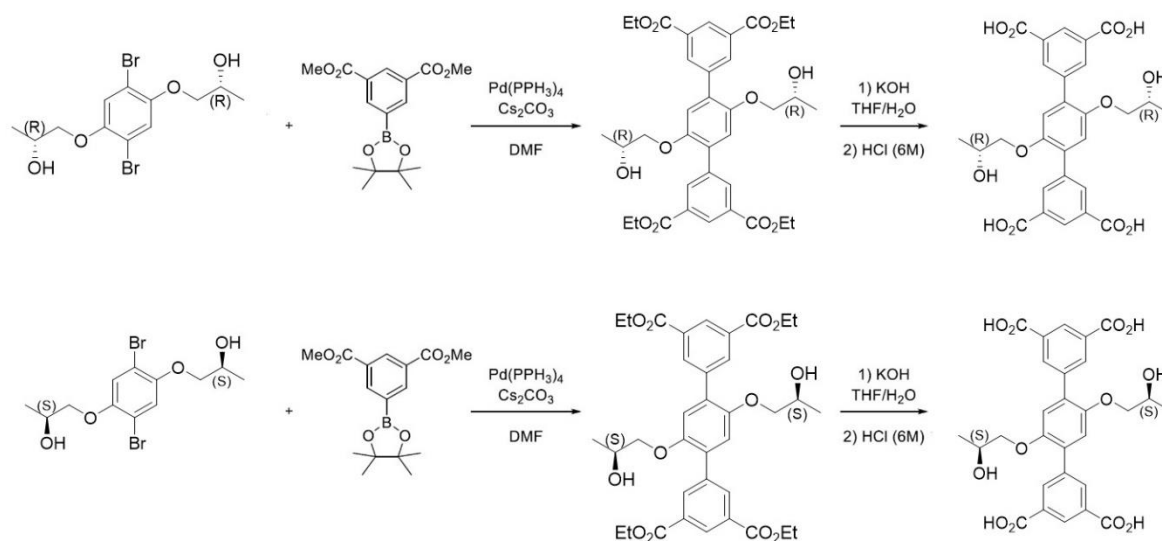
3-Zn and 3-Cu

$^1\text{H-NMR}$ (DMSO- d_6 , 400 MHz): δ (ppm) = 13.28 (br, 4H), 8.45 (t, 2H, $^4J = 1.6$ Hz), 8.38 (d, 4H, $^4J = 1.6$ Hz), 7.19 (d, 2H), 3.89 (dd, 2H, $^2J = 9.1$ Hz, $^3J = 5.7$ Hz), 3.84 (dd, 2H, $^2J = 9.1$ Hz, $^3J = 6.2$ Hz), 1.67 (m, 2H), 1.40 (m, 2H), 1.13 (m, 2H), 0.86 (d, 6H, $^3J = 6.8$ Hz), 0.79 (t, 6H, $^3J = 7.4$ Hz).

$^{13}\text{C-NMR}$ (DMSO- d_6 , 100 MHz): δ (ppm) = 166.6, 149.8, 138.3, 134.2, 131.1, 128.7, 128.5, 115.2, 73.5, 34.3, 25.5, 16.3, 11.1.

4.1.2 Synthesis of 1-Cu(OH) and 3-Cu(OH) tectons

Concerning the homo-chiral MOFs with the hydroxyl groups linked to the stereogenic carbons, the precursors (2*R*,2'*R*)-1,1'-[(2,5-bromo-1,4-phenylene)bis(oxy)]bis-2-propanol and (2*S*,2'*S*)-1,1'-[(2,5-bromo-1,4-phenylene)bis(oxy)]bis-2-propanol were synthesized as described in the literature¹⁸. As reported in the previous paragraph, the coupling of the dibromo compounds with 3,5-bis(ethylbenzoate) boronic ester gave the respective tetraesters. The final tectons were obtained upon saponification of the tetraesters (see Scheme 2). Only Cu(II) cations were chosen as metallic nodes, because the Zn-based frameworks were already found out to be not permanently porous. Zn(II) salts are able to provide single crystals of the 3D frameworks, since their crystallization pathway is quite slow and the structures can easily rearrange. Instead, Cu(II) cations rapidly crystallize with the organic ligands in DMF and therefore only microcrystalline powders were obtained in all cases.



Scheme 2. Synthesis of **1-Cu(OH)** and **3-Cu(OH)** tectons.

1-Cu(OH) and 3-Cu(OH)

$^1\text{H-NMR}$ (DMSO-d_6 , 400MHz): δ (ppm) = 1.08 (s, 6H), 3.77-3.98 (m, 6H), 4.70 (s, 2H), 7.19 (s, 2H), 8.38 (d, 4H, $^3J = 1.7$ Hz), 8.45 (t, 2H, $^3J = 1.7$ Hz), 13.29 (s, 4H).

$^{13}\text{C-NMR}$ (DMSO-d_6 , 100MHz): 20.9, 65.2, 75.1, 116.1, 129.5, 132.1, 134.9, 138.9, 150.4, 167.3.

$[\alpha]^{20}_{\text{D}} = +5.32^\circ$ ($c = 1.80$ in DMF).

4.2 Crystal structures

Single-crystal X-ray diffraction elucidated the solid-state structures of **1-Zn** and **3-Zn**, while, unfortunately, no single-crystal suitable for XRD analysis was obtained for **1-Cu**, **3-Cu**, **1-Cu(OH)** and **3-Cu(OH)**, as mentioned above. Crystal structural data, together with the simulated and experimental PXRD patterns of the Zn-based compounds, are reported in Appendix C. The tetra-anionic octadentate tectons act as linking units, connecting two distinct Zn(II) atoms through a dimeric paddlewheel type motif with a Zn–Zn distance of ca. 2.98 Å. The Zn(II) centers adopt a distorted square pyramidal geometry with average Zn–O distances of 2.056 Å for **1-Zn** and 2.118 Å for **3-Zn**. The coordination sphere around each metal node, composed of four oxygen atoms belonging to carboxylate moieties, is completed with a water molecule. The 3D architectures form an interconnected network of cavities of two distinct sizes and shapes: a large ovaloid cavity (14 Å x 14 Å x 25 Å) and a smaller spherical cavity with 13 Å in diameter (see Figure 2). Every spherical cage presents two free carboxylate sites, which allow to interconnect the 1D networks in the other two dimensions. This results in a tridimensional framework tailored with mono-dimensional chiral channels formed by different sized cavities. The free volumes explored by a sphere of 1 Å radius by PLATON account for 53% (6280 Å³) and 52% (6148 Å³) of the unit cell volume for **1-Zn** and **3-Zn**, respectively. Interestingly, the inner walls of the nanochannels are decorated with the chiral fragments of the organic tectons, thus creating a chiral confined environment, suitable for hosting small molecules, as highlighted in Figure 3.

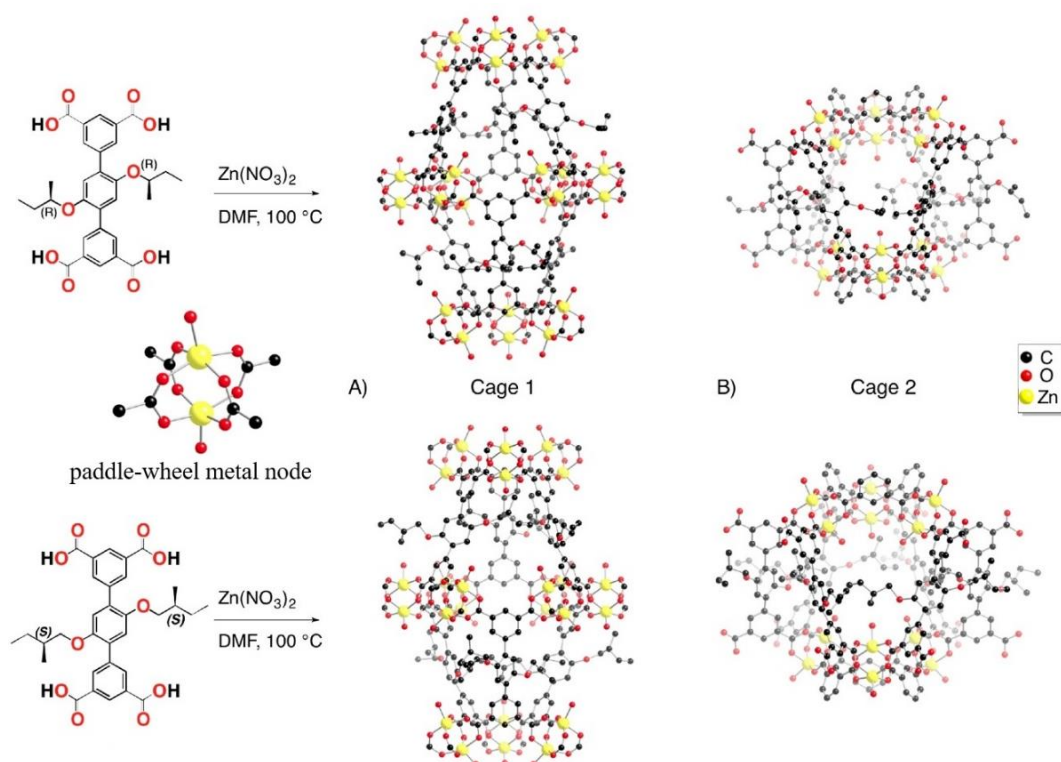


Figure 2. Section of 1-Zn and 3-Zn crystal structures showing: a) the ovaloid-type cage and b) the spherical-type cage.

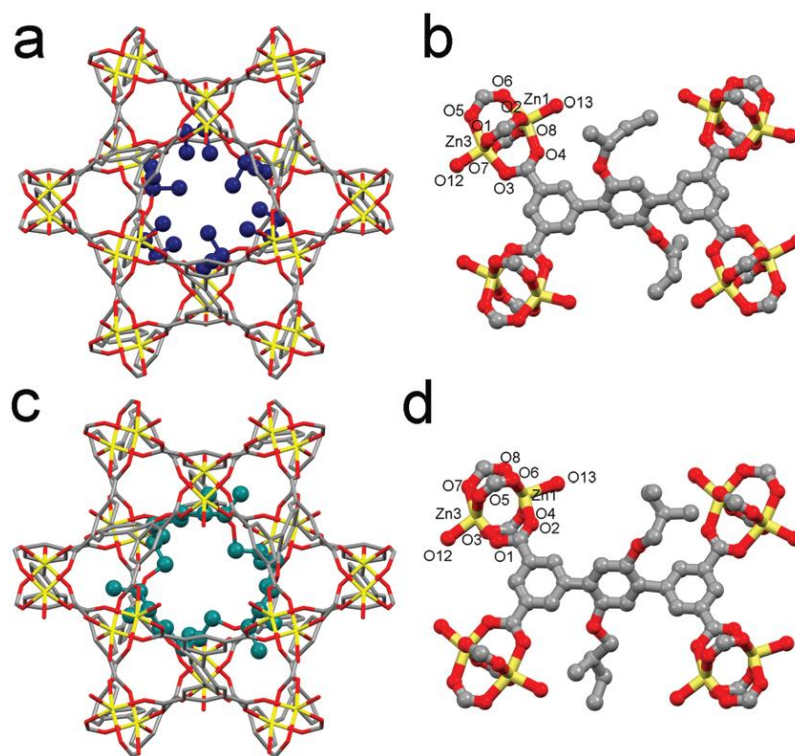


Figure 3. Portions of the crystal structure of 1-Zn (a) and 3-Zn (c) showing the two types of channels along the c axis. The substituents bearing the stereogenic centers pointing towards the interior of the channel are differentiated by color (blue for 1-Zn and green for 3-Zn). Hydrogen atoms and solvent molecules are omitted for clarity.

The crystalline frameworks of **1-Zn** and **3-Zn** were prepared in quantity sufficient for powder diffraction and thermogravimetric analyses, in order to determine their phase purity and thermal stability. In both cases, the PXRD patterns confirmed that the synthetic and crystallization conditions used provided pure homo-chiral samples. The experimental PXRD patterns are in perfect agreement with the simulated ones calculated from the single-crystal data, as shown in Figure 4.

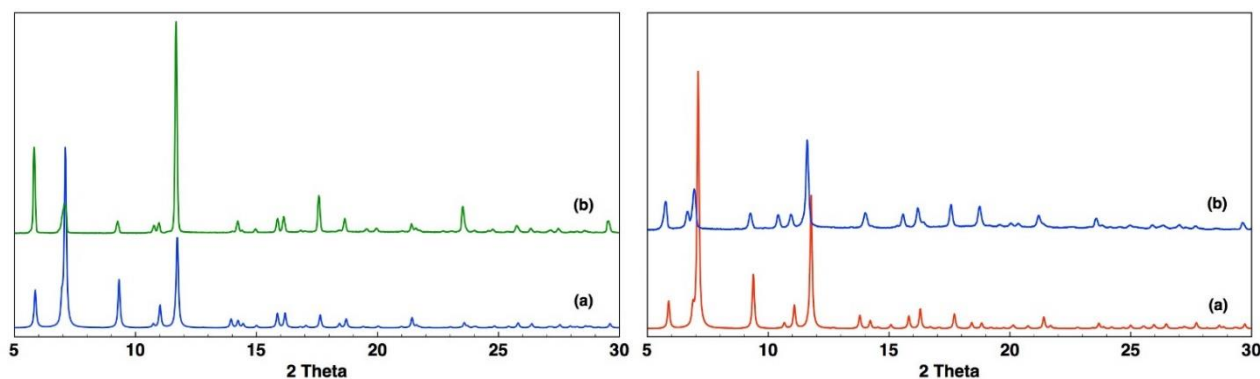


Figure 4. Simulated (a) and experimental (b) PXRD patterns of **1-Zn** (left) and **3-Zn** (right).

The thermal stability of **1-Zn** and **3-Zn** was analyzed via TGA from 25° to 500°C (5°/min) under nitrogen flux, as reported in Figure 5. For **1-Zn**, the main weight losses are observed in the range 25° - 300°C, due to the evacuation of the crystallization solvent molecules from the channels and to the water molecules bond to the cationic nodes. From 300°C, the structure starts to degrade. For **3-Zn**, the first weight loss at 190°C is attributed to the evaporation of the solvent molecules and from 300°C there is the thermal degradation of the crystalline structure. To confirm that the two materials retain their crystallinity after the desolvation process, the powders were washed with abundant acetone and dried under vacuum for 24 hours. Then, PXRD analysis was performed in both cases and it proved the good crystallinity of **1-Zn** and **3-Zn**.

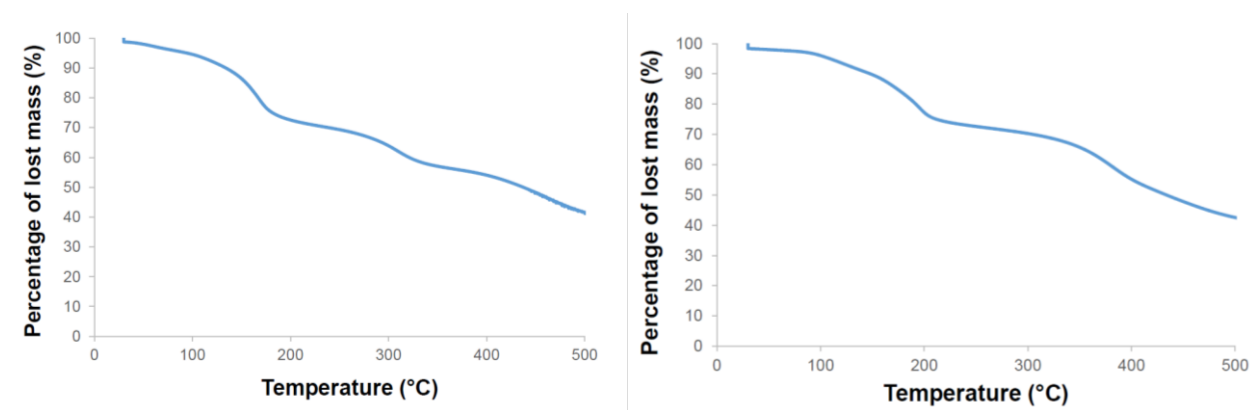


Figure 5. Thermogravimetric analyses (TGA) of **1-Zn** (left) and **3-Zn** (right).

Cu(II) salts are known to produce crystalline architectures similar to those obtained with Zn(II). Combining the same organic tectons of **1**-Zn and **3**-Zn with Cu(NO₃)₂ salts, the tridimensional frameworks **1**-Cu and **3**-Cu were synthesized. Their reaction in DMF at 85 °C, in presence of a small amount of HCl, afforded after 24 hours polycrystalline powders. The same crystallization conditions were applied for the synthesis of **1**-Cu(OH) and **3**-Cu(OH), whose linkers differ just for the chiral chains. In these cases, no single-crystal suitable for XRD analysis was obtained. Despite the lack of single-crystal structures for the copper-based MOFs, we were able to compare the powder X-ray diffraction patterns of polycrystalline powders of all the frameworks (Figure 6), revealing a good match between them. Thus, it seems reasonable to assume that the Cu-networks are isostructural with **1**-Zn and **3**-Zn.

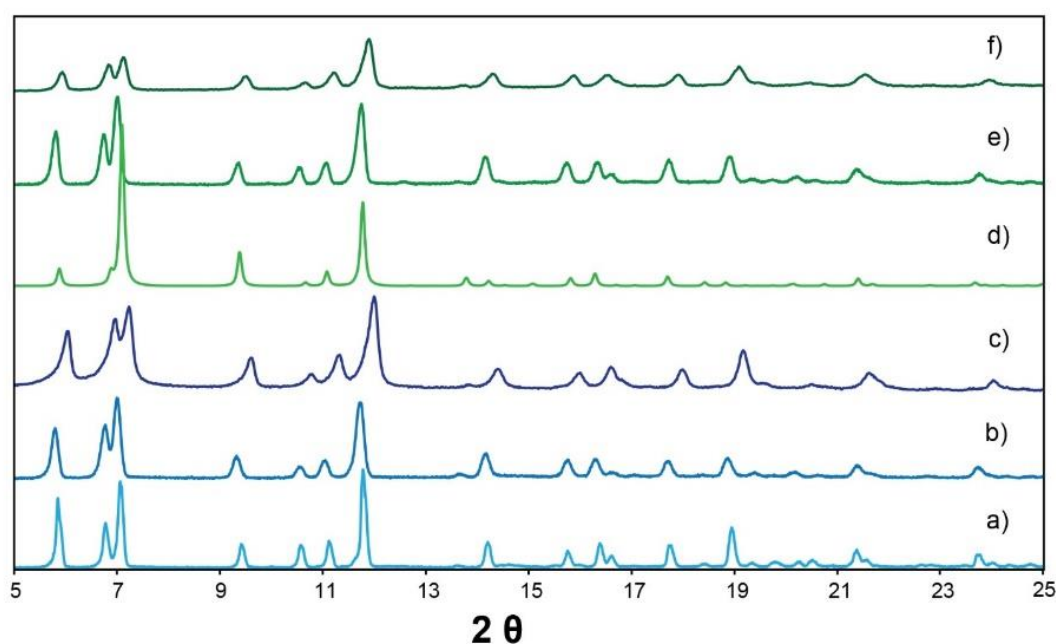


Figure 6. PXRD patterns of: **1**-Zn (a); **1**-Cu (b); **1**-Cu(OH) (c); **3**-Zn (d); **3**-Cu (e) and **3**-Cu(OH) (f).

After the PXRD measurements, the MOFs were activated by solvent exchange with methanol and dichloromethane, followed by heating at 120 °C under dynamic vacuum for 12 h, to prove their permanent porosity. Unfortunately, the zinc-based crystals were found to be unstable in dichloromethane and thus it was not possible to generate porous frameworks. However, **1**-Cu, **3**-Cu, **1**-Cu(OH) and **3**-Cu(OH) resisted to the exchange in different solvents (CH₂Cl₂ and THF, for example) and could be activated. By PXRD patterns, we established that the Cu-based 3D networks retained their crystallinity after the soaking in solvent (see Appendix C). The thermal stability of the activated copper crystals was studied using TGA, which revealed that they were stable up to ca 300 °C (Figure 7). This temperature was necessary to determine the adequate thermal treatment before the gas adsorption measurements.

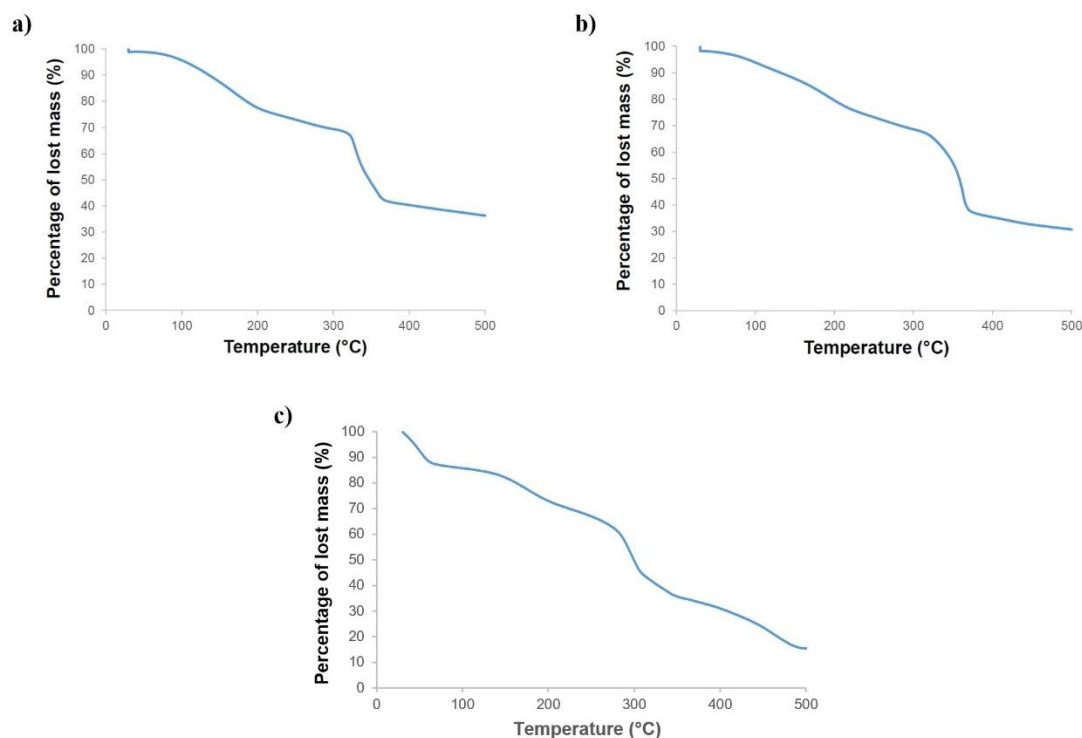


Figure 7. Thermogravimetric analyses (TGA) of: a) **1-Cu**; b) **3-Cu**; c) **1- and 3-Cu(OH)** MOFs.

In the case of **1-Cu(OH)** and **3-Cu(OH)** MOFs, their enantiopurity was proved to resist after the solvent removal, as we demonstrated by circular dichroism measurements, as shown in Figure 8.

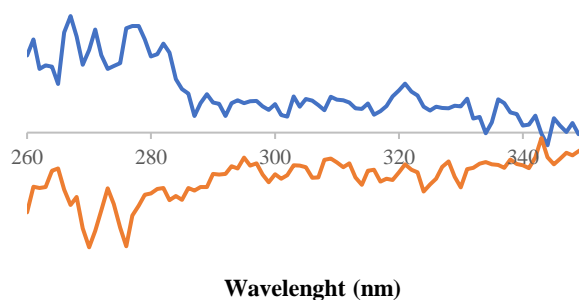


Figure 8. Circular dichroism measurements of **1-Cu(OH)** (blue) and **3-Cu(OH)** (orange) MOFs.

4.3 Gas adsorption properties

After activating the Cu-based MOFs for 8 hours at 120 °C in high vacuum, we demonstrated the permanent porosity by N₂ at 77 K adsorption-desorption measurements. The adsorption isotherms show a sharp uptake at low pressure and the curves display type-I profiles, typical of microporous solids. The BET surface areas were established to be 930 m²/g, 954 m²/g, 580 m²/g and 630 m²/g for **1-Cu**, **3-Cu**, **1-Cu(OH)** and **3-Cu(OH)**, respectively. CO₂ adsorption isotherms at 195 K confirmed the porosity, as shown in Figure 9. All the isotherms exhibited Langmuir profiles, with plateau values of about 243 cm³ (STP)/g at 1 bar for **1-Cu** and **3-**

Cu and 155 cm³(STP)/g at 1 bar for **1**-Cu(OH) and **3**-Cu(OH). The measured CO₂ capacities correspond to an occupied volume of 0.62 cm³/g (CO₂ density (l) = 0.77 g/cm³ was used), which matches the pore volumes of 0.57 and 0.59 cm³/g for **3**-Cu and **1**-Cu respectively, as estimated by considering the crystal density and pore volume explored by a sphere having a radius of 1.2 Å.

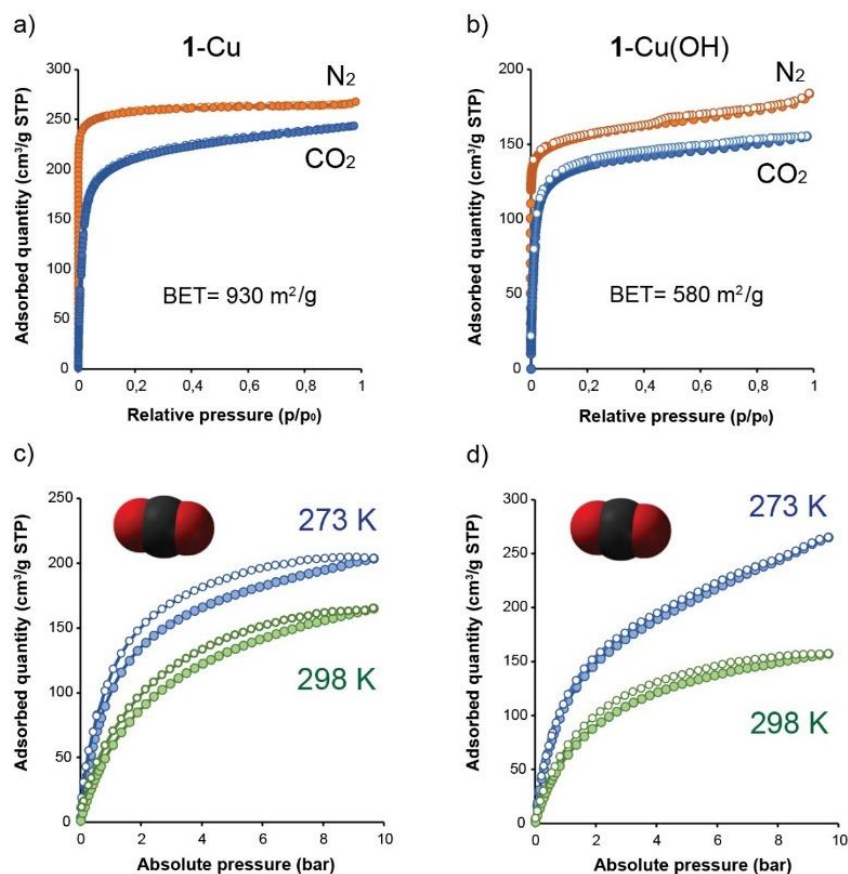


Figure 9. Gas adsorption isotherms: (a) N₂ at 77 K and CO₂ at 195 K of **1**-Cu; (b) N₂ at 77 K and CO₂ at 195 K of **1**-Cu(OH); (c) CO₂ at 273 and 298 K of **1**-Cu up to 10 bar; (d) CO₂ at 273 and 298 K of **1**-Cu(OH) up to 10 bar.

The almost complete filling of the empty spaces in the crystal structures, proved by the adsorption measurements, indicated the easy accessibility of the cavities to diffusing gases. Thanks to the promising porosity, we tested the storage capacities of the copper-based frameworks under mild conditions. Nitrogen and carbon dioxide adsorption isotherms were collected up to 10 bar at 273 K and room temperature¹⁹ (see Figure 9). Dealing with CO₂ capture, **1**-Cu shows Type-I isotherms and total absorbed amounts of 165 and 203 cm³(STP)/g, corresponding to 32% and 40% of the host weight at a moderate pressure of 10 bar. Similarly, for **1**-Cu(OH), the maximum quantity adsorbed is 157 and 265 cm³(STP)/g at 298 and 273 K, respectively. The isosteric heat of CO₂ adsorption, determined by applying the Van't Hoff equation, is 27 kJ/mol for **1**-Cu and **3**-Cu. These values agree with reported data for porous crystals and MOFs without open metal sites or specific interactions with pores' walls²⁰⁻²². On the contrary, N₂ adsorption measurements displayed poor uptake even at high pressure, indicating low affinity between the MOFs and nitrogen. This considerable difference in

affinity of the Cu-based networks for the two gases may suggest their application for a selective separation of carbon dioxide in a mixture with nitrogen. All the gas adsorption isotherms for **3**-Cu and **3**-Cu(OH) are reported in Appendix C. Furthermore, the porous crystals of **1**-Cu and **3**-Cu were checked for methane storage²³. CH₄ isotherms for both compounds exhibit Langmuir profiles, reaching a binding energy of 18 kJ/mol (see Appendix C). This value is rather high and may be accounted for by multiple van der Waals interactions between the hydrocarbon pendant groups and the gas²⁴. Similar values have been obtained for porous molecular crystals displaying pores lined with hydrocarbon moieties²⁵.

4.4 Enantioselectivity experiments

The chiral and porous nature of the Cu-based frameworks prompted us to explore the enantioselective recognition of various guests²⁶⁻²⁹. The work was divided in two parts, investigated with different techniques. We first dedicated our attention to **1**-Cu and **3**-Cu MOFs, which differ just in a -CH₂ group on the alkyl fragments bond to the tectons' central phenyl rings. **3**-Cu, indeed, present longer mobile chains and the stereogenic carbons are more distant from the oxygen atoms compared to **1**-Cu. The first approach chosen was the adsorption of enantiopure solutions inside the chiral nanochannels of **1**-Cu and **3**-Cu monitored through absorbance spectroscopy during time. The essential amino acid tryptophan was selected as a promising guest for its active biological role in the production of serotonin and melatonin. The selective adsorption of (*D*)- and (*L*)-tryptophan in water solution was tested for 24 hours through UV-Vis measurements. Thus, it was possible to determine the enantioselectivity properties respect to the single enantiomers for both the 3D networks. The second part represented one step forward in this investigation and concerned the use of the high performance liquid chromatography for the resolution of racemic mixtures of small chiral molecules, employed as pharmaceutical precursors. In this case, **1**-Cu(OH) and **3**-Cu(OH) were put in THF with racemic solutions and on the products deriving from the soaking experiments were analyzed by HPLC to determine the enantiomeric excess values and the enantioselectivity capabilities of these MOFs.

4.4.1 Chiral uptake of (*D*)- and (*L*)-tryptophan

To address the enantioselectivity properties of **1**-Cu and **3**-Cu, we performed adsorption measurements in enantiomerically pure solutions of (*D*)- and (*L*)-tryptophan. The target was to test the recognition power of the chiral units pointing towards the interior of the nanochannels. The choice of the guest fell on a molecule coming from the natural world and involved in important biochemical processes, like tryptophan. Tryptophan is an α -amino acid and it is one of the eight essential amino acids to the human body, since we cannot produce it by ourselves, but it must be supplied by the diet. It is a precursor to the neurotransmitter serotonin and to the hormone melatonin³⁰. As for all the other amino acids, only the *L* isomer is used in protein synthesis³¹ and can pass across the blood-brain barrier^{32,33}. Therefore, it results of great relevance to separate the two tryptophan's isomers for any possible pharmaceutical application. Moreover, tryptophan presents good dimension fitting with the MOFs' pores, thanks to the indole group steric hindrance. Prior to adsorption studies, the stability and crystallinity of **1**-Cu and **3**-Cu in water at room temperature were investigated. Tryptophan's

poor solubility in organic solvents, indeed, forced us to use water. After immersion in water for 24 hours under magnetic stirring of the crystalline materials, the samples were dried out in vacuum and the microcrystalline powders were studied by PXRD, which revealed the integrity of both materials (see Appendix C). The high stability in water represents a promising feature for these structures, since generally MOFs are water-sensitive and their application in biomedical fields is strongly inhibited. For the uptake processes, we first activated **1**-Cu and **3**-Cu crystals by heating them at 120 °C for 8 hours in high vacuum; then the powders were immersed in an aqueous solution containing pure (*L*)- or (*D*)-tryptophan, using a concentration tested to afford an absorbance easily detectable by UV-vis spectroscopy (in fact, 3.3×10^{-3} M). The guest absorption capacity through time was monitored by measuring the intensity of the band at 280 nm of tryptophan in solution, as reported in Figure 10.

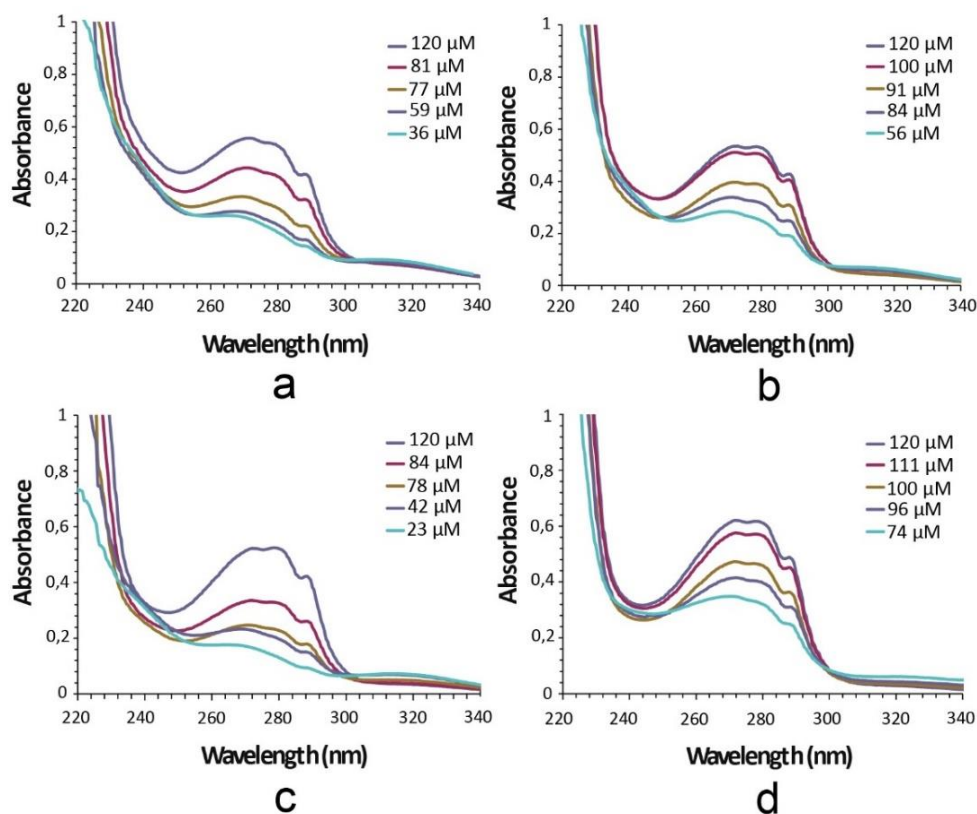


Figure 10. UV-vis absorption spectra at variable concentrations as a function of time containing enantiopure (*D*)-tryptophan (a and c) and (*L*)-tryptophan (b and d) for **1**-Cu (a and b) and **3**-Cu (c and d), respectively.

The absorption data were recorded every 30 minutes for the first two hours, then every 60 minutes for six hours. Upon uptake of tryptophan by the porous materials, the intensity of the peak measured in solution decreased until it reached a plateau. To ensure the host-guest system has gone to equilibrium, we registered absorption spectra after 24 hours. After two hours of adsorption in solution, the systems reached absorbance plateau values, indicating the establishment of equilibrium, as reported in Figure 10. The absorbance values after 24 hours were almost exactly the same as after two hours. From the concentration values, calculated using

the calibration line, the enantioselective recognition was evaluated as a function of time (see Figure 11). It clearly appears from the graphs in Figure 10 that there is strong difference in the adsorption rates at short times for both the MOFs, and this is accentuated in the case of **3**-Cu. The enantioselectivity is therefore correlated to the adsorption kinetics in solution, whereas at equilibrium the enantioselectivity ability of these materials is lower. While enantioselective performance was negligible in the case of **1**-Cu, **3**-Cu adsorbs preferentially (*L*)-tryptophan. Just after 30 min, 66% of (*L*)- and 20% of (*D*)-tryptophan were adsorbed from the solution in a ratio of 3.3 : 1. Higher ratios up to 4 : 1 were obtained at shorter times of guest uptake; this is the confirmation that high enantioselectivity can be most favorably achieved far from the equilibrium conditions. Once known the guest uptake, we wanted also to determine the quantity of tryptophan which can be released in water. The capability to store and release in a controlled manner the drugs is a fundamental characteristic for all nanomedicine delivery devices. Therefore, we needed to understand how the loaded MOFs could interact with an aqueous environment, similar to the physiological solutions present in the human body. Small amounts of **1**-Cu and **3**-Cu after tryptophan adsorption were dissolved in water and the guest releasing was monitored by UV-vis following the same procedure used for the first part. The desorption process showed that, after 24 hours, a minor amount of guest (2.5–4.9%) is released from the adduct, indicating the occurrence of strong host–guest interactions (see Figure 12). The higher stereoselectivity of **3**-Cu with respect to **1**-Cu can be explained by the longer alkyl fragments bearing the stereogenic carbons at their ends, which protrude towards the center of the cavities and recognize more efficiently one of the enantiomers. However, the flexibility of these side-chains promotes guest diffusion but does not allow high enantioselectivity values. With the aim of exploring selective chiral uptake and separation ability of other small molecules such as amines and alcohols, we focused our attention on the other two Cu-based frameworks, which are characterized by chiral hydroxyl groups. These functional groups have a larger steric hindrance compared to the chiral methyl fragments of **1**-Cu and **3**-Cu, and can be exploited for hydrogen bonding interaction with the guest molecules.

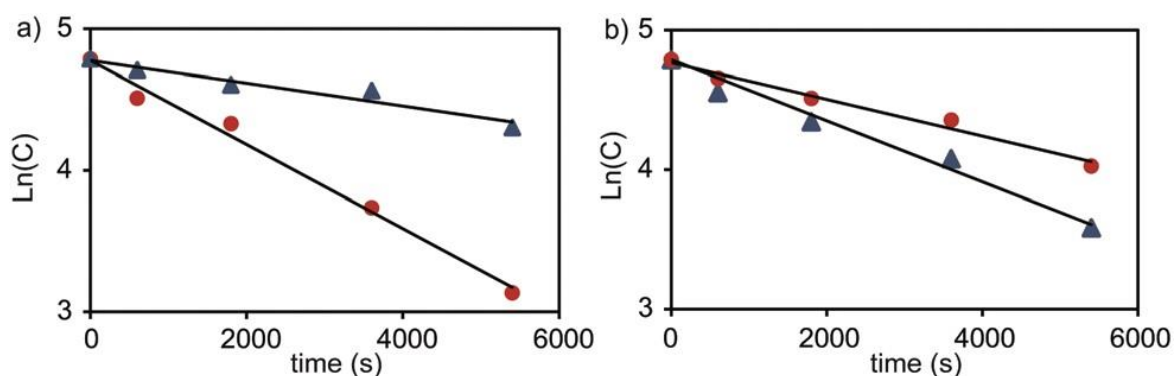


Figure 11. Plot of guest concentration (C) versus time for (a) **3**-Cu and (b) **1**-Cu MOFs. (*L*)- and (*D*)-tryptophan are indicated as circles and triangles, respectively.

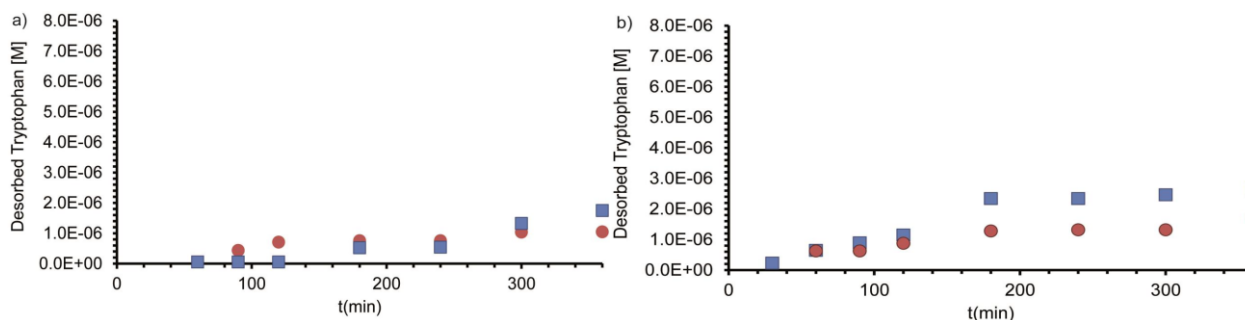


Figure 12. Desorbed tryptophan versus time of a) 1-Cu and b) 3-Cu. D-tryptophan (circles) and L-tryptophan (squares).

4.4.2 Enantioselective separation of small molecules

The presence of nanochannels, decorated with hydroxyl groups on the homo-chiral stereogenic centers, as shown in Figure 13, pushed our study to pass from enantioselective recognition to separation of racemic mixtures of small molecules.

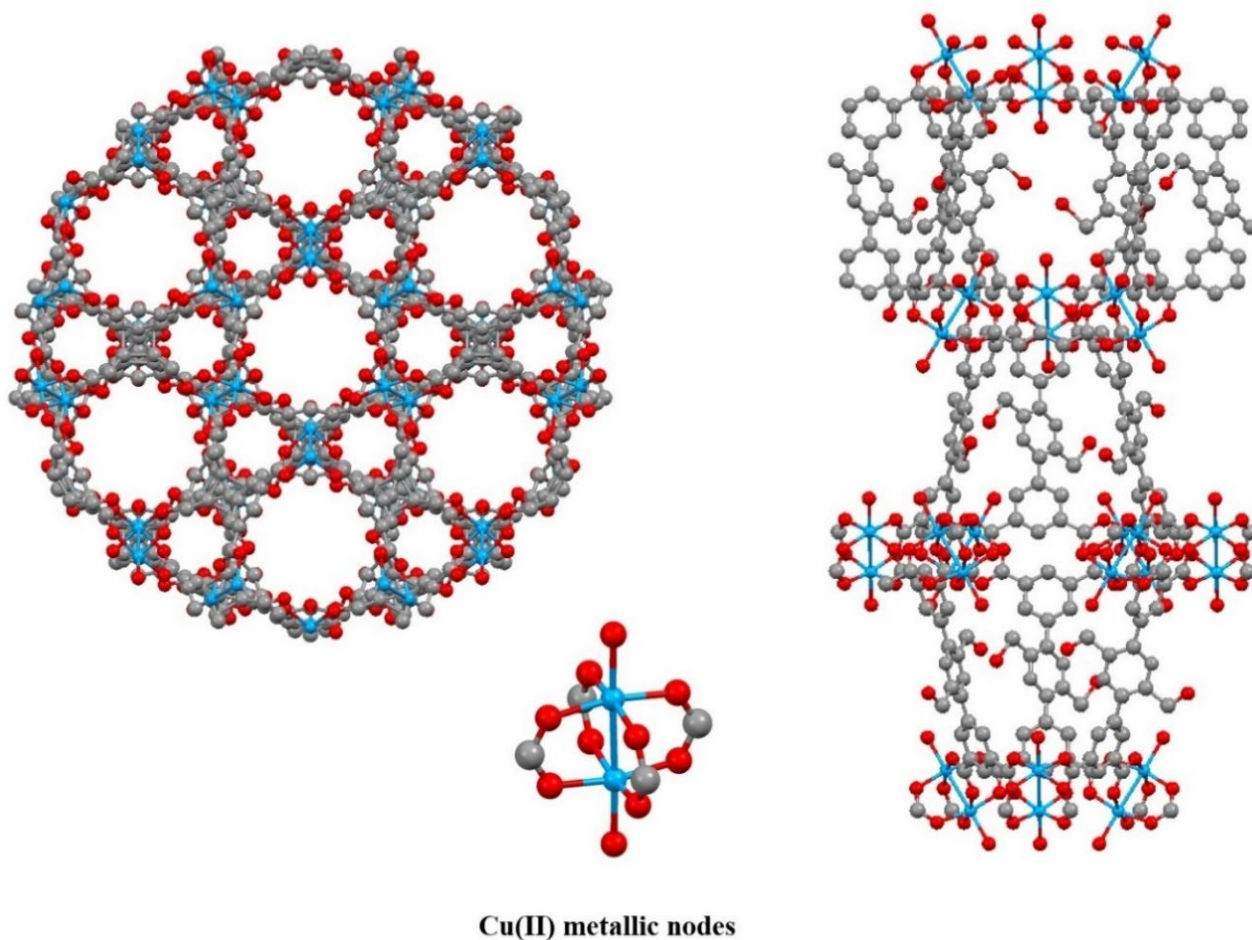


Figure 13. Sections of the OH-MOFs channels (elaborated by substituting 1-Zn tectons with 1-Cu(OH) chiral fragments in the crystal structure). In blue copper, in red oxygen and in grey carbon atoms.

Passing from the uptake of enantiopure guests to the resolution of racemic mixtures represented a challenging step forward to the practical employment of homo-chiral MOFs in chromatographic techniques. We began by choosing primary alkyl amines and amides as guests for **1**-Cu(OH) and **3**-Cu(OH). Many pharmaceutical drugs contain enantiomerically pure amines and amides as intermediates, thanks to their important role in biological activities³⁴. Moreover, the resolution of racemic amines and amides still constitutes a demanding challenge, since metal-organic frameworks are often sensitive to these kinds of substances. The choice of the guests fell on *sec*-butylamine, α -methylbenzylamine and *N-sec*-butyl benzamide. These molecules, besides their interesting properties as pharmaceutical precursors, possess steric dimensions which should fit the empty space available inside the OH-MOFs. To prove the effective adsorption of *sec*-butylamine in the two MOFs, preliminary adsorption measurements were conducted at 273 K, as illustrated in Figure 14. Thanks to the high volatility (b.p. 63°C), butylamine is the ideal guest for adsorption from the vapor phase. Here, the adsorption isotherms of the single butylamine enantiomers follow the Langmuir-type shape and establish the efficient capture of the amines by the MOFs, without stability loss. After that, the adsorption process with the racemic guests was conducted in solution, as done for the other frameworks. This time, tetrahydrofuran was chosen as a solvent, because it can well solubilize the guests, but it doesn't destroy the crystallinity of the two MOFs. After the thermal treatment described in the previous paragraph, the evacuated crystalline powders were soaked in a solution of THF and racemic *sec*-butylamine under magnetic stirring for two hours. Then, the frameworks were filtered and washed several times with THF.

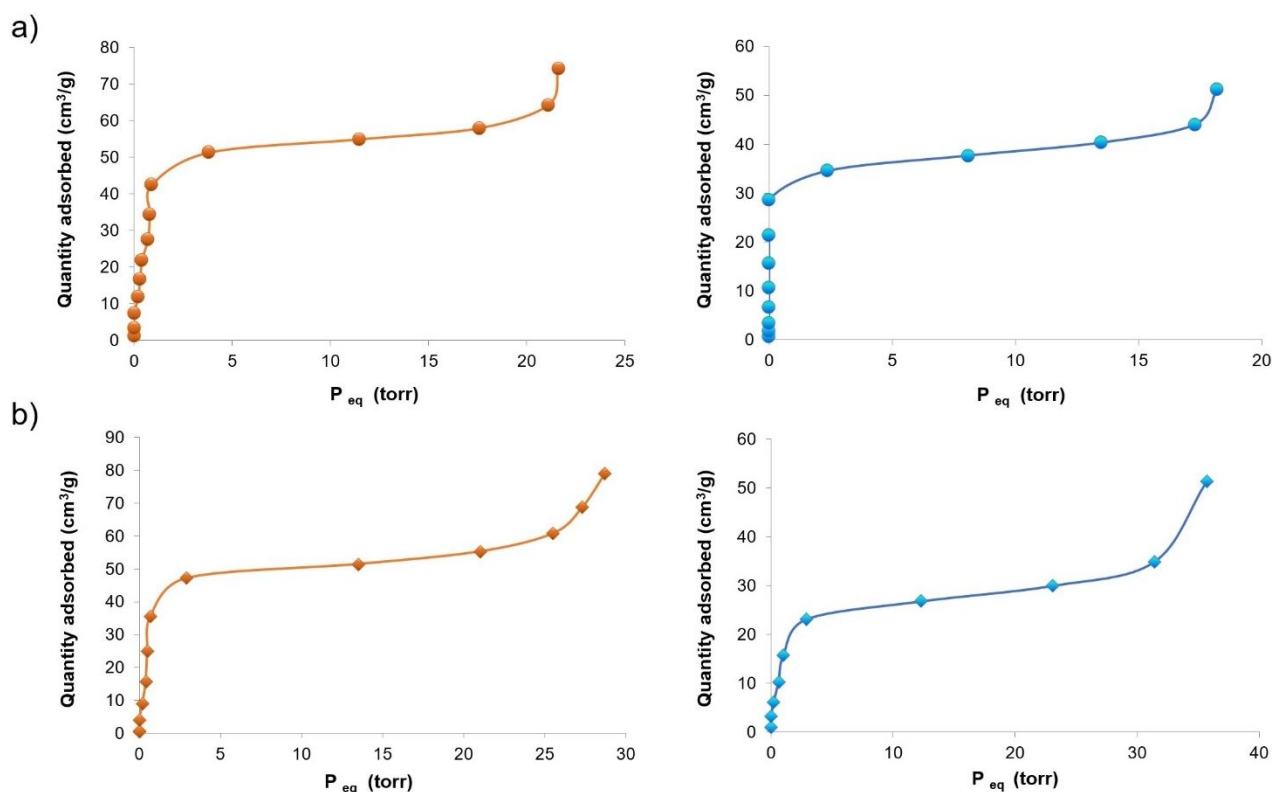


Figure 14. Adsorption isotherms at 273 K of *S*-butylamine (orange) and *R*-butylamine (blue) in a) **1**-Cu(OH) and b) **3**-Cu(OH).

We kept both the solutions from the soaking and from the extraction and we performed benzoylation on the alkyl butylamines. This derivatization was necessary to obtain aromatic products that can be analyzed by the UV-vis detector of the HPLC system. Unfortunately, the reaction did not work for the solutions coming from the MOFs washing; tested by NMR, it was highlighted that no guest was present in the solutions extracted from the frameworks. After the soaking, small amounts of MOFs were dissolved in deuterated trifluoroacetic acid and DMSO to detect the presence of the guest molecules inside the structures; the ^1H NMR spectra clearly show that the guests are present in really scarce quantities compared to the organic ligands peaks (see Appendix C). Therefore, I performed the derivatization and the HPLC analysis only on the soaking supernatant solutions. Racemic benzoylated *sec*-butylamines were successfully resolved on the chiral stationary phase of the HPLC column (see details in Appendix A) with hexane/isopropanol (90:10 v/v) as the mobile phase at a flow rate of 1 ml/min at room temperature. The chromatographic resolution was achieved in 20 min and the elution sequence was the *R*-enantiomer followed by the *S*-enantiomer. Both enantiomer peaks were completely resolved, with more than one minute of retention time between one another. This sequence was determined by testing an enantiomerically pure sample of benzoylated *S*-butylamine before the racemic compounds. The analysis was fast to be completed and with no byproducts residues from the derivation reaction in the chromatograms. From these first experiments, the enantioselective ability of both the two MOFs resulted to be low, as proven by the calculated enantiomeric excesses. For **1**-Cu(OH), there is a slight preference for *R*-butylamine, with an enantiomeric excess of 0.6%, while **3**-Cu(OH) preferentially absorbs the *S*-enantiomer, with a larger ee of about 3%. The HPLC chromatograms are reported in Figure 15.

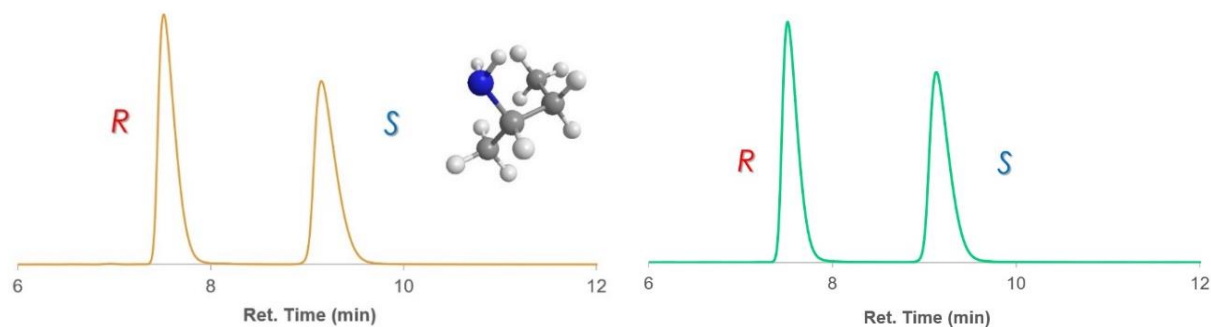


Figure 15. HPLC separation of racemic *sec*-butylamine on **3**-Cu(OH) (left in orange) and **1**-Cu(OH) (right in green).

These low enantioselectivity values can be explained by the small size of the *sec*-butylamine, which make hard to recognize the two enantiomers simply by steric hindrance. Since **3**-Cu(OH) appeared to be more promising compared to the related compound **1**-Cu(OH), its enantioselectivity power was tested also for aromatic guests, such as α -methylbenzylamine and *N*-*sec*-butyl benzamide. The soaking procedure in THF applied for the racemic aromatic guests is the same previously described for *sec*-butylamine. Analyzed by HPLC, very low enantiomeric excess values were found out, in particular decreasing with the increasing of the guest steric incumbrance. Therefore, the next step was determining the rate of adsorption of aromatic guests inside the nanochannels, in order to understand the reason of this negligible guest uptake. The adsorption kinetics of α -

methylbenzylamine in **1**-Cu(OH) was monitored through absorbance spectroscopy in acetonitrile solution, whose UV-vis cutoff absorption starts at 190 nm. Just the 14,8% of guest was adsorbed after 24 hours (see Appendix C), motivating the low uptake and the scarce selectivity. It is therefore reasonable to assume that aromatic molecules present steric difficulties to penetrate inside the nanochannels of **1**-Cu(OH) and **3**-Cu(OH) and cannot be easily separated. This low uptake could be also addressed to THF, which polarity is not probably adequate for the adsorption process, since it is known that the use of polar solvents favors the guests capture^{16c}. Both the OH-MOFs were not stable in more polar solvents, like water or methanol, therefore the limited range of solvents that can be employed makes experiments in solution quite difficult to be performed. Moreover, the difficult adsorption process for aromatic molecules limits also the number of possible guests. The choice of longer-chained aliphatic amines and/or alcohols as guests can represent a good compromise for future investigations on the enantioselectivity of these and similar homo-chiral metal-organic frameworks.

4.5 Conclusions

In conclusion, four new enantiomerically pure organic tectons, bearing four carboxylate moieties as coordinating sites and two chiral appended chains were designed and prepared. Their reaction, under hydrothermal conditions in DMF, with Cu(II) cations as metallic nodes leads to the formation of enantiomerically pure porous crystals with their space occupied by the chiral chains. The crystalline materials are robust and exhibit permanent porosity and high thermal stability. The latter solid-state architectures were shown to uptake guest molecules, as they capture N₂, CO₂ and CH₄ molecules. The sorption of CO₂ takes place at room temperature and under rather low pressure (10 bar). Interestingly, the porous crystals show high affinity for CO₂ with respect to N₂. Furthermore, **1**-Cu and **3**-Cu were shown to adsorb D- and L-tryptophan from water. Interestingly, **3**-Cu preferentially adsorbed L-tryptophan: the amount of adsorbed L- versus D-tryptophan resulted in a ratio higher than 3.3 : 1 after 30 min. The 3D structures **1**-Cu(OH) and **3**-Cu(OH) were tested for the enantioselective separation of small molecules. After soaking with sec-butylamine racemic mixtures, the HPLC analyses showed complete peak resolution and fast retention time, but low enantiomeric excess values due to the very small dimensions of the guest. These first experiments represent the starting point of a deeper investigation of selective chiral uptake and separation of other chiral molecules such as alcohols by homo-chiral porous crystalline architectures.

4.6 References

- 1** (a) H.-C. Zhou and S. Kitagawa, *Chem. Soc. Rev.*, **2014**, 43, 5415; (b) S. Lee, E. Kapustin and O. M. Yaghi, *Science*, **2016**, 353, 808; (c) J.-R. Li, J. Sculley and H.-C. Zhou, *Chem. Rev.*, **2012**, 112, 869; (d) G. Férey, *Chem. Soc. Rev.*, **2008**, 37, 191.
- 2** N. B. McKeown, *J. Mater. Chem.*, **2010**, 20, 10588; J. R. Holst, A. Trewin and A. I. Cooper, *Nat. Chem.*, **2010**, 2, 915; P. Sozzani, S. Bracco, A. Comotti, L. Ferretti and R. Simonutti, *Angew. Chem.Int. Ed.*, **2005**, 44, 1816.
- 3** S. Freiberg and X. X. Zhu, *Int. J. Pharm.*, **2004**, 282, 1.
- 4** K. S. Soppimath, T. M. Aminabhavi, A. R. Kulkarni and W. E. Rudzinski, *J. Controlled Release*, **2001**, 70, 1.

- 5 P. Dhivanand and O. L. Sprockel, *Int. J. Pharm.*, **1998**, 167, 83.
- 6 A. Rivera and T. Farias, *Microporous Mesoporous Mater.*, **2005**, 80, 337.
- 7 M. Vallet-Regi, A. Ramila, R. P. del Real and J. Perez-Pariente, *Chem. Mater.*, **2001**, 13, 308.
- 8 B. Munoz, A. Ramila, J. Perez-Pariente, I. Diaz and M. Vallet-Regi, *Chem. Mater.*, **2003**, 15, 500.
- 9 (a) M. Simard, D. Su and J. D. Wuest, *J. Am. Chem. Soc.*, **1991**, 113, 4696; (b) S. Mann, *Nature*, **1993**, 365, 499; (c) M. W. Hosseini, *Acc. Chem. Res.*, **2005**, 38, 313.
- 10 M. W. Hosseini, *CrystEngComm*, **2004**, 6, 318.
- 11 Wagniere, G. H., *On Chirality and the Universal Asymmetry: Reflections on Image and Mirror Image* (Wiley-Verlag Helvetica Chimica Acta, **2007**).
- 12 Stinson, S. C., Chiral pharmaceuticals. *Chem. Eng. News*, **2001**, 79, 79.
- 13 Liu, Y., Xuan, W. & Cui, Y., *Adv. Mater.*, **2010**, 22, 4112.
- 14 Ward, T. J. & Ward, K. D., *Anal. Chem.*, **2012**, 84, 626.
- 15 (a) V. N. Yadav, A. Comotti, P. Sozzani, S. Bracco, T. Bonge-Hansen, M. Hennumand C. H. Gorbitz, *Angew. Chem., Int. Ed.*, **2015**, 54, 15684; (b) S.-Y. Zhang, L. Wojtas and M. J. Zaworotko, *J. Am. Chem. Soc.*, **2015**, 137, 12045; (c) A. Comotti, S. Bracco, G. Distefano and P. Sozzani, *Chem. Commun.*, **2009**, 284; (d) A. Comotti, A. Fraccarollo, S. Bracco, M. Beretta, G. Distefano, M. Cossi, L. Marchese, C. Riccardi and P. Sozzani, *CrystEngComm*, **2013**, 15, 1503; (e) C. Zhou, Y. Wen and X. Wu, *CrystEngComm*, **2016**, 18, 2792; (f) D. N. Dybtsev, A. L. Nuzhdin, H. Chun, K. P. Bryalikov, E. P. Talsi, V. P. Fedin and K. Kim, *Angew. Chem., Int. Ed.*, **2006**, 45, 916; (g) Z.-X. Xu, Y.-X. Tan, H.-R. Fu, Y. Kang and J. Zhang, *Chem. Commun.*, **2015**, 51, 2565; (h) Z.-X. Xu, Y.-L. Ma and J. Zhang, *Chem. Commun.*, **2016**, 52, 1923; (i) Z.-G. Gu, C. Zhan, J. Zhang and X. Bu, *Chem. Soc. Rev.*, **2016**, 45, 3122; (j) Z.-X. Xu, H.-R. Fu, X. Wu, Y. Kang and J. Zhang, *Chem. Eur. J.*, **2015**, 21, 10236.
- 16 (a) D. Bradshaw, T. J. Prior, E. J. Cussen, J. B. Claridge and M. J. Rosseinsky, *J. Am. Chem. Soc.*, **2004**, 126, 6106; (b) Y. Liu, W. Xuan and Y. Cui, *Adv. Mater.*, **2010**, 22, 4112; (c) Y. Peng, T. Gong, K. Zhang, X. Lin, Y. Liu, J. Jiang and Y. Cui, *Nat. Commun.*, 2014, 5, 4406.
- 17 D. Asnaghi, R. Corso, P. Larpent, I. Bassanetti, A. Jouaiti, N. Kyritsakas, A. Comotti, P. Sozzani and M. W. Hosseini *Chem. Commun.*, 2017, 53, 5740.
- 18 P. Larpent, A. Jouaiti, N. Kyritsakas and M. W. Hosseini, *Chem. Commun.*, **2013**, 49, 4468.
- 19 Y. He, B. Li, M. O’Keeffe and B. Chen, *Chem. Soc. Rev.*, **2014**, 43, 5618.
- 20 (a) J. R. Li, R. J. Kuppler and H. C. Zhou, *Chem. Soc. Rev.*, **2009**, 38, 1477; (b) H. Zhang, P. Deria, O. K. Farha, J. T. Hupp and R. Q. Snurr, *Energy Environ. Sci.*, **2015**, 8, 1501.
- 21 (a) Y. Peng, V. Krungleviciute, I. Eryazici, J. T. Hupp, O. K. Farha and T. Yildirim, *J. Am. Chem. Soc.*, **2013**, 135, 11887; (b) H. C. Zhou, J. R. Long and O. M. Yaghi, *Chem. Rev.*, **2012**, 112, 673.
- 22 J. A. Mason, J. Oktawiec, M. K. Taylor, M. R. Hudson, J. Rodriguez, J. E. Bachman, M. I. Gonzales, A. Cervellino, A. Guagliardi, C.M. Brown, P. L. Llwellyn, N. Masciocchi and J. R. Long, *Nature*, **2015**, 527, 357.
- 23 (a) Z. Guo, H. Wu, G. Srinivas, Y. Zhou, S. Xiang, Z. Chen, Y. Yang, W. Zhou, M. O Keeffe and B. Chen, *Angew. Chem., Int. Ed.*, **2011**, 50, 3178; (b) D. Yuan, D. Zhao, D. Sun and H. C. Zhou, *Angew. Chem., Int. Ed.*, **2010**, 49, 5357.

- 24** S. Gao, C. J. Morris, Z. Lu, Y. Yan, H. G. W. Godfrey, C. Murray, C. C. Tang, K. M. Thomas, S. Yang and M. Schroder, *Chem. Mater.*, **2016**, 28, 2331.
- 25** L. Chen, P. S. Reiss, S. Y. Chong, D. Holden, K. E. Jelfs, T. Hasell, M. A. Little, A. Kewley, M. E. Briggs, A. Stephenson, K. M. Thomas, J. A. Armstrong, J. Bell, J. Busto, R. Noel, J. Liu, D. M. Strachan, P. K. Thallapally and A. I. Cooper, *Nat. Mater.*, **2014**, 13, 954.
- 26** (a) J. S. Seo, D. Whang, H. Lee, S. I. Jun, J. Oh, Y. J. Jeon and K. Kim, *Nature*, **2000**, 404, 982; (b) Y. Peng, T. Gong, K. Zhang, X. Lin, Y. Liu, J. Jiang and Y. Cui, *Nat. Commun.*, **2014**, 5, 4406; (c) K. Tanaka, N. Hotta, S. Nagasea and K. Yoza, *New J. Chem.*, **2016**, 40, 4891.
- 27** J. Zhang, Z. Li, W. Gong, X. Han, Y. Liu and Y. Cui, *Inorg. Chem.*, **2016**, 55, 7229.
- 28** (a) Z. G. Gu, S. Grosjean, S. Brase, C. Wo'lla and L. Heinke, *Chem. Commun.*, **2015**, 51, 8998; (b) J. Zhao, H. Li, Y. Han, R. Li, X. Ding, X. Feng and B. Wang, *J. Mater. Chem. A*, **2015**, 3, 12145; (c) B. Liu, *J. Mater. Chem.*, **2012**, 22, 10094.
- 29** P. E. Hare and E. Gil-Av, *Science*, **1979**, 204, 1226.
- 30** A. Slominski et al., *FEBS Letters*, **2002**, 511, 102.
- 31** Stryer L., *Biochemistry.*, 4th ed., New York: WH Freeman and Company; **1995**.
- 32** Pardridge W.M. and Oldendorf W.H., *Biochim Biophys Acta.*, **1975**, 401(1),128.
- 33** Oldendorf W.H., *Exp Eye Res.*, **1977**, 25, Suppl.177.
- 34** Breuer, M. et al., *Angew. Chem. Int. Ed.*, **2004**, 43, 788.

General conclusions

This PhD thesis has focused on the study of the adsorption and enantioselectivity properties of two different classes of supramolecular crystals. Supramolecular chemistry deals with the elegant self-assembly of building units through weak interactions (ion-ion, ion-dipole, hydrogen bonding, cation- π , etc). Thanks to these coordinative forces, simple active molecular blocks, bearing recognition information, generate an endless number of mono, bi and tridimensional networks. Among the 3D supramolecular crystals group, the dipeptides and the metal-organic frameworks families have reached remarkable attention in the latest years.

The first part of the work was dedicated to five microporous dipeptides belonging to the Valyl-Alanine class: Valyl-Alanine itself, Alanyl-Isoleucine, Valyl-Valine, Isoleucyl-Alanine and Isoleucyl-Valine. These dipeptide crystals, known as *biozeolites*, are characterized by one-dimensional, hydrophobic, chiral channels, with diameters in a range between 5.1 and 3.4 Å. Interestingly, dipeptides containing the same amino acids, such as alanine and isoleucine, in opposite sequences, AI and IA, generate different cross-sections, that can differentiate the adsorption properties of the same guest. The use of biocompatible peptides in various association states make them suitable as drug delivery systems for hydrophobic drugs. Volatile halogenated ethers, used as inhalation agents in general anesthesia, have never been stored so far in supramolecular networks of biological origin and there are really few examples in literature for their application in drug delivery systems. The reduction of the vapor pressure of these commonly-used volatile anesthetics upon nanoconfinement may give rise to practical advantages in handling and storage, as well as for controlled administration. Moreover, the use of nanocrystals as hydrophobic-drug carriers may be attractive for parenteral or oral administration, thanks to the increased solubility and, thus, bioavailability. Enflurane, isoflurane, desflurane, halothane and diethyl ether were chosen as volatile guests. The adsorption and desorption isotherms at 298 and 273 K of the three most efficient crystals, VA, AI and VV, were presented and spectroscopic evidences for guest-anesthetic arrangement in the nanochannels. The adsorption in VA channels showed Langmuir-type profiles for all the anesthetic guests with maximum absorption values corresponding to a virtually complete loading of available volume. Type-I isotherms for enflurane were also exhibited in the case of the smaller channels of AI and VV, owing to the limited steric requirements of the chlorine on the terminal methyl group, which allows easy adjustment in the channels. On the contrary, the isotherms of the structural isomer isoflurane, bearing the chlorine substituent on the methylene group, and halothane (containing F, Cl and Br) in VV did not follow a Langmuir profile. On the contrary, in IA and IV nanochannels the halogenated molecules are excluded for their exceeding steric encumbrance. Desflurane, containing exclusively fluorine atoms as halogens and presenting the highest volatility, showed in all dipeptides modest adsorption, whilst

diethyl ether is absorbed with high efficiency in the hydrocarbon environment. Desorption branches highlighted the complete reversibility of the isotherms and no hysteresis, indicating possible reuse of dipeptides without regeneration. The spectroscopic detection of the volatile guests inside the nanochannels was provided through solid state NMR. For example, fast MAS ^1H NMR spectra illustrated the inclusion of the anesthetics in the crystalline channels of VA, AI and VV upon sorption from the gas phase. An interesting feature is the upfield shift ($\delta = -0.2$ ppm) of included halogenated ethers with respect to the pure compounds, owing to the magnetic susceptibility generated by the dipeptide environment. A theoretical study allowed us to establish the most stable conformers of isoflurane. We explored the two main dihedral angles and observed the stability of two conformational minima in the energy map. The experimental spectrum clearly indicated that the conformer II (with the torsional angle θ_2 setting one fluorine atom in *trans* and the other in *gauche* conformation) provides the only feasible arrangement of isoflurane confined in the narrow dipeptide channels: in fact, the behavior of included isoflurane is common to all the observed dipeptide crystals, such as AI and VV. The Gran Canonical Monte Carlo simulations of enflurane and isoflurane isotherms in VA show that the energetically stable conformers occupy the channels with a maximum loading corresponding to that of the experimental isotherms and the guests are not periodically distributed along the channels. This investigation may shed light on the way volatile anesthetics adapt to variable-size sub-nanometric channels, a fundamental topic for understanding the complex mechanism of general anesthesia.

In the second part of the thesis, I worked on homo-chiral metal-organic frameworks and their applications in enantioselective adsorption of small molecules, commonly-used as pharmaceutical precursors. Four new structures were synthesized, thanks to a collaboration with the university of Strasbourg, based on enantiomerically pure organic building blocks, bearing two chiral side chains and four carboxylate coordinating groups. Their combinations with Cu(II) salts led to the formation of highly robust porous crystals, displaying channels lined with homo-chiral alkyl moieties. For **1**-Cu and **3**-Cu frameworks, the stereogenic carbons were connected to a methyl group, whereas for **1**-Cu(OH) and **3**-Cu(OH) a hydroxyl group leaned on the chiral centers. We failed in obtaining a single-crystal structures of these MOFs, but all the four frameworks resulted to be isostructural to Zn(II) compounds, built with the same tetracarboxylated organic linker. The crystalline materials are robust and exhibit permanent porosity and high thermal stability. The solid-state architectures were shown to uptake guest molecules, as they capture N_2 , CO_2 and CH_4 molecules. The sorption of CO_2 takes place at room temperature and under rather low pressure (10 bar). Interestingly, the porous crystals show high affinity for CO_2 with respect to N_2 . The N_2 at 77 K and CO_2 at 195 K adsorption isotherms presented a Langmuir profile and no hysteresis in the desorption branches in all cases. The chiral environment inside the microporous channels prompted our interest for the study of their enantioselectivity properties. For the first two structures, **1**-Cu and **3**-Cu, the adsorption of D- and L-tryptophan was investigated in water: enantiopure evacuated crystals were immersed in an aqueous solution containing pure tryptophan enantiomers and their absorption capacity was monitored by UV-Vis absorption spectroscopy, by measuring the intensity of the band at 280 nm of tryptophan in solution as a function of time. While enantioselective recognition was negligible in the case of **1**-Cu, **3**-Cu adsorbs preferentially L-tryptophan, for instance, after 30 min 66% of L-

and 20% of D-tryptophan were adsorbed from the solution in a ratio of 3.3 : 1. Higher ratios up to 4 : 1 were obtained at shorter times of guest uptake; this is an indication that high enantioselectivity can be most favorably achieved far from the equilibrium conditions. The desorption process showed that, after 24 hours, an amount of guest between 2.5 and 4.9% was released from the adduct, indicating the occurrence of strong host–guest interactions. The higher stereoselectivity of **3**-Cu with respect to **1**-Cu can be explained by the longer pendants bearing the stereogenic carbons at their ends which protrude towards the center of the cavity and recognize more efficiently one of the enantiomers. The other two structures **1**-Cu(OH) and **3**-Cu(OH) were tested, instead, for the resolution of chiral small molecules. After soaking with *sec*-butylamine racemic mixtures in THF, HPLC analyses were performed to determine the enantioselectivity: the complete peak resolution and fast retention time were highlighted, but low enantiomeric excess values were found out, because of the very little dimensions of the guest. Using the same procedure, also α -methylbenzylamine and *sec*-benzamide were used as guests in racemic solutions: unfortunately, the steric hinderance due to the aromatic rings prevented their adsorption inside the nanochannels. However, these first experiments can be the starting point of a deeper investigation of selective chiral uptake and separation of other chiral molecules such as alcohols by these or similar homo-chiral porous crystalline architectures.

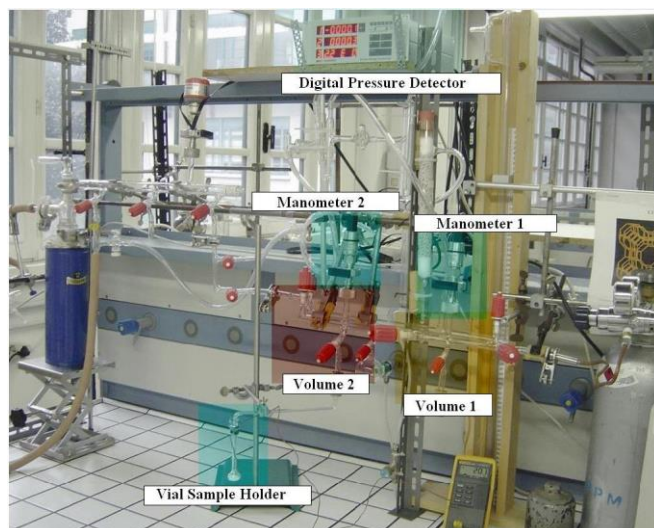
Appendix A

Experimental conditions

A.1 Gas and vapor adsorption characterization

Nitrogen and carbon dioxide adsorption-desorption isotherms were measured at their respective condensing temperature (77 and 195 K) up to 1 bar using the ASAP 2020 Micromeritics analyzer. Nitrogen, carbon dioxide and methane adsorption-desorption isotherms up to 10 bar at 273 and 298 K were performed by the ASAP 2050 Micromeritics analyzer. The samples were degassed in high vacuum (2 μ mHg) and adequately thermally treated overnight before each measurement. Surface areas were calculated using the Brunauer, Emmett, Teller (BET) and Langmuir method. The pore size distributions were calculated according to NL DFT on carbon slit pores analysis. The isosteric heat of adsorption Q_{st} values were determined by applying the Van't Hoff equation while the selectivities of CO₂/N₂ binary mixture were determined from the single-component isotherms using the ideal adsorbed solution theory (IAST) and a CO₂/N₂ ratio of 15:85 (mol:mol).

The vapor adsorption experiments have been conducted with a vacuum ramp and it has been used the volumetric method. The vacuum ramp presents three volumes: volume 1 allows to load a known pressure of a gas compound, measured by the manometer 1; it is used as a temporary reserve of the volatile substance and, through a teflon tap that connect volume 1 to volume 2, it is possible to perform the gas expansion in the second volume. The pressure in volume 2 is measured by manometer 2. Another teflon tap connects through a capillary tube volume 2 to a vial sample holder, the third volume. The vacuum pump, that permits the evacuation in the entire ramp, is connected to the volume 2 by a teflon tap. The experimental procedure used to realize the adsorption isotherms provides the loading of a known pressure of anesthetic in volume 2 and the opening of the teflon tap that connects the volume 2 to the vial sample holder. To initiate the adsorption kinetics, the detector has been set up to take the pressure values every 5 seconds for twenty minutes. The vacuum level of the system has been measured by a BOC Edwards manometer. At the end of the twenty minutes, the equilibrium pressure value has been used to calculate the quantity of adsorption molecules, known the initial weight of matrix and the volume of the vial sample holder. At last the volume of the blank, previously measured, is subtracted to the sample volume.



The empty vial sample holder is connected to the vacuum ramp and it is put in a dewar with a water bath at a known temperature (273 or 298 K). Next, the vacuum is created in all the system. During the analysis, it is used a thermometer to constantly measure the temperature of the water bath. When the vacuum is about 10^{-3} torr, the volumetric expansions in the ramp volumes begin: a known pressure of vapor is loaded in volume 1, then, the vapor is expanded in volume 2, in the reaction flask and finally in the vial sample holder. This procedure is repeated for different initial pressure values, in order to cover the range of pressures used during the isotherm measurements. Plotting the initial pressure versus the final pressure, it's possible to point out the ideal behavior range of the gas. The expansion volumes can be obtained by the slope extrapolation, known the initial one. First, I considered the empty vial sample holder weight and then I connected it to the vacuum ramp. I put it in a water bath at a known temperature (273 or 298 K) and I started the kinetics measurements. Starting from a known initial pressure value, the adsorption kinetics measurements have been taken for 20 minutes. After this time, the system has achieved the pressure equilibrium value. The blank analysis for different temperatures and anesthetics is extremely important because it allows to obtain linear and parabolic equations used to correct the isotherm volume values. Before the adsorption measurement, the porous matrix has been evacuated in vacuum at 60°C for a night, in order to eliminate all the adsorbed molecules in the channels, that can alter the following measures. The maximum pressure values used during the adsorption measures have been set from the vapor pressures. To obtain the adsorption isotherms the vapor pressures have been measured: the vapor, put in a vial, has been purified from the gaseous residues and the impurities with a *freeze and thaw* process. The vapor pressure has been measured by opening the tap that connects the vial and the volume 1. To calculate the quantity of adsorbed molecules, I weighted the empty vial and then the vial with the sample; in this way I obtained the sample weight. The vial is connected to the vacuum ramp and the vacuum is created in all the system. After fifteen minutes, the water bath at a known temperature is set on the vial sample holder. After other fifteen minutes, I can proceed with the analysis: the volumetric method consists in measuring the pressure decrease due to the vapor adsorption in the porous material. A known pressure is loaded in volume 2: to start the measure I open the tap between volume 2 and the vial sample holder. At the same time, I start the

adsorption kinetics measurements activating the pressure detector; the adsorption kinetics values are taken every 5 seconds for 20 minutes. After this time, I close the tap and I take the equilibrium pressure value from the detector. The analysis is repeated for different initial pressure values. This is known as the upload cumulative method. The pressure decrease continues gradually till the equilibrium value is asymptotically reached. The adsorption kinetics values are collected with a personal computer connected with the pressure detector and they require at least 20 minutes of measurement.

A.2 X-Ray diffraction

Single-crystal data of **1-Zn** and **3-Zn** were collected on a Bruker SMART CCD diffractometer with Mo-K α radiation at 173 K. The structures were solved using SHELXS-97 and refined by full matrix least-squares on F^2 using SHELXL-2014 with anisotropic thermal parameters for all non-hydrogen atoms.² The hydrogen atoms were introduced at calculated positions and not refined (riding model). For both structure of **1-Zn** and **3-Zn**, highly disordered solvent molecules are present, the SQUEEZE command has been employed to account for the corresponding electron density.

The dipeptides' powder X-ray diffraction patterns were collected using a Panalytical X'Pert PRO con PIXcel detector e Incident-beam focusing mirror diffractometer, (Cu-K α radiation), in the 2θ range 4° to 80° , with $\Delta(2\theta)=0.013^\circ$ and 360 sec per step as counting time. The MOFs' powder X-ray diffraction patterns were recorded using a X-Pert Pro diffractometer at room temperature. The radiation wavelength λ of the incident X-rays was 1,54 Å and a 2θ range is from 5° to 30° was investigated.

A.3 Thermogravimetric analysis

Thermogravimetric analysis (TGA) were performed at Strasbourg university, France, on a Pyris 6 TGA Lab System apparatus (Perkin-Elmer). About 2 mg of sample was heated from 30°C to 500°C at a heating rate of 5°C/min using a N_2 flow of 20 mL/min.

A.4 UV-visible absorption spectroscopy

All the spectra of Cu-based MOFs were recorded in the 220-340 nm range with a UV-visible Lambda 900 Perkin Elmer spectrophotometer, in 1 mm quartz cuvettes. Aqueous solutions of enantiopure *L*-tryptophan and *D*-tryptophan ($3.3 \cdot 10^{-3}\text{ M}$) were prepared. The strongest absorption peak of tryptophan at 280 nm was used as the reference wavelength. 15 mg of the evacuated samples were immersed in 7 ml of the tryptophan aqueous solutions and optical absorption spectra were recorded versus time. Upon uptake of tryptophan by the porous materials, the intensity of peak measured in solution decreased until it reached a plateau. The solution absorbance showed a typical Lambert-Beer linear correlation with the concentration at different wavelengths.

A.5 High Performance Liquid Chromatography measurement

High Performance Liquid Chromatography (HPLC) was performed using an AGILENT 1100 Series system composed by Agilent 1100 series autosampler, isocratic pump and WVD detector set at 240 nm. The chromatographic system was composed by a CHIRACEL OD-H column (4.6 mm x 250 mm, particle size 5 μ m) from DAICEL CORPORATION, eluted with a mobile phase hexane/isopropanol (80/20 %v/v) at flow rate 1 ml/min.

A.6 Liquid state NMR

^{13}C NMR spectra, ^{19}F NMR and ^{19}F decoupled from ^1H NMR spectra of the samples in CDCl_3 were recorded on a Bruker AVANCE NEO 400 MHz, SmartProbe™ equipped with 2 channels and 2H lock channel.

A.7 Solid state NMR

Solid-state ^1H MAS NMR spectra (single-pulse experiment SPE) were performed with a Bruker Avance III 600 MHz instrument operating at 14.1 T, using a recycle delay of 20 s. A MAS Bruker probe head was used with 2.5 mm ZrO_2 rotors spinning at 30 kHz. The 90° pulse for proton was 2.9 μ s. The ^1H chemical shift was referenced to adamantane. Spectral profiles were fit by Lorentzian line shapes. Solid-state NMR spectra were run at 75.5 MHz for ^{13}C and at 282.4 MHz for ^{19}F MHz on a Bruker Avance 300 instrument operating at a static field of 7.04 T equipped with high-power amplifiers (1 kW) and a 4 mm double resonance MAS probe. $^{13}\text{C}\{^1\text{H}\}$ ramped-amplitude cross polarization (CP) experiments were performed at a spinning speed of 8 kHz and 12.5 kHz, using a contact time of 5 ms. The 90° pulse used for proton was 2.9 μ s. $^{13}\text{C}\{^1\text{H}\}$ single-pulse excitation (SPE) experiments were run using a recycle delay of 10 s and a 90° pulse of 4.5 μ s. $^{13}\text{C}\{^{19}\text{F}\}$ ramped-amplitude cross polarization (CP) experiments were performed at a spinning speed of 8 kHz, using a 90° pulse of 3.2 μ s and a contact time of 5 ms. $^{13}\text{C}\{^{19}\text{F}\}$ SPE experiments were run using a recycle delay of 30 s, a 90° pulse of 3.65 μ s and a spinning speed of 5 kHz. Crystalline polyethylene was taken as an external reference at 32.8 ppm from TMS. ^{19}F SPE MAS NMR spectra were collected using a 90° pulse of 3.2 μ s and a recycle delay of 20 s. The ^{19}F chemical shift was referenced to NaF. The spectra were collected at 249 K and 300 K. The dipeptide crystalline powders were treated under vacuum at 60°C for 10 hours and room temperature for 12 hours, then they were transferred into the NMR rotors (4 mm for ^{13}C and ^{19}F NMR and 2.5 mm for ^1H NMR) under dry N_2 atmosphere and evacuated at room temperature for a few hours (10-3 torr). They were loaded with halogenated molecules by following the adsorption isotherms at 273-298 K, when the maximum adsorption was reached the rotors were sealed.

A.8 Dynamic light scattering measurements

Malver Zetasizer equipped with a continuous wave 1 mW He-Ne laser operating at 632.6 nm and an avalanche photodiode detector placed at 173° with respect to the incident beam was used. The sample was dispersed in toluene concentration of 2 mg/ml) and sonicated for 1 h.

A.9 Ab initio calculations

The computational study was performed using the Gaussian03 software. The dihedral angles θ_1 (C-C-O-C) and θ_2 (C-O-C-H) for isoflurane and θ_1 (Cl-C-C-O), θ_2 (C-C-O-C) and θ_3 (C-O-C-H) for enflurane were explored by incremental steps of 15° in order to localize the most stable conformers. For isoflurane, the structural optimizations and the frequency calculations were performed with the B3LYP/6-311G++(2df,p) hybrid density functional method. For enflurane, the structural optimization was performed with the B3LYP/6-311G++(2d,2p) hybrid density functional method, whereas the frequency calculation with the B3LYP/6-31G (2d) DFT method. The NMR chemical shifts and J couplings were calculated applying the B3LYP/6-311G++(2df,p) GIAO method for both the molecules.

A.10 Gran Canonical Monte Carlo simulations

Grand Canonical Monte Carlo simulations were applied to calculate the adsorption isotherms of the porous VA. The geometry optimized structures of enflurane and isoflurane were used. The CVFF and Universal force fields for enflurane and isoflurane were applied. The Lennard-Jones cut-off distance was set to 14 Å. The simulation box consists of a supercell of 2 x 2 x 3 crystallographic units with fixed atom positions of VA. All simulations include 8 x 10⁶ cycle equilibration periods. The temperature was set at 298K. The Ewald sum technique was used to compute the electrostatic interactions.

A.11 Sec-butylamine derivatization conditions

To the solution after the butylamine soaking in anhydrous THF (5 ml) was added Et₃N (30 µl) and benzyl chloride (13 µl) at room temperature under inert atmosphere and magnetic stirring. The reaction mixture was stirred for 2 hours and then diluted in Et₂O (10 ml), washed with aqueous HCl (1M, 5 ml) and concentrated in vacuum.

Appendix B

Physical properties of gases and vapors

B.1 Pressure units conversion table

	mbar	bar	Pa	KPa	MPa	atm	torr	psi
mbar	1	10^{-3}	100	0,1	$0,1 \cdot 10^{-3}$	$0,98692 \cdot 10^{-3}$	0,75006	$14,504 \cdot 10^{-3}$
bar	10^3	1	10^5	100	0,1	0,9869	750,06	14,504
Pa	0,01	10^{-5}	1	10^{-3}	10^{-6}	$9,8692 \cdot 10^{-6}$	$7,5006 \cdot 10^{-3}$	$0,14504 \cdot 10^{-3}$
KPa	10	0,1	10^3	1	10^{-3}	$9,8692 \cdot 10^{-3}$	7,5006	0,14504
MPa	$10 \cdot 10^3$	10	10^6	10^3	1	9,8692	$7,5006 \cdot 10^3$	$0,14504 \cdot 10^3$
atm	$1,0133 \cdot 10^3$	1,0133	$0,10133 \cdot 10^6$	$0,10133 \cdot 10^3$	0,10133	1	760	14,693
torr	1,3332	$1,3332 \cdot 10^{-3}$	$0,13332 \cdot 10^3$	0,13332	$0,13332 \cdot 10^{-3}$	$1,3158 \cdot 10^{-3}$	1	$19,34 \cdot 10^{-3}$
psi	68,948	$68,948 \cdot 10^{-3}$	$6,8948 \cdot 10^3$	6,8948	$6,8948 \cdot 10^{-3}$	$68,046 \cdot 10^{-3}$	51,715	1

B.2 Gas and vapor properties¹

Gas	MW [g/mol]	Triple point			Critical point			Boiling point		
		T[K]	P[Pa]	$\Delta_{\text{vap}}H$ [kJ/kg]	T _c [K]	P _c [kPa]	Vol. Mass [kg/dm ³]	T[K]	Mass. Vol. [kg/dm ³]	$\Delta_{\text{vap}}H$ [kJ/kg]
CO ₂	44,01	216,6	518500	196,52	304,2	7382,5	0,46	194,7	1,18	570,78
N ₂	28,013	63,2	12534	25,73	126,2	3399,9	0,31	77,4	0,81	198,56
CH ₄	16,04	-182,5	11692	58,42	191,1	4640,7	0,16	111,7	0,42	509,88

Vapor	MW [g/mol]	Vapor tension (kPa at 20°C)	Density (g/mL)	Boiling point (°C)	Volume (Å ³) ²
Diethyl ether	74,1	58,7	0,71	34,6	85,4
Halothane (2-bromo-2-chloro-1,1,1-trifluoroethane)	197,4	32	1,86	50,2	88,7
Enflurane (2-chloro-1,1,2-trifluoroethyl-difluoromethyl ether)	184,5	23	1,51	56,5	110,3
Isoflurane (2-chloro-2,2,2-trifluoroethyl-difluoromethyl ether)	184,5	32	1,51	48,5	108,3
Desflurane (1,2,2,2-tetrafluoroethyl difluoromethyl ether)	168	88,5	1,46	23,5	134,8

B.3 References

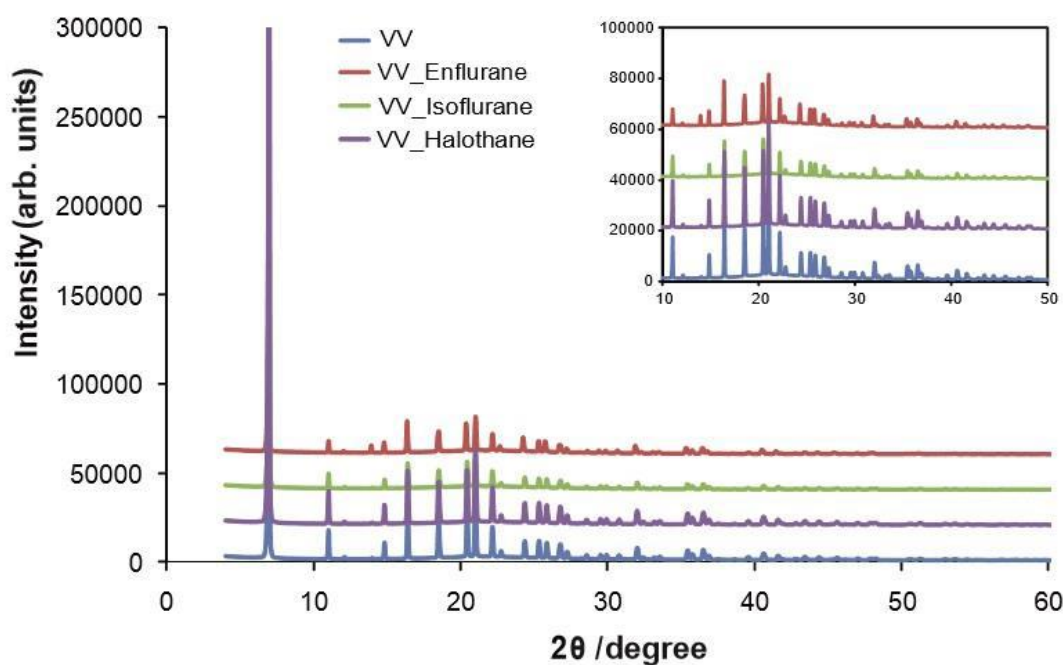
- 1) (a) *Handbook of Chemistry and Physics*, 76th ed., CRC Press, Florida, 1995;
(b) IPCS: International Programme on Chemical Safety.
- 2) Volume calculated by Material Studio 8.0, considering the van der Waals radii.

Appendix C

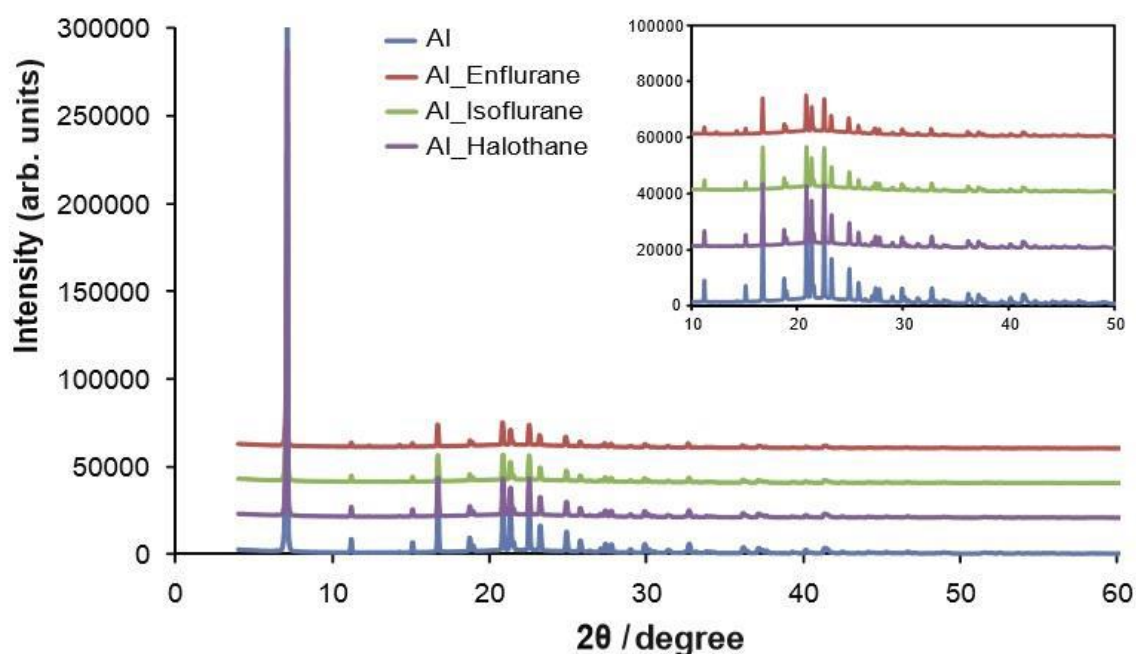
Supporting data

C.1 SI Chapter 3

C.1.1 Dipeptide powder diffraction patterns



Powder X-ray diffraction patterns of empty Valyl-Valine (blue) and with the guests (red, enflurane; green, isoflurane; purple, halothane). The unit cell parameters of the empty VV are the following: $a=14.64$ Å, $c=10.34$ Å, $V=1918.38$ Å³, $\sigma=6 \times 10^{-4}$. The unit cell parameters of VV/enflurane are the following:
 $a=14.66$ Å, $c=10.35$ Å, $V=1927.74$ Å³, $\sigma=8 \times 10^{-4}$.

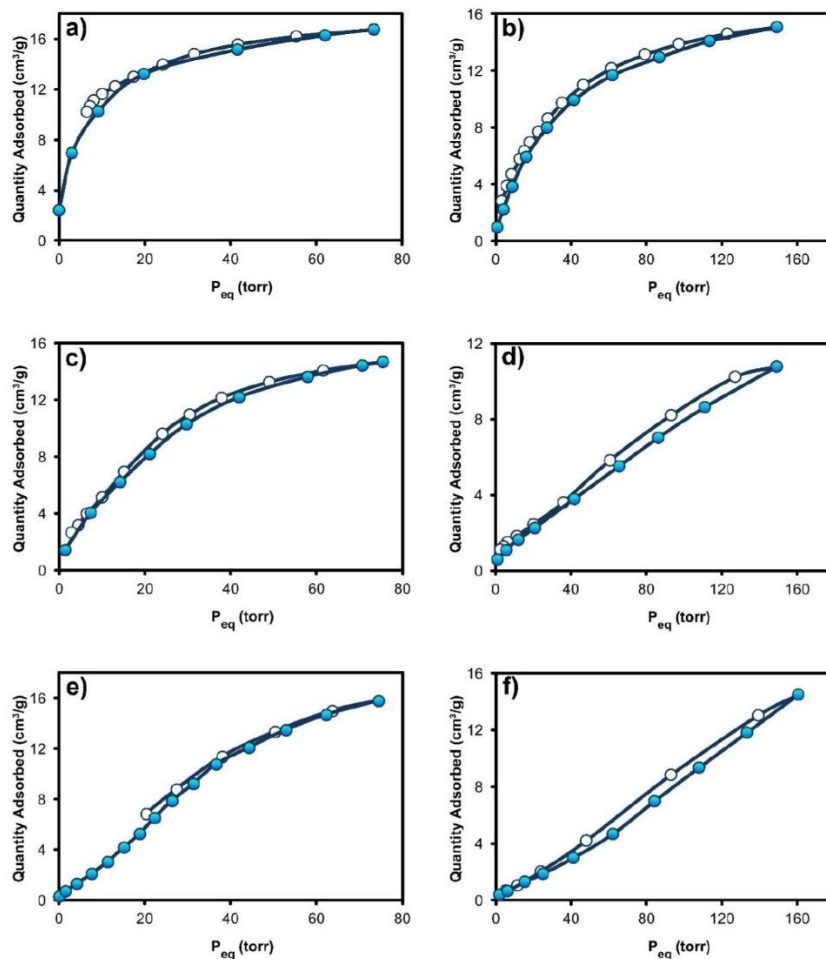


Powder X-ray diffraction patterns of empty Alanyl-Isoleucine (blue) and with the guests (red, enflurane; green, isoflurane; purple, halothane). The unit cell parameters of the empty AI are the following: $a=14.12 \text{ \AA}$, $c=10.02 \text{ \AA}$, $V=1729.60 \text{ \AA}^3$, $\sigma=2.6 \times 10^{-4}$. The unit cell parameters of AI/enflurane are the following: $a=14.17 \text{ \AA}$, $c=10.18 \text{ \AA}$, $V=1769.80 \text{ \AA}^3$, $\sigma=2.0 \times 10^{-4}$.

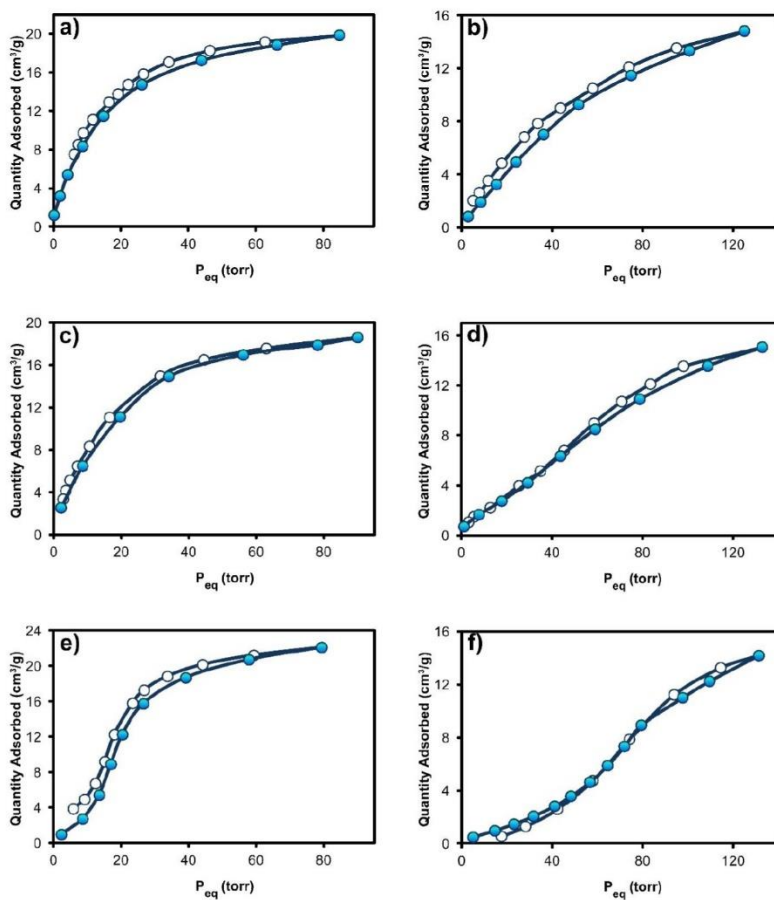
C.1.2 Isosteric heats of adsorption

	$\Delta H \text{ (kJ/mol)}$
Valyl-Alanine (VA)	
Enflurane	54.70
Isoflurane	32.70
Halothane	42
Alanyl-Isoleucine (AI)	
Enflurane	n.d.
Isoflurane	37.70
Halothane	39.80
Valyl-Valine (VV)	
Enflurane	39.60
Isoflurane	37.60
Halothane	40.70

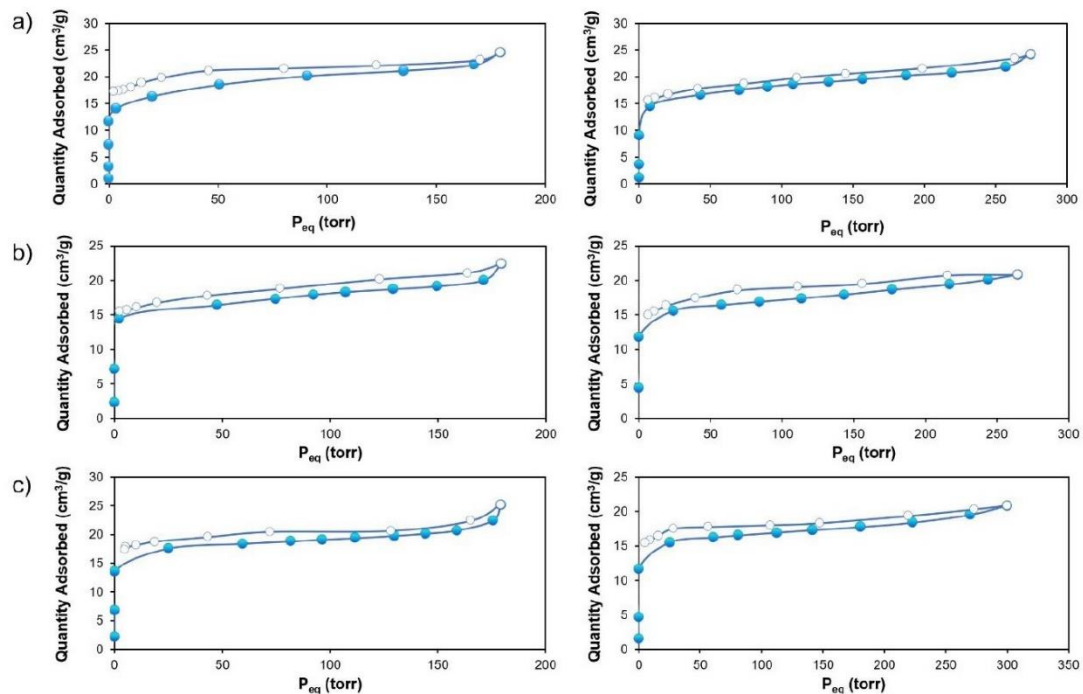
C.1.3 Adsorption isotherms



Adsorption/desorption isotherms of isoflurane in VA at 273 K (a) and 298 K (b), in AI at 273 K (c) and 298 K (d), and in VV at 273 K (e) and 298 K (f).

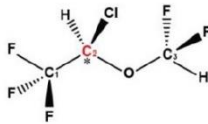
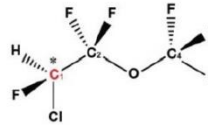


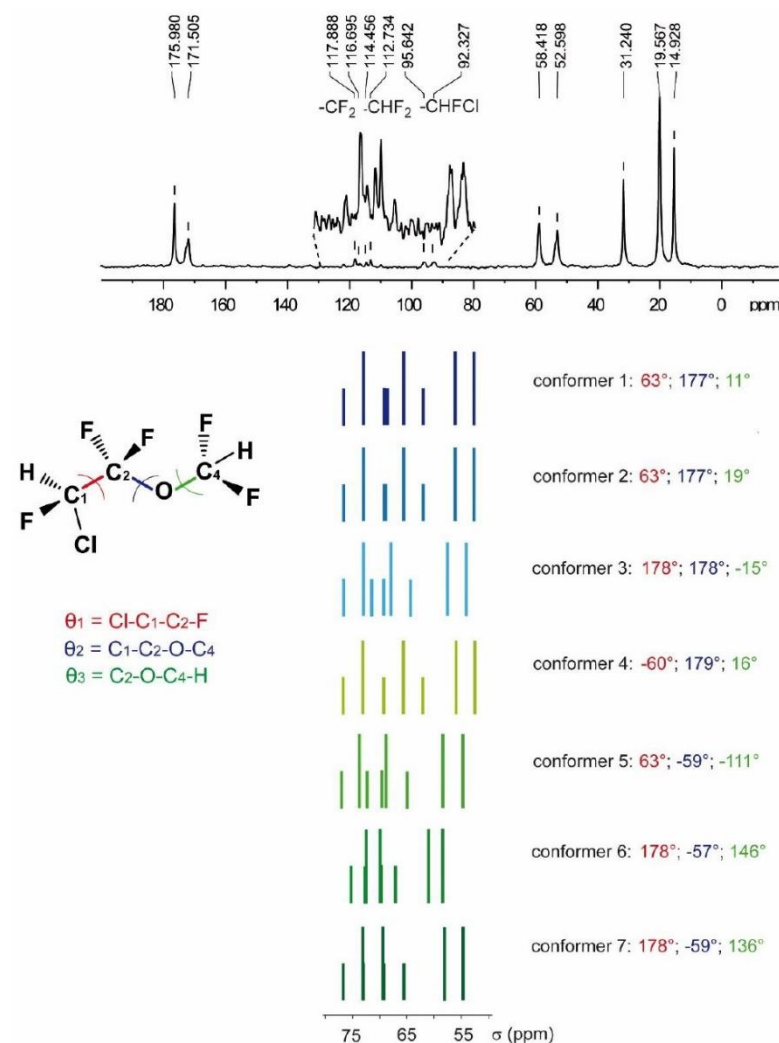
Adsorption/desorption isotherms of halothane in VA at 273 K (a) and 298 K (b), in AI at 273 K (c) and 298 K (d), and in VV at 273 K (e) and 298 K (f).



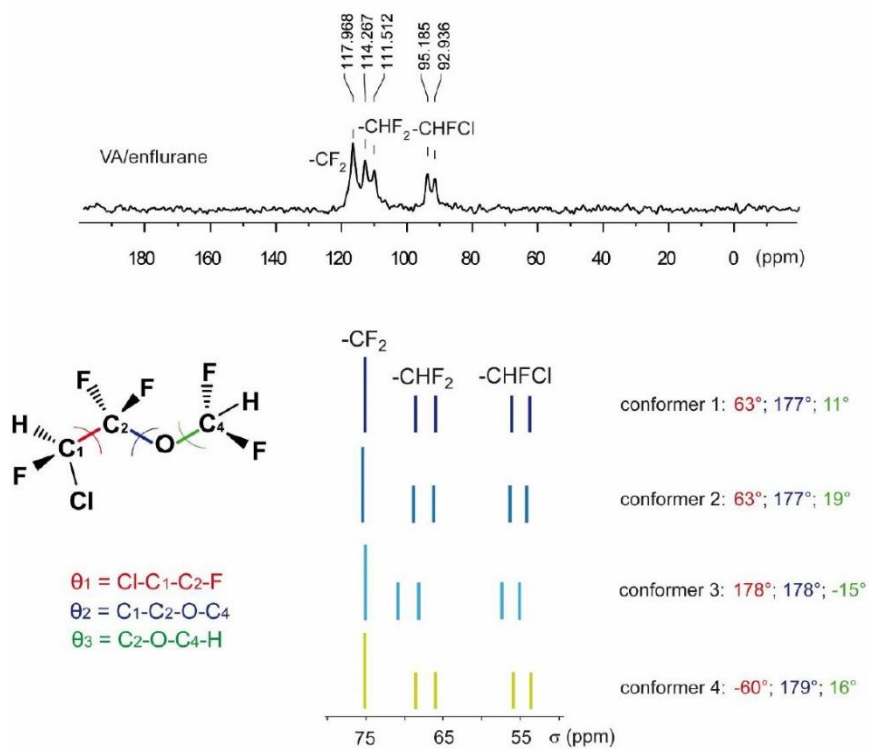
Adsorption (full circles) and desorption (empty circles) isotherms at 273 (left) and 298K (right) of diethyl ether: (a) in VA, (b) in AI and (c) in VV.

C.1.4 Conformers of isoflurane and enflurane

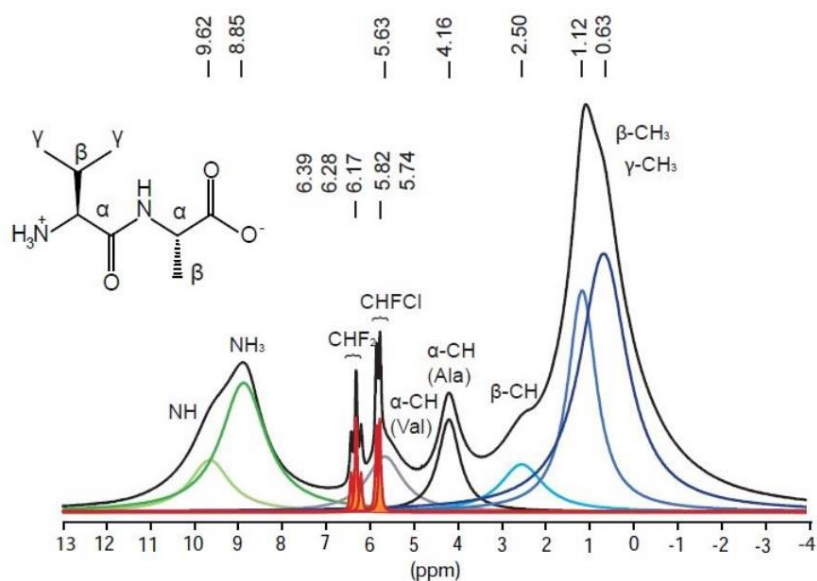
Molecules	Minima	ΔE (Kcal/mol)
 <p><i>Isoflurane</i></p> <p><u>Dihedral angles</u></p> <p>$\theta_1 = \text{C}_1\text{-C}_2\text{-O-C}_3$ $\theta_2 = \text{C}_2\text{-O-C}_3\text{-H}$</p>	Minimum 1 $\theta_1 = 139^\circ$ $\theta_2 = 179^\circ$	0
	Minimum 2 $\theta_1 = 166^\circ$ $\theta_2 = 59^\circ$	0.46
 <p><i>Enflurane</i></p> <p><u>Dihedral angles</u></p> <p>$\theta_1 = \text{Cl-C}_1\text{-C}_2\text{-F}$ $\theta_2 = \text{C}_1\text{-C}_2\text{-O-C}_4$ $\theta_3 = \text{C}_2\text{-O-C}_4\text{-H}$</p>	Minimum 1 $\theta_1 = 63^\circ$ $\theta_2 = 177^\circ$ $\theta_3 = 11^\circ$	0
	Minimum 2 $\theta_1 = 63^\circ$ $\theta_2 = 177^\circ$ $\theta_3 = 19^\circ$	0.006
	Minimum 3 $\theta_1 = 178^\circ$ $\theta_2 = -178^\circ$ $\theta_3 = -15^\circ$	0.1
	Minimum 4 $\theta_1 = -60^\circ$ $\theta_2 = 179^\circ$ $\theta_3 = 16^\circ$	0.12
	Minimum 5 $\theta_1 = 63^\circ$ $\theta_2 = -59^\circ$ $\theta_3 = -111^\circ$	0.42
	Minimum 6 $\theta_1 = 178^\circ$ $\theta_2 = -57^\circ$ $\theta_3 = 146^\circ$	0.43
	Minimum 7 $\theta_1 = 178^\circ$ $\theta_2 = -59^\circ$ $\theta_3 = 136^\circ$	0.49

C.1.5 ^1H , ^{19}F and ^{13}C Solid State NMR spectra

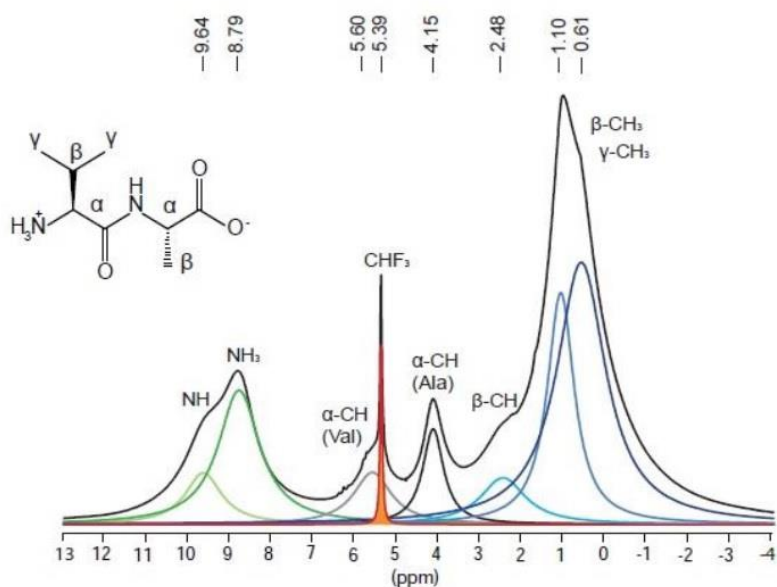
$^{13}\text{C}\{^1\text{H}\}$ SPE MAS NMR spectrum of enflurane in VA at 300 K (ss= 12.5 kHz, rd=10s) (above). Calculated ^{13}C shielding constants of the 7 conformers (below).



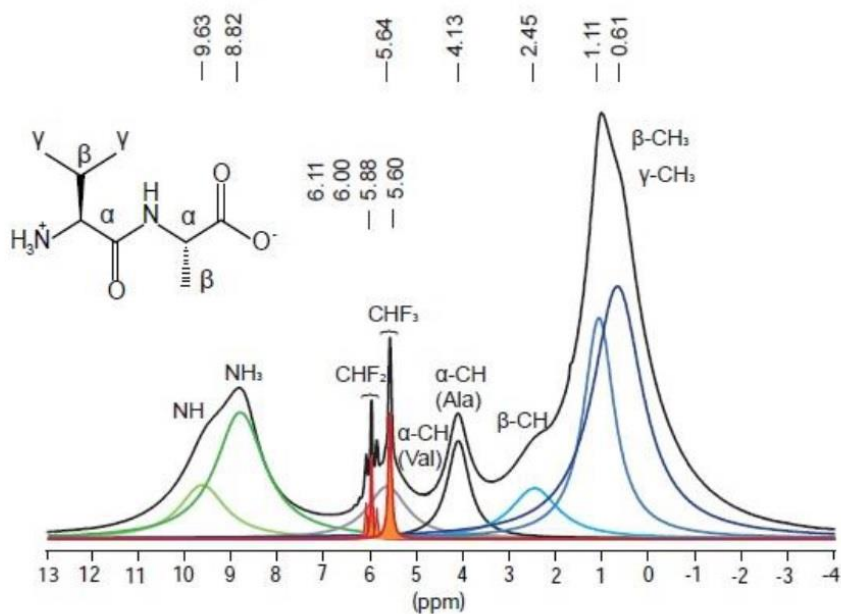
$^{13}\text{C}\{^{19}\text{F}\}$ CPMAS NMR spectrum of enflurane in VA (above). A spinning speed of 8 kHz was applied, $\text{ct} = 5$ ms, $T = 243$ K. Calculated ^{13}C shielding constants of the 4 conformers (below).



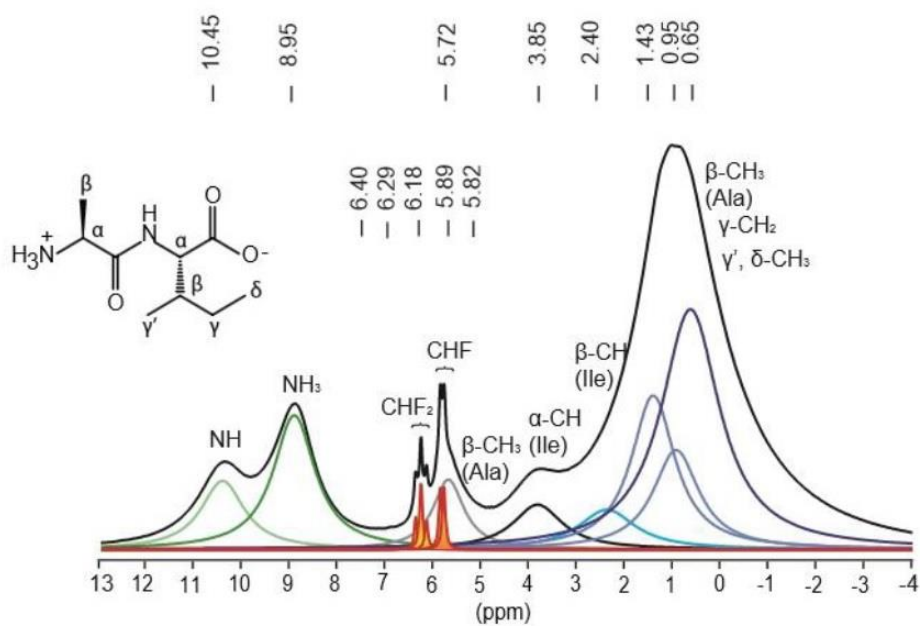
^1H SPE fast-MAS NMR spectrum of VA/Enflurane (600 MHz and 30 kHz spinning speed).



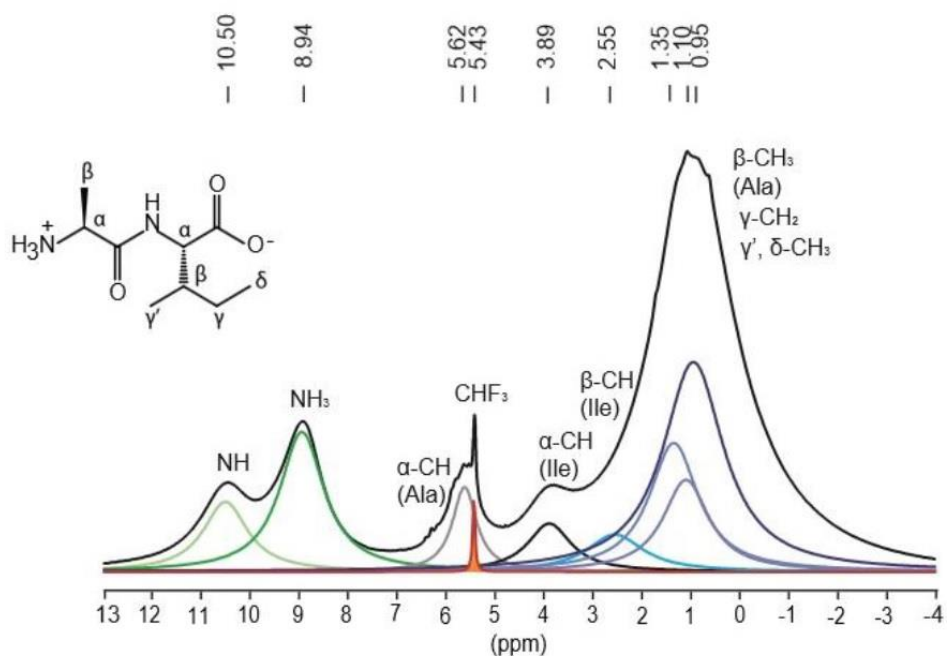
¹H SPE fast-MAS NMR spectrum of VA/Halothane (600 MHz and 30 kHz spinning speed).



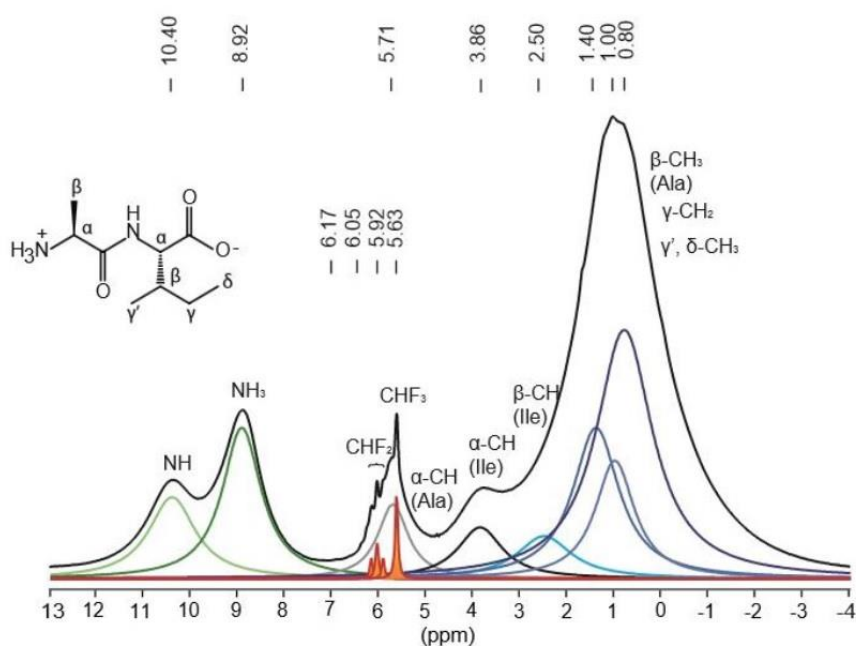
¹H SPE fast-MAS NMR spectrum of VA/Isoflurane (600 MHz and 30 kHz spinning speed).



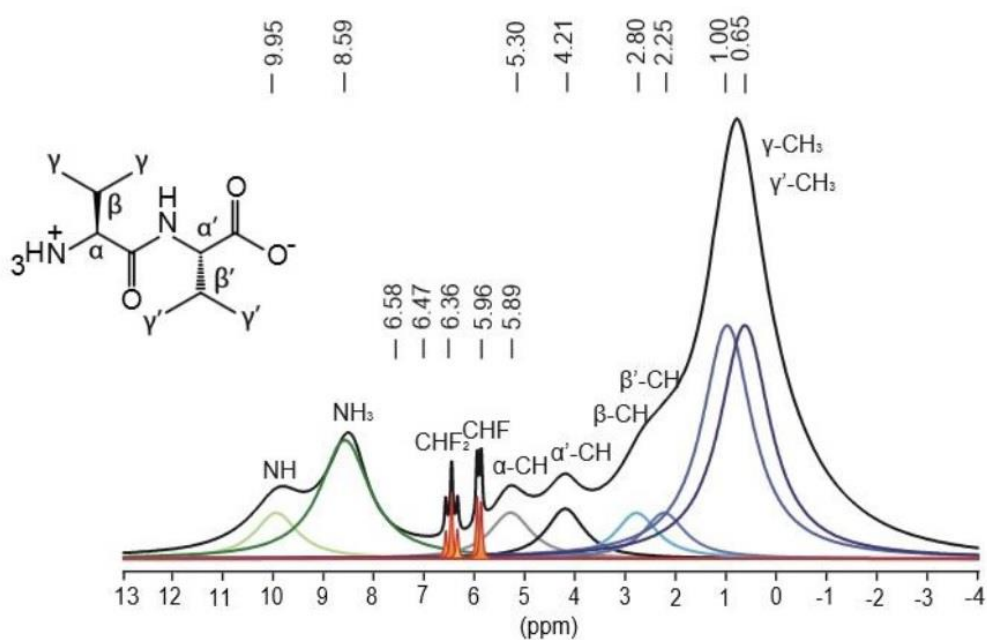
^1H SPE fast-MAS NMR spectrum of AI/Enflurane (600 MHz and 30 kHz spinning speed).



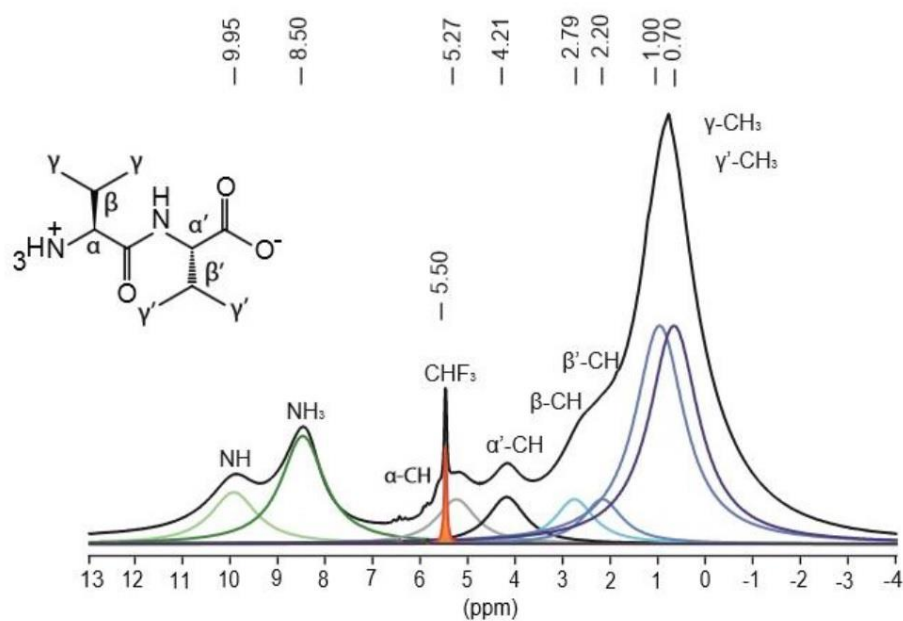
^1H SPE fast-MAS NMR spectrum of AI/Halothane (600 MHz and 30 kHz spinning speed).



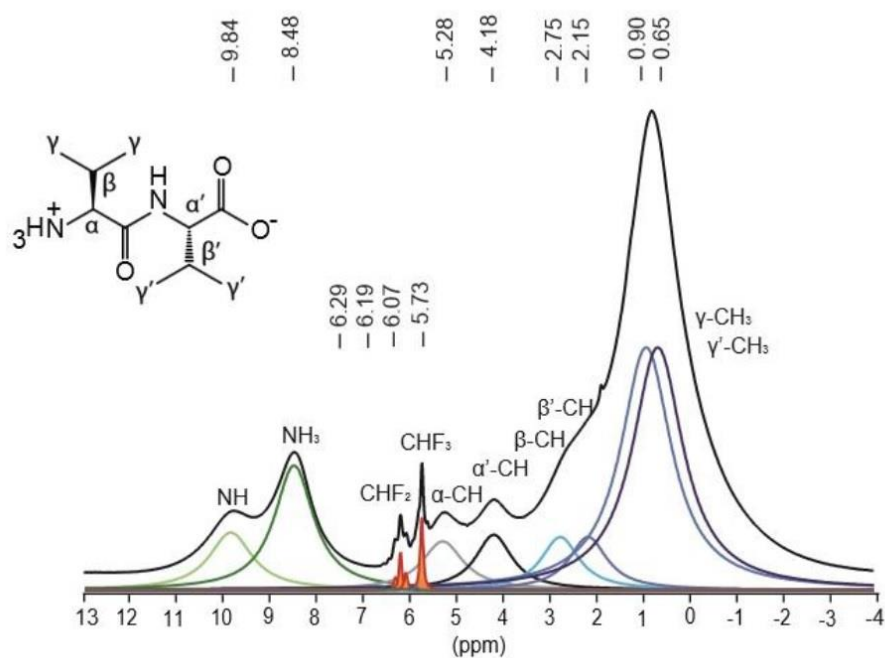
¹H SPE fast-MAS NMR spectrum of AI/Isoflurane (600 MHz and 30 kHz spinning speed).



¹H SPE fast-MAS NMR spectrum of VV/Enflurane (600 MHz and 30 kHz spinning speed).

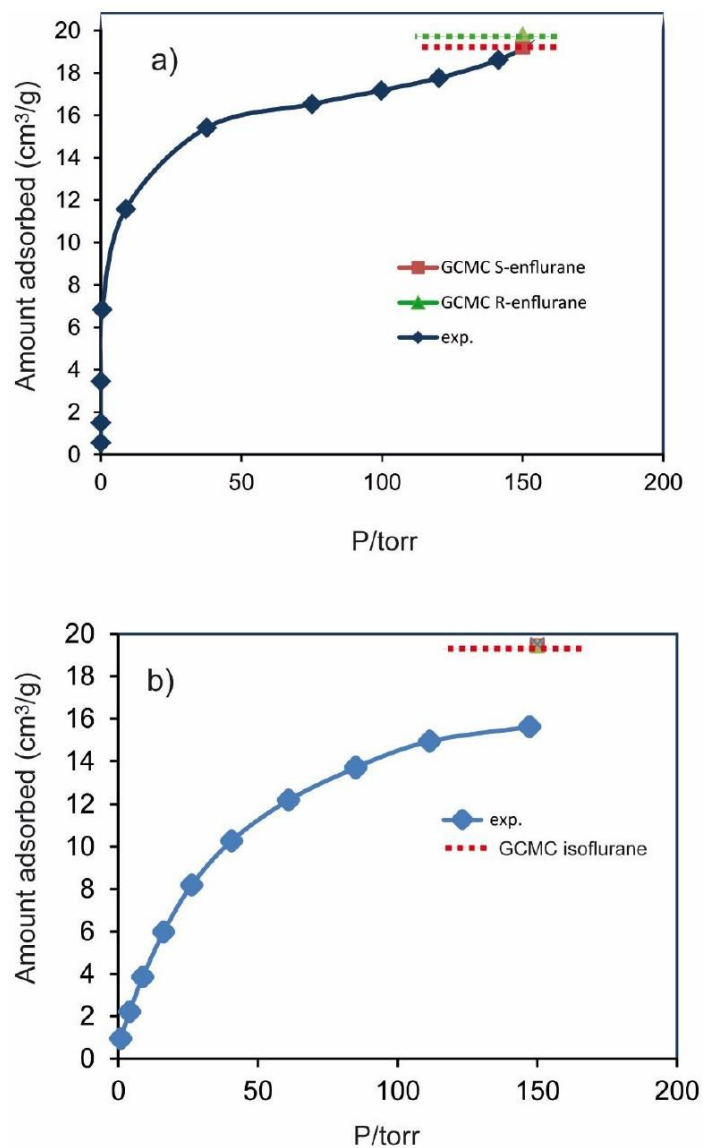


¹H SPE fast-MAS NMR spectrum of VV/Halothane (600 MHz and 30 kHz spinning speed).



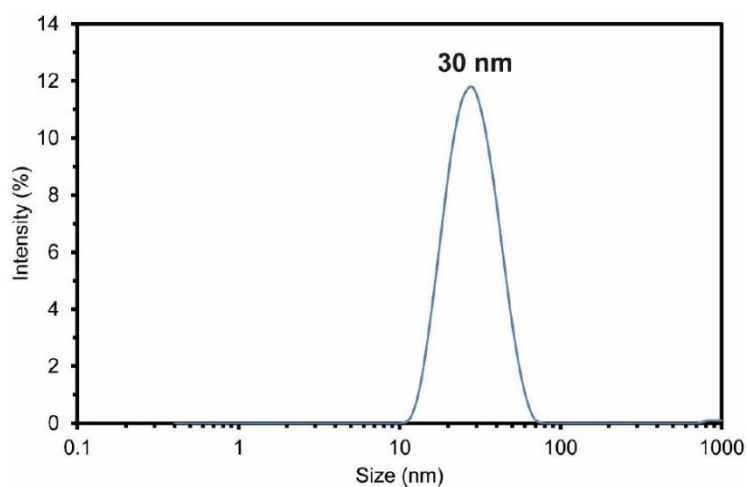
¹H SPE fast-MAS NMR spectrum of VV/Isoflurane (600 MHz and 30 kHz spinning speed).

C.1.6 GCMC simulations



Enflurane (a) and isoflurane (b) adsorption isotherms in VA. The experimental isotherms are compared to the maximum adsorption values calculated by GCMC simulation. Adsorption values of *R*- and *S*- enflurane are 19.2 and 19.8 cm³/g, respectively. Adsorption values of isoflurane for conformers I and II and in both conformations correspond to 19.51 cm³/g

C.1.7 Dynamic Light Scattering



Particle size distribution of the VA crystals. The distribution size is centered at 30 nm.

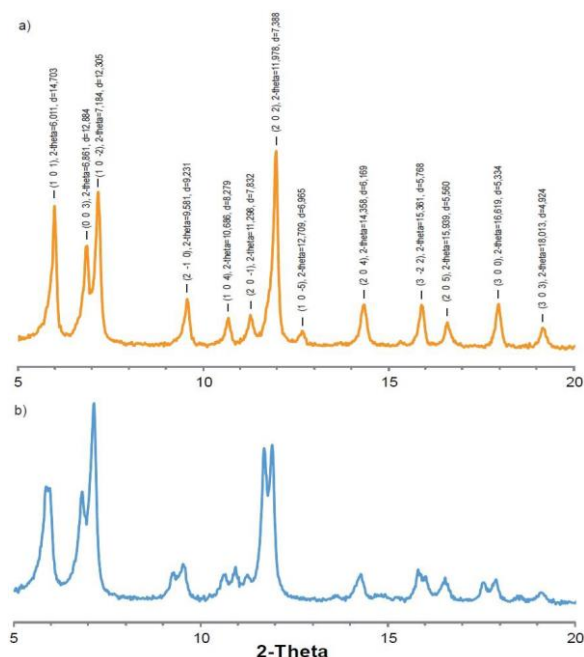
C.2 SI Chapter 4

C.2.1 Crystal structure data of 1-Zn and 3-Zn

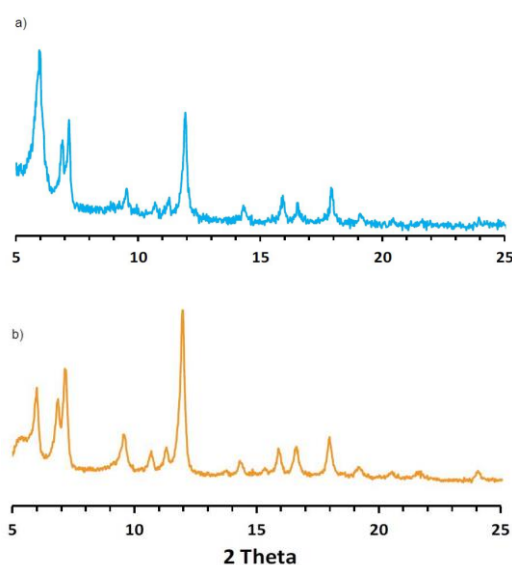
	1-Zn	3-Zn
Formula	C ₃₀ H ₃₀ O ₁₂ Zn ₂	C ₃₂ H ₃₄ O ₁₂ Zn ₂
FW	713,33	741,33
Crystal system	Rhombohedral	Rhombohedral
Space group	R3	R3
<i>a</i>/Å	18,9586(7)	18,8323(7)
<i>b</i>/Å	18,9586(7)	18,8323(7)
<i>c</i>/Å	38,0589(13)	38,4958(15)
<i>α</i>/°	90	90
<i>β</i>/°	90	90
<i>γ</i>/°	120	120
<i>V</i>/Å³	11846,7(7)	11823,6(8)
<i>Z</i>	9	9
T/K	173(2)	173
<i>μ</i>/mm⁻¹	0,950	0,951
Refls. coll	15013	14983
Ind. refls. (<i>R</i>_{int})	15013	14983

CCDC 1520830 and 1520777 contain the supplementary crystallographic data for **1-Zn** and **3-Zn**. These data can be obtained free of charge *via* www.ccdc.cam.ac.uk/data_request/cif.

C.2.2 PXRD patterns

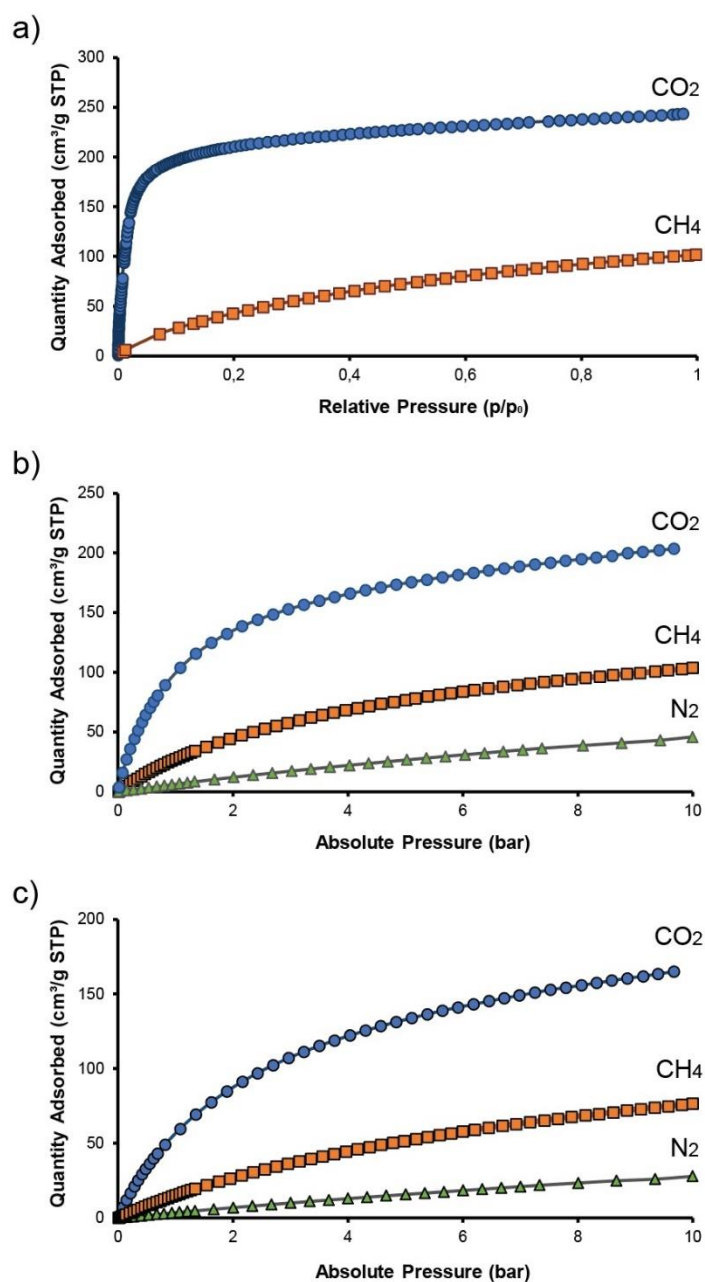


PXRD patterns of evacuated **3-Cu** (a) and **1-Cu** (b). The unit cell parameters were calculated by non linear least square fitting and the interplanar distances were indexed considering the space group R3. The cell parameters and volumes are the following: $a = b = 18,7534 \text{ \AA}$ ($\pm 0,0344$), $c = 38,6509 \text{ \AA}$ ($\pm 0,0955$), $V = 11772,05 \text{ \AA}^3$ ($\pm 0,0010$) for **3-Cu**; $a = b = 18,8943 \text{ \AA}$ ($\pm 0,0537$), $c = 38,5605 \text{ \AA}$ ($\pm 0,1438$), $V = 11921,63 \text{ \AA}^3$ ($\pm 0,0013$) for **1-Cu**.

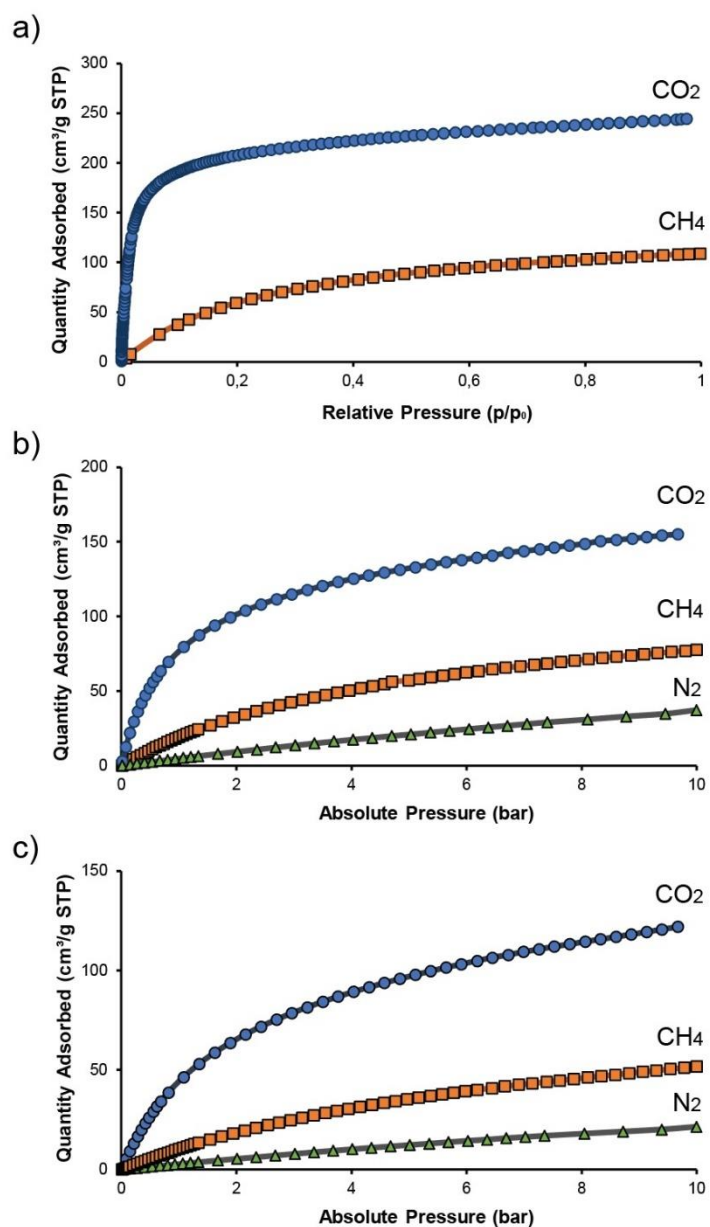


PXRD for **3-Cu** (a) and **1-Cu** (b) after 24 hours of soaking in water.

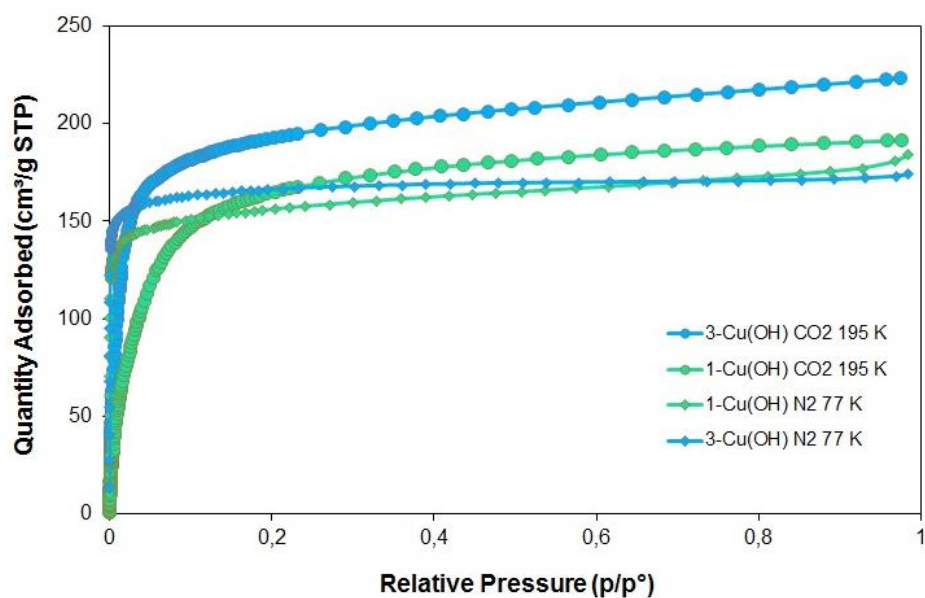
C.2.3 Adsorption isotherms for Cu-based MOFs



Adsorption isotherms of 1-Cu: a) at 195 K; b) at 273 K; c) at 298 K. Desorption curves are omitted for clarity.

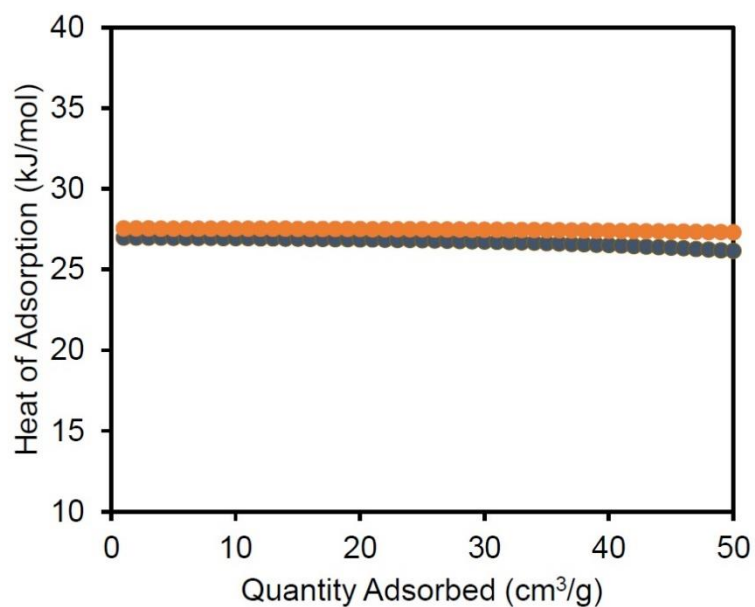


Adsorption isotherms of **3**-Cu: a) at 195 K; b) at 273 K; c) at 298 K. Desorption curves are omitted for clarity.

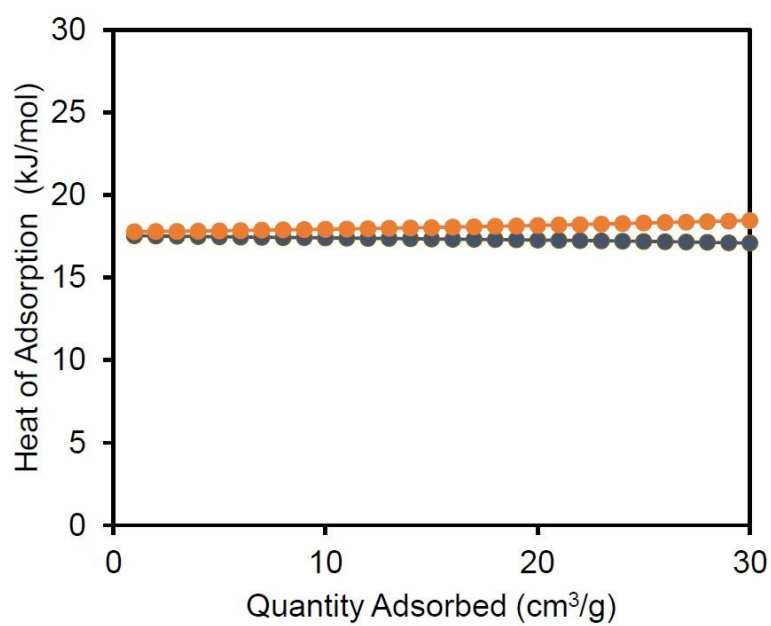


N₂ at 77 K and CO₂ at 195 K Adsorption isotherms of **1**-Cu(OH) and **3**-Cu(OH).

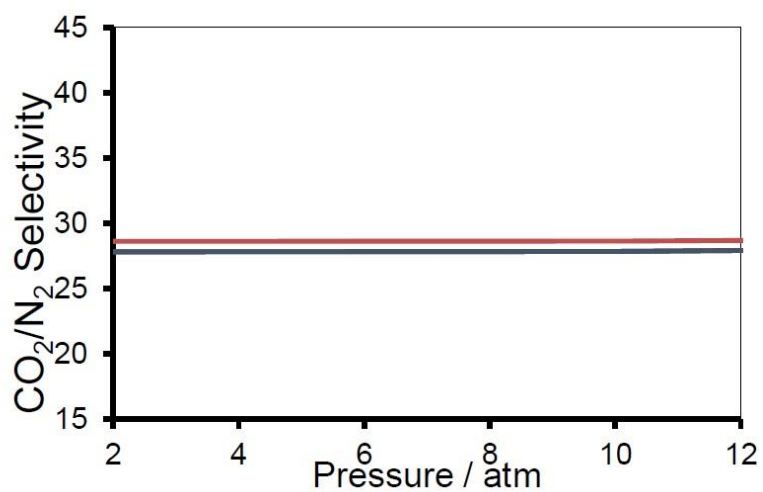
C.2.4 Isostatic heats of adsorption and CO₂/N₂ selectivity



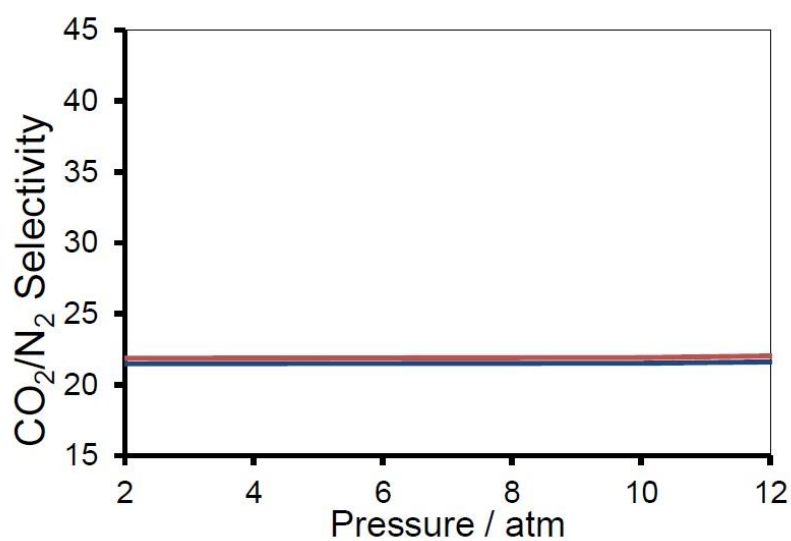
CO₂ heat of Adsorption of **1**-Cu (grey) and of **3**-Cu (red).



CH₄ heat of Adsorption of **1**-Cu (grey) and of **3**-Cu (red).

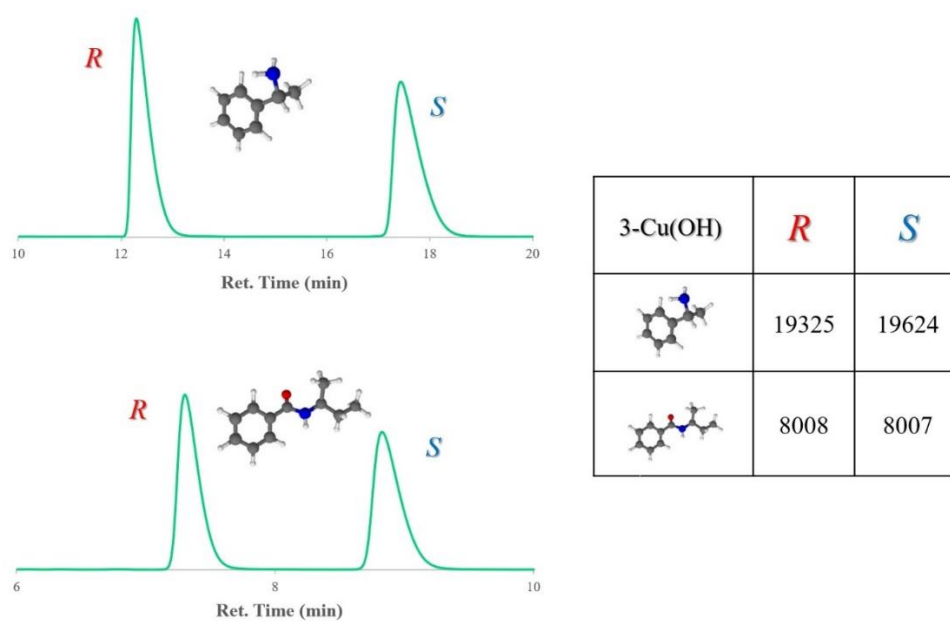


Selectivity of **1**-Cu (blue) and of **3**-Cu (red) on CO₂/N₂ mixture at 273 K.



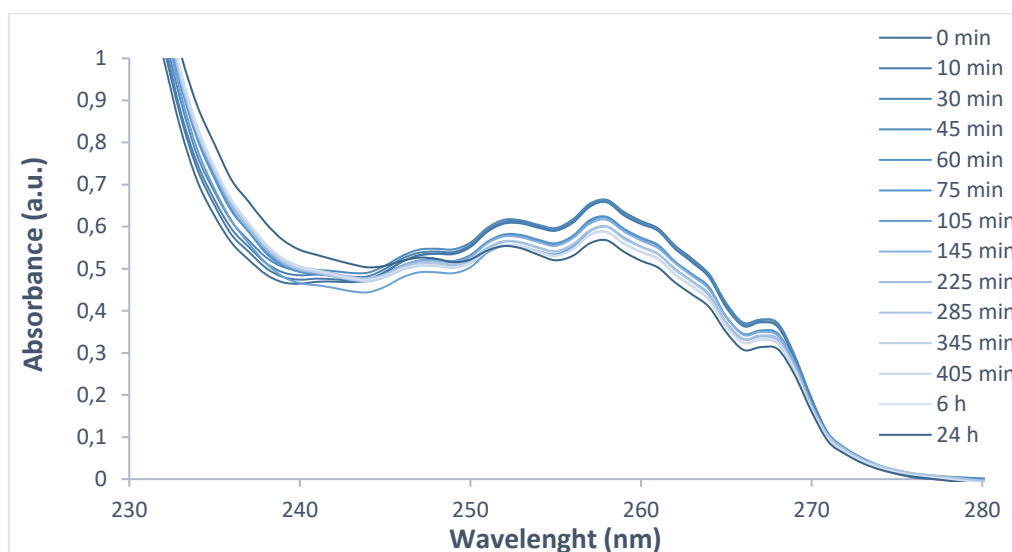
Selectivity of **1**-Cu (blue) and of **3**-Cu (red) on CO₂/N₂ mixture at 298 K.

C.2.5 HPLC chromatograms

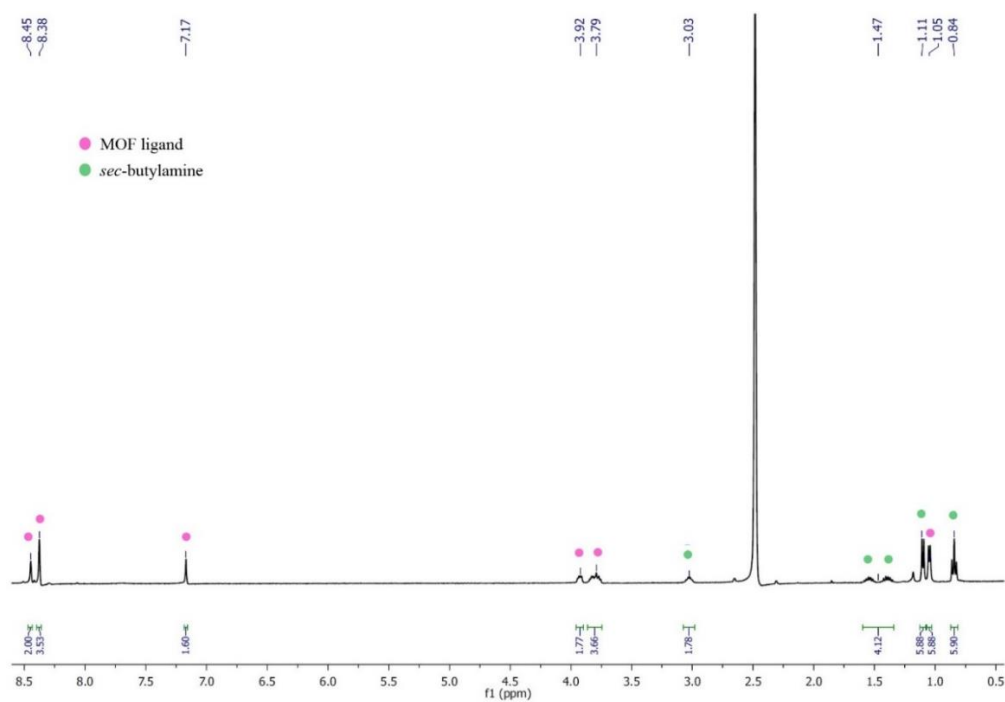


HPLC chromatograms of methylbenzylamine (up) and N-sec-benzamide (below) separation on **3**-Cu(OH). In table, the areas of the single enantiomers' peaks are reported.

C.2.6 UV-vis MBA adsorption monitoring



UV-visible spectrum of methylbenzylamine in acetonitrile adsorbing for 24 hours in **1**-Cu(OH).

C.2.7 Liquid ^1H NMR spectra

^1H liquid NMR spectrum of **3**-Cu(OH) after *sec*-butylamine adsorption, dissolved in deuterated TFA and DMSO.